ISSN 1000-9620

Marine Science Bulletin

海洋通报

Volume 10 • Number 2 2008

ISSN 1000-9620
02>
9 771000 962001

NATIONAL MARINE DATA AND
INFORMATION SERVICE OF CHINA

LIBRARY

FEB 18 2009

National Oceanic & Atmospheric Administration
U.S. Dept. of Commerce

MARINE SCIENCE BULLETIN

Vol.10 No.2 Oct. 2008

CONTENTS

Application of Argo Data in the Analysis of Water Masses
In the Northwest Pacific Ocean ····· SUN Chaohui et al. (1)

An Assessment of Urban Heat Island Effect
using Remote Sensing Data·····WANG Guiling et al. (14)

Development and Application of the GIS-Based Water Mass
Analysis Integrated System·····ZHANG Yuexia et al. (26)

Numerical Simulation of the Influence of Mean Sea Level Rise
on Typhoon Storm Surge in the East China Sea·····GAO Zhigang et al. (36)

Antarctic Psychrophile Bacteria Screening for Oil Degradation
and Their Degrading Characteristics·····ZHENG Zhou et al. (50)

Study on Different Size-fractionated Phytoplankton Assemblage
Change in the Mesocosm Ecosystem ····· LI Tao et al. (58)

Correlation and Path Analysis for Growth Traits in F_1
Population of Pearl Oyster *Pinctada martensii* ·····DENG Yuewen et al. (68)

Dynamics Characteristics and Topographic Profile Shaping
Process of Feiyan Shoal at the Yellow River Delta ·····YING Ming et al. (74)

Application of Dynamic Track Drawing Algorithm
in Ship Monitoring System ····· ZHANG Feng et al. (89)

U.S. NATIONAL OCEANIC AND ATMOSPHERIC ADMINISTRATION
NOAA
U.S. DEPARTMENT OF COMMERCE

LIBRARY
Pacific Islands Fisheries Science Center
NOAA Fisheries
Honolulu, Hawai'i

Vol.10 No.2 Marine Science Bulletin Oct. 2008

Application of Argo Data in the Analysis of Water Masses in the Northwest Pacific Ocean

SUN Chaohui, XU Jianping, LIU Zenghong, TONG Mingrong, ZHU Bokang

State Key Laboratory of Satellite Ocean Environment Dynamics, Second Institute of Oceanography, State Oceanic Administration, Hangzhou 310012, *Zhejiang, China*

Abstract: The temperature and salinity distributions, and the water mass structures in Northwest Pacific Ocean are studied using the temperature and salinity data obtained by Argo profiling floats. The T-S relation in this region indicates there exist 8 water masses, they are the North Pacific Tropical Surface Water (NPTSW), North P, acific Subsurface Water (NPSSW), North Pacific Intermediate Water (NPIW), North Pacific Subtropical Water (NPSTW), North Pacific Deep Water (NPDW) and Equatorial Surface Water (ESW), and the South Pacific Subsurface Water (SPSSW) and South Pacific Intermediate Water (SPIW).

Keywords: Argo profiling float; T-S relation; water mass analysis; the Northwest Pacific Ocean

Introduction

Northwest Pacific Ocean around the southeast coast of our country is the cradle of the East Asia Monsoon and typhoon, and also the area of genesis of Kuroshio, which makes it a hot spot to study for oceanologists and meteorologists at home and abroad. Many international investigation projects such as TOGA, WOCE and CLIVAR were all executed in this area.

Chinese scientists have studied the distribution and characteristics of the water masses with data from routine investigations and got some good results. Using the fuzzy clustering rigid division method combined with T-S relation analysis method LI Xulu[1-3] divided the water masses of upper layers of the North Equatorial Current and its adjacent area (section 130°E), and showed that there were 4 water masses above 1 000 meters of depth, and they were the West Pacific Tropical Surface Water, North Pacific Subsurface Water, North Pacific Intermediate Water and Antarctic Intermediate Water. He also divided the upper water of North Equatorial Countercurrent Groove (section 8°N) into 4 water masses, the North Pacific Tropical Surface Water, North Pacific Subsurface Water, North Pacific Intermediate Water, Antarctic Pacific Intermediate Water, their boundaries were at about 75, 200 and 310 meters separately. He also found 3 water masses in 1 000 meters of the source area of Kuroshio, North Pacific Tropical Surface Water, North Pacific Subsurface Water and North Pacific Intermediate Water, their boundaries were at about 100 and 350 meters. With an advanced marine observing equipment of the Argo profiling float, temperature and salinity data of 2 000 meters deep can be obtained every 10 days[4], and with the increase of the floats number, it is possible to have a further study on the northwest Pacific water masses

Received on December 25, 2007

and some new understandings could be expected.

1 Data source and analysis method

The data used in this paper are from 39 Argo profiling floats (18 of them were deployed by China) in the Northwest Pacific (0° - 25°N, 115° - 145°E). Fig. 1 shows the trajectories of these floats. To insure the accuracy and reliability of these data, real-time and delayed mode quality control were made beforehand[1].

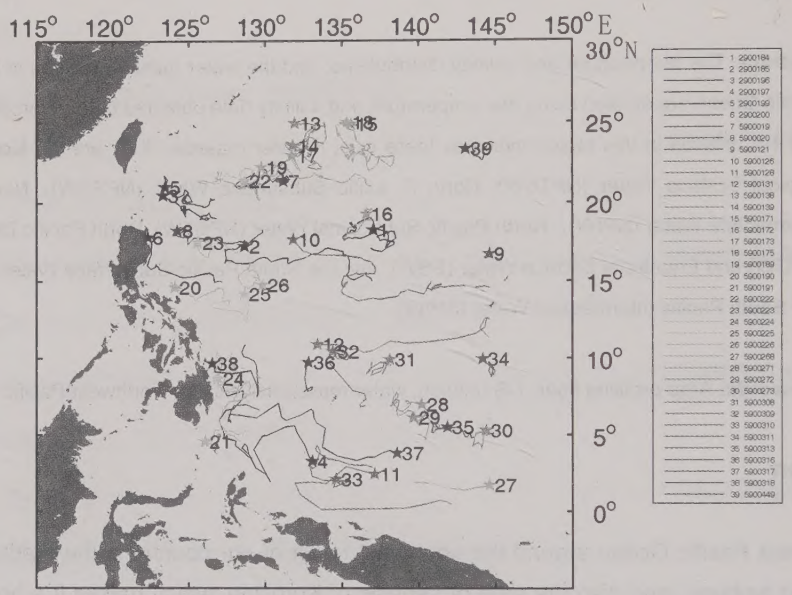

Fig. 1 Floating trajectory of Argo profiling floats in the sea area of northwest pacific ocean

In water mass analysis, water mass distribution was analysed with the T-S diagram first [5], and the water masses were further divided with fuzzy clustering soft division method, so as to get more reasonable results [6, 7].

According to the attribution level of the sample point to each water mass, the contours were drawn with clustering soft division method, and the core, boundary and mixing zone of the water masses were described objectively and quantificationally. For example, the sample points with attribution value greater than 0.9 were regarded as the core zone of the water mass, those with attribution value greater than and equal to 0.5 as the body of the water mass, and those with attribution value less than 0.5 as the mixing zone. In this way, the distribution, structure and mixing process of the water masses could be described clearly [8]. In addition, F examination could be done easily to different division methods, to get the best division method. This is the most remarkable advantage of the fuzzy clustering soft division method.

1) Tong Mingrong. The discussion about data processing and correction of Argo floats. Hangzhou: Master's degree thesis. Second Institute of Oceanography, SOA, 2004.

Since the Argo floats are drifting in the ocean freely, the range of the data for the studied area can be ensured, and there will be too much data to calculate for water mass analysis with fuzzy clustering analysis method if all the data are analysed. That is why our calculation for dividing the water masses was made by season. According to the climate features of the northwest Pacific Ocean, four seasons are divided as follows: Jan. to Mar. is winter, Apr. to Jun. is spring, Jul. to Sep. is summer and Oct. to Dec. is autumn. In this paper water masses distribution in the depth of 0 to 2 000 meters in winter and summer was analysed. Fig. 2 shows the position of the Argo sections in winter and summer. According to the distribution of the section, section P2 (around 137°E in winter) and P3 (around 137°E in summer) were set to show the vertical distribution of the water masses in this area, and section P1 was set to compare with the results of previous studies.

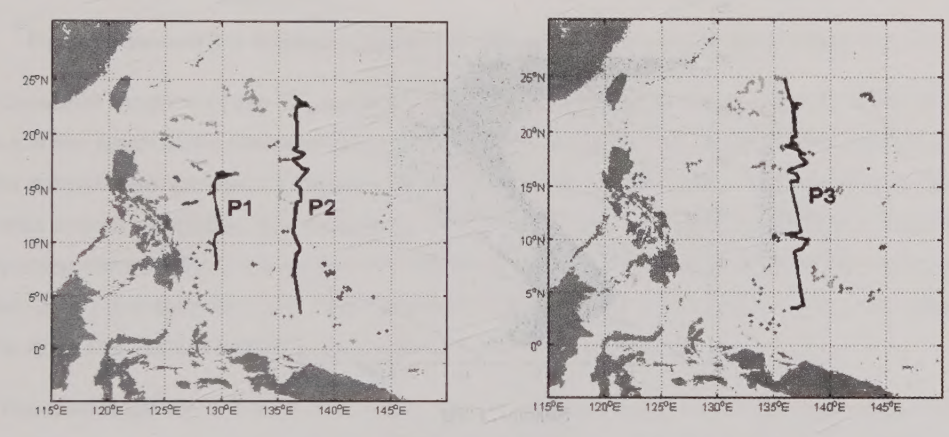

Fig. 2 Selected sections from Argo profiling float observations (a) winter (b) summer

2 Water masses analysis

Since the study area is in the west of the tropical North Pacific Ocean, it can be influenced by water driven by circulation of the North Pacific Ocean (or Arctic) from the north, of the South Pacific (or Southern Ocean) from the south, and of the East Pacific Ocean from the east. Under the constraints of the study area and observing time, only the temperature and salinity data from Oct. 2002 to Oct. 2003 were used to make the T-S diagrams and T-S curves, and then fuzzy clustering soft division method was used to analyse and discuss the distribution and structure of the water masses.

2.1 Distribution of temperature and salinity

T-S diagram of the research area was drawn with the temperature and salinity profiling data from 39 Argo floats (Fig. 3), which shows that the T-S diagram is a reverse 'S' in shape, which means the water structure here was high temperature and low salinity in surface, and high temperature and high salinity in subsurface, less-low temperature and salinity in intermediate layer and low temperature less-high salinity in deep layer. Surface, subsurface and intermediate water's T-S diagram scattered, which means that

water there were strongly mixed. According to results of the previous research, these 4 water masses could be named the North Pacific Tropical Surface Water, North Pacific Subsurface Water, North Pacific Intermediate Water and North Pacific Deep Water. The T-S diagram converges (which means well-mixed water mass) between the North Pacific Subsurface Water and North Pacific Intermediate Water, and the water body was usually called the North Pacific Subtropical Mode Water. However the southern part of the research area was also influenced by the Equator Surface Water, South Pacific Subsurface Water and South Pacific Intermediate Water, which results in the scattering of the T-S diagram. If the T-S diagrams to the north and south of 12°N were dawn separately (Fig. 4), the distribution of the water masses and their influence between one another could be seen.

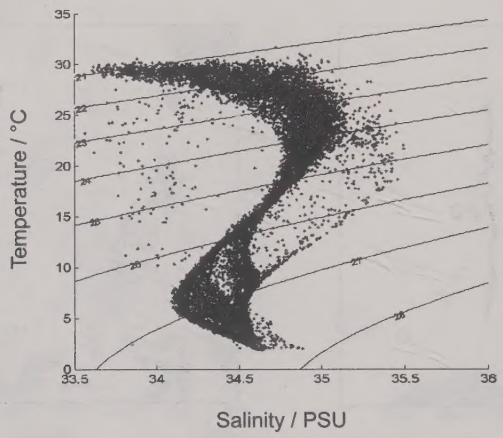

Fig. 3 T-S diagram (All the observed profile data of the 39 floats)

Fig. 5 shows the T-S curves of the measurements of 5 floats in Jan. and Jul. in different areas of the research waters. The water temperature changed little except for the surface water in Jan. which was lower than Jun.. North Pacific intermediate low salinity water came from the north of the research area (north of 20°N), which was represented by the T-S curve from the data obtained by float 5900222, and the lowest salinity value was 34.20. The southern part of the research area represented by T-S curve drawn with data from float 5900317 was obviously influenced by the intermediate low salinity water from the Southern Pacific, and the lowest salinity was 34.60. Floats 5900020, 5900226 and 5900224 were all in the middle of the research sea area (10° - 20°N), and the clear distribution of the intermediate low salinity water shows the extent of mixing and influence between the 2 low salinity water masses in the south and north in this area. But the function and influence of the subsurface high salinity water was far not so obvious as the intermediate low salinity water. Float 5900317 was influenced by South Pacific subsurface high salinity water the most, and the seasonal variation was not obvious. It seems that the North Pacific subsurface high salinity water was represented by float 5900226 in the middle of the research area, and its seasonal variation was also not obvious. But the high salinity value from Floats 5900224, 5900020 and 5900222 located to the north and South of Float 5900226 had obvious seasonal variation. It's noteworthy that the North Pacific Subtropical Mode Water only existed in the middle and north of the research sea area.

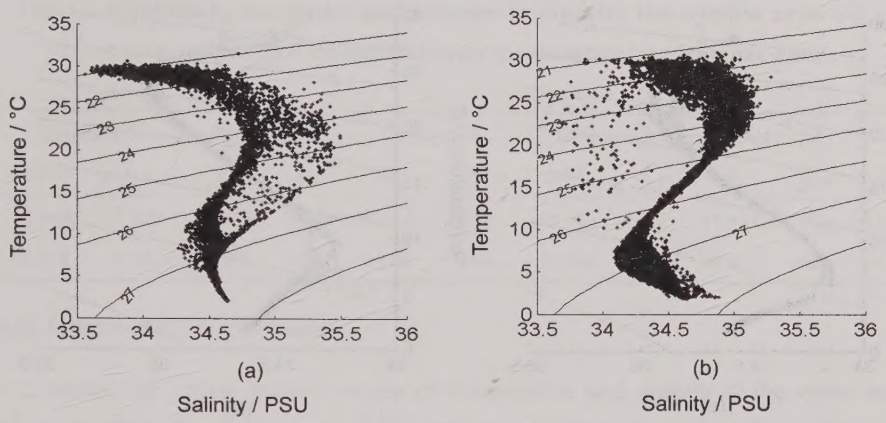

Fig. 4 Observed T-S diagram of the floats in the area to the south (a) and north (b) of 12

Seasonal variation of the T-S curves (Fig. 6) shows that the temperature and salinity variation was obvious in the south of the research area. It can be seen from the T-S curve of float 5900317 (c of Fig. 6) that the temperature variation of the surface water and deep water in four seasons was not obvious, the latter was almost invariable. But the salinity of the subsurface high salinity water and intermediate low salinity water varied greatly, the variation of the former in spring (Apr.) and autumn (Oct.) was greater than in winter (Nov.) and summer (Jul.). The highest salinity value >35.30 occurred in Oct. and it was about 0.5 lower in Apr.. The highest salinity in Jan. and Jun. was similar, about 34.90.

The lowest salinity value of the intermediate low salinity water occurred in Jan. (about 34.40), and the highest occurred in Apr. (about 34.80), on which further study should be made. The salinity variation in June and Oct. was not obvious, about 34.50. The more to the north, the less was the seasonal variation of the T-S curves (a and b of Fig. 6). But the seasonal variation of the surface water temperature in the north of the research area was more obvious than in the south, that is, it was low in Jan. and Apr. and high in Jun. and Oct..

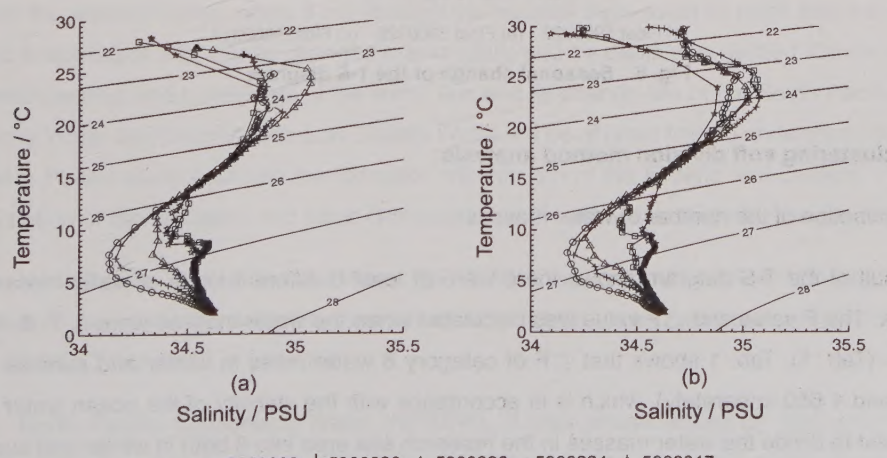

Fig. 5 Observed T-S curves in Jan. (a) and Jul. (b) of the 5 floats which located in different areas

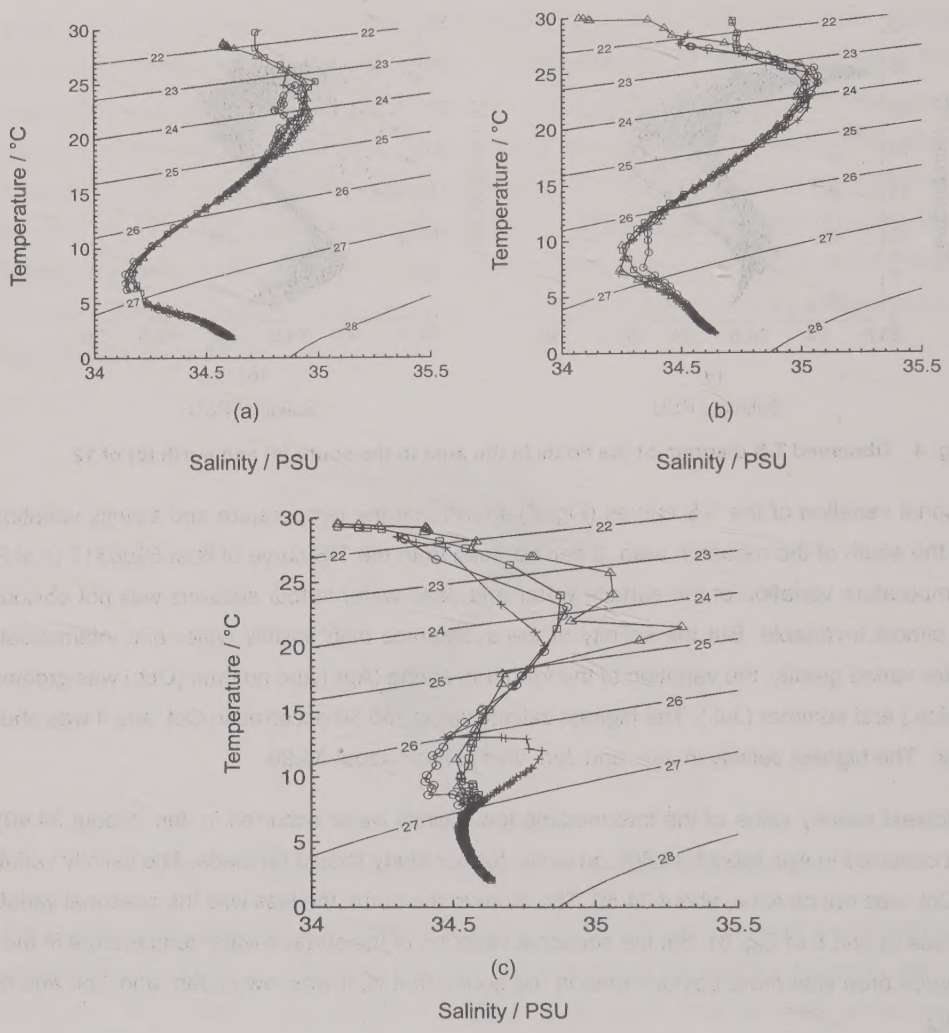

○ Jan; ┼ Apr; □ Jul; △ Oct;

(a) Float 5900222 (b) Float 5900226 (c) Float 5900317

Fig. 6 Seasonal change of the T-S diagram

2.2 Fuzzy clustering soft division method analysis

2.2.1 Determination of the number of water masses

The result of the T-S diagram shows there were at least 6 different kinds of water masses in the research area. The F value and △F value was calculated when the water masses were 6, 7, 8, 9, 10 and 11 separately (Tab. 1). Tab. 1 shows that △F of category 8 water mass in winter and summer was the largest (932 and 1 650 separately), which is in accordance with the stability of the ocean water masses. So, it is the best to divide the water masses in the research sea area into 8 both in winter and summer.

Tab.1 F values in the winter and summer to classify the number sets and the incremental ΔF values between the neighboring number sets

Season	Category 6		Category 7		Category 8		Category 9		Category 10		Category 11	
	F	ΔF	F	ΔF	F	ΔF	F	ΔF	F	ΔF	F	ΔF
Winter	11 435	-1 026	10 373	-254	10 118	932	11 051	379	11 431	99	11 530	249
Summer	9 239	1 38	93 78	-282	9 096	1 650	10 746	87	10 833	-609	10 224	-504

2.2.2 Basic feature of the water masses

Tab. 2 shows the critical feature values of temperature and salinity of the water masses of the research area, in which the depth range of the water mass distribution was estimated from the maps of plane and section distribution of the water masses.

Tab.2 Critical feature values and the depth range of the temperature and salinity of the water masses

Name of water mass	Abbreviation	Winter			Summer		
		Temperature / °C	Salinity	Depth / m	Temperature / °C	salinity	Depth / m
North Pacific Tropical Surface Water	NPTSW	23.97	34.95	<100	28.24	34.71	<100
North Pacific Subsurface Water	NPSSW	22.91	34.84	100 - 200	24.31	34.97	100 - 200
North Pacific Subtropical Mode Water	NPSTMW	12.77	34.49	200 - 350	12.48	34.52	200 - 350
North Pacific Intermediate Water	NPIW	7.17	34.22	300 - 750	6.94	34.21	300 - 700
North Pacific Deep Water	NPDW	3.55	34.56	>800	3.18	34.57	>800
Equator Surface Water	ESW	27.57	34.41	<100	29.03	34.09	<100
South Pacific Subsurface Water	SPSSW	18.00	34.75	100 - 280	19.05	34.81	100 - 300
South Pacific Intermediate Water	SPIW	5.09	34.47	350 - 850	5.14	34.51	350 - 950

Actually, almost all the sources of these water masses were not in the research sea area, except for the North Pacific Tropical Surface Water and Equatorial Surface Water. Especially the South Pacific Intermediate Low Salinity Water, of which the source was in the South Pacific Ocean near the Antarctic far away from the research area, when it cut through the equator from south to north into the North Pacific Ocean, its temperature and salinity changed dramatically, and it's depth was uplifted. Obviously, to have a better understanding and knowledge of the water flux and its change law of the South Pacific Subsurface High Salinity Water and Intermediate Low Salinity Water will be of great help to understand the variation of the Western Pacific warm pool and the formation mechanism of the El-Niño and La-Niña. Following is a brief description of the formation and basic characteristics of each water mass in the research sea area.

(1) North Pacific Tropical Surface Water (NPTSW). It was distributed above 100 meters in the north of the research sea area. The critical feature values of temperature and salinity were 23.97 °C and 34.95 in winter, 28.24 °C and 34.71 in summer.

(2) North Pacific Subsurface Water (NPSSW). It was characterized by high salinity. The high salinity water distributed in the thermocline under the surface water in the north of the research area. The depth of the water mass was 100 m to 200 m. The critical feature values of temperature and salinity were

22.91 °C and 34.84 in winter, 24.31 °C and 34.97 in summer. The source of NPSSW was at the surface centered by 23°N, 172°30′E, which was roughly corresponding to the North Pacific sub-high pressure sea area. Obvious salinity uplift occurred and evaporation was far greater than precipitation. After its formation, it scattered gradually westward and southward along the thermocline between 18.5 - 27.0 °C to the research sea area [10].

(3) North Pacific Subtropical Mode Water (NPSTMW). NPSTMW was formed by the anticyclone convergence sinking water between 29° - 33°N [10-11], and located under NPSSW between 200 to 350 meters. Its upper and lower boundaries were bending upward from north to south, and its thickness decreased. The critical feature values of the temperature and salinity of NPSTMW in winter was 12.77 °C and 34.49, 12.54 °C and 34.52 in summer.

(4) North Pacific Intermediate Water (NPIW). It was characterized by low salinity and mainly distributed under the NPSTMW, the depth of which was from 300 to 700 meters. The critical feature values of temperature and salinity were 7.17 °C and 34.22 in winter, 6.94 °C and 34.21 in summer. NPIW was formed in the Sub-Arctic front belt, and then sank in the southern margin, and moved southward through the Kuroshio front, joined subtropical anticyclone circulation and was brought to the Northwest Pacific Ocean [10]. After entering into the research sea area, its upper and lower boundaries bended more upward when it moved further south, and the thickness decreased , which was obviously resulted from the strong upwelling of the cold water near the equator countercurrent trough and the wedging of the North Pacific deep water.

(5) North Pacific Deep Water (NPDW). There was a large stable water body under the intermediate layer of the research area, that is NPDW. The critical feature values of temperature and salinity of NPDW were 3.55 °C and 34.56 in winter, 3.18 °C and 34.57 in summer.

(6) Equator Surface Water (ESW). It was characterized by high temperature and low salinity, and distributed above 100 meters of the southern research area. The critical feature values of temperature and salinity were 27.57 °C and 34.41 in winter, 29.03 °C and 34.09 in summer.

(7) South Pacific Subsurface Water (SPSSW). High salinity is the main feature. It distributed in the thermocline below the surface water in the south of the research sea area. The largest depth of the SPSSW was up to 300 meters. The critical feature values of temperature and salinity of SPSSW were 18.00 °C and 34.75 in winter, 19.05 °C and 34.81 in summer. It formed in the subtropical high pressure convergent subsidence area of the southern hemisphere, and then scattered westward and northward along the thermocline into the research sea area [10].

(8) South Pacific Intermediate Water (SPIW). It was characterized by low temperature and low salinity , and distributed under the subsurface of the southern research sea area with the largest depth of 900 meters. The critical feature values of temperature and salinity of SPIW was 5.09 °C and 34.47 in winter, 5.14 °C and 34.51 in summer. It was formed by Antarctic convergence sinking water in cool half year, and moved northward to the northern most north at about 15°N. It was distributed between 300 m to

950 m.

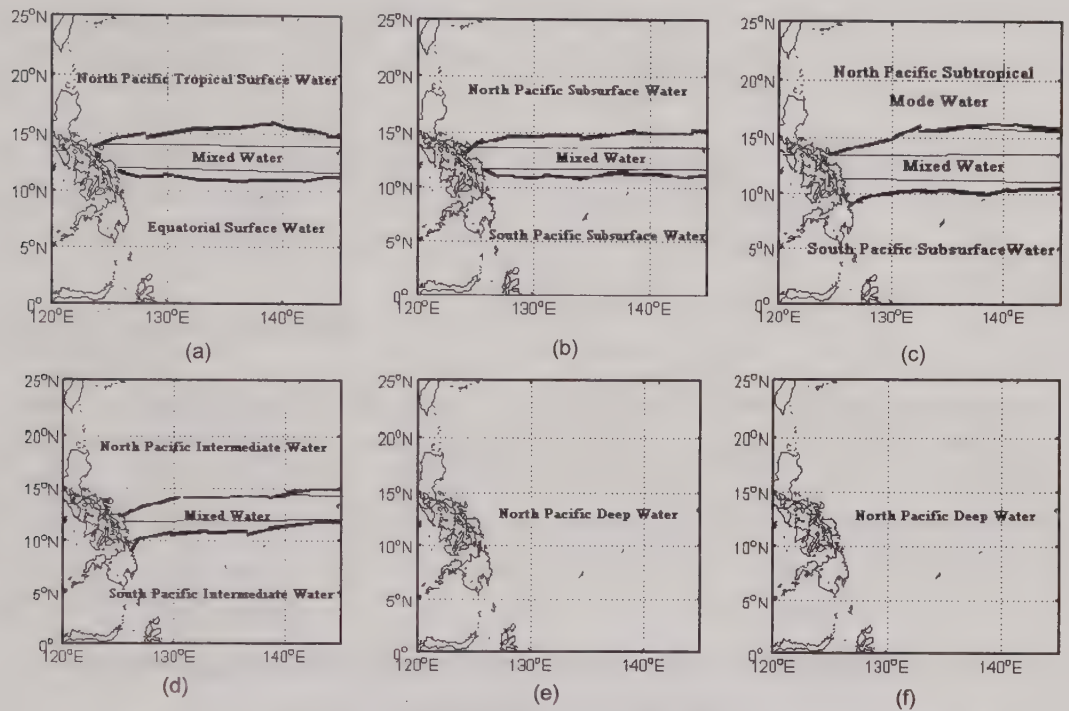

(a) 20 m (b) 150 m (c) 250 m (d) 500 m (e) 1 000 m (f) 1 500 m

Fig. 7 Horizontal distribution of water masses in winter

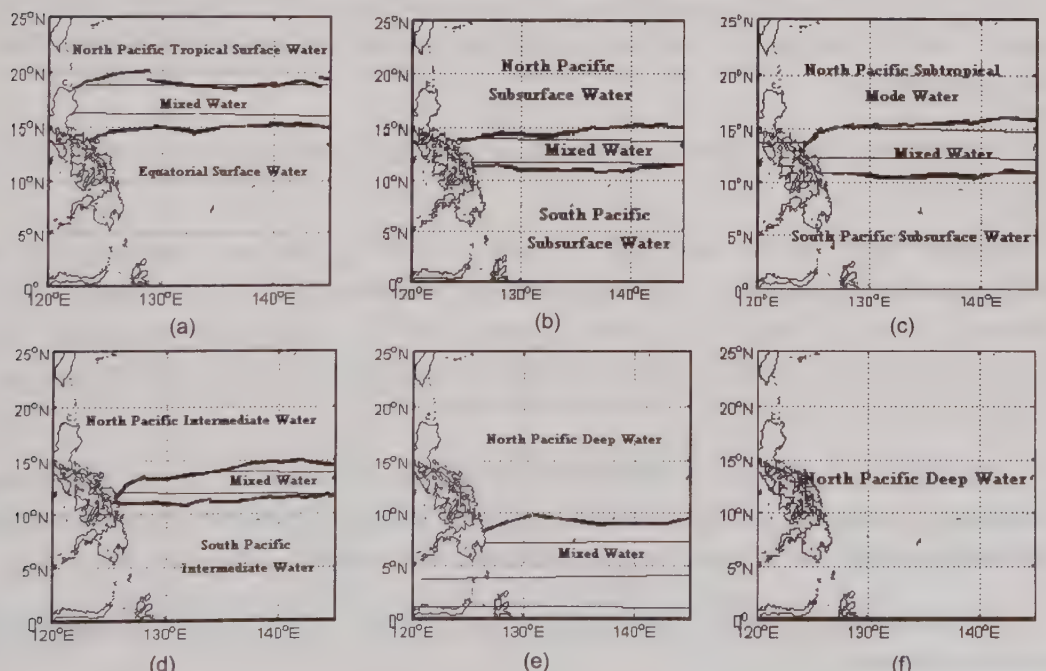

(a) 20 m (b) 150 m (c) 250 m (d) 500 m (e) 1 000 m (f) 1 500 m

Fig. 8 Horizontal distribution of water masses in summer

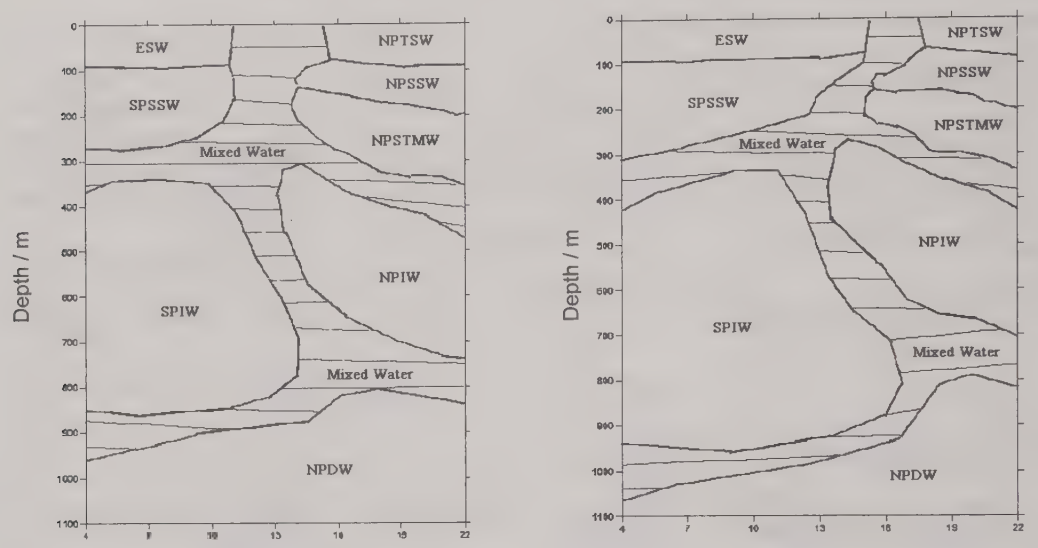

Fig. 9 Distribution of water masses in the 137 °E section (a) winter (b) summer

2.2.3 Water mass distribution and seasonal variation

Fig. 7 and Fig. 8 show the water mass distribution at the depth of 20, 150, 250, 500, 1 000 and 1 500 meters in winter and summer. Fig. 9 shows the water mass structure at section 137°E (Section P2 and P3) in winter and summer.

The distribution and variation of the water masses in each layers in winter and summer showed following features:

20-meter Layer. There was NPTSW in the north of the research sea area, and ESW in the south. Mixing water area was greater in summer than in winter. It moved northward. NPTSW existed only to the north of 20°N (Fig. 7a and Fig. 8a). The critical feature values of temperature of surface water in summer were greater than those in winter, and the critical feature value of salinity of surface water in summer was smaller than that in winter.

150-meter Layer. There were NPSSW and SPSSW both in winter and summer. The latitude of mixing water in winter and summer was almost the same (Fig. 7b and Fig. 8b). The critical feature values of temperature and salinity of subsurface water in summer were greater than those in winter.

250 to 500-meter Layer. NPSTMW existed here both in summer and winter. The largest depth in winter was greater than in summer.

500 to 1 000-meter Layer. This layer mainly consisted of NPIW and SPIW. NPIW distributed to the north of SPIW. The mixing water of these two water masses was pushed southward near the shore, since

NPIW was schlepped by the southward Mindanao current. The critical feature value of temperature of NPIW in summer was smaller than that in winter, but those of salinity of NPIW in summer and winter were almost the same. The critical feature value of temperature of SPIW in summer was greater than that in winter.

1 500-meters Layer. This layer was occupied by NPDW both in winter and summer (Fig. 7f and Fig. 8f). The critical feature value of temperature of NPDW in summer was smaller than in winter, and the critical feature value of salinity was almost unchanged in summer and winter.

3 Discussion and conclusion

Tab.3 shows the critical feature values of temperature and salinity and the depth range of all the water masses in winter in the research sea area. Results by XU Bochang were obtained from the CTD data collected in the 1st cruise of Tropical West Pacific Air-Sea Interaction Research project (Dec. 1985 to Feb. 1986) with the method of fuzzy clustering soft division [10], while results by LI Xulu were obtained from the CTD data got in China-USA joint TOGA investigation cruise in Nov. 1986 with the method of fuzzy clustering rigid division [3].

Tab.3 Ranges of temperature, salinity and depth of the water masses in winter from former studies and our work

Name of water mass		NPTSW	NPSSW	NPSTMW	NPIW	ESW	SPSSW	SPIW
XU Bochang	Temperature	—	19.7-24.8	14.6-18.7	4.2-10.9	26.8-29.2	13.8-29.3	4.6-6.1
	Salinity	—	34.9-35.1	34.5-34,8	34.2-34.5	34.2-34.9	34.9-35.4	34.4-34.6
	Depth	—	110-210	100-350	200-1000	<130	100-300	500-1000
LI Xulu	Temperature	24.3-29.6	14.0-27.0	—	3.8-14.0	25.7-30.5	14.0-27.4	3.8-11.2
	Salinity	33.9-34.8	34.5-35.0	—	34.1-34.6	33.6-34.6	34.5-35.3	34.5-34.6
	Depth	<130	100-400	—	250-1000	<110	50-250	200-1200
Our study	Temperature	20.5-27.7	20.3-26.3	10.0-15.2	4.1-11.4	23.9-29.3	15.4-22.3	2.8-7.6
	Salinity	34.9-35.1	34.7-34.9	34.4-34.6	34.1-34.3	34.2-34.6	34.6-35.2	34.4-34.6
	Depth	<100	100-200	200-350	300-750	<100	100-280	350-850

Fig. 10b shows the characteristics of the water mass distribution concluded by XU Bochang in section 130°E (8° - 18°N), in which WTS represents the Western Tropical Surface water (That is NPTSW and ESW in this paper), NSH the North Pacific Subsurface water, NST the NPSTMW, and NMS the NPIW. Fig. 10c shows the distribution characteristics of water masses concluded by LI Xulu in section 130°E (8° - 18°N), in which WPTSW represents the West Pacific Surface water (that is NPTSW and ESW in this paper), NPSW the NPSSW, NPIW the NPIW, and AAIW the AIW (SPIW in this paper).

Tab.3 shows that the conclusion of the paper coincides basically with the results from the previous study. It should be mentioned that the previous results were based on the data of one section or several

sections obtained in a single cruise, while those in this paper were based on the data of all Argo floats which worked in the research sea area all the time in winter, which might resulted in the differences of the critical feature values of temperature and salinity from the previous study.

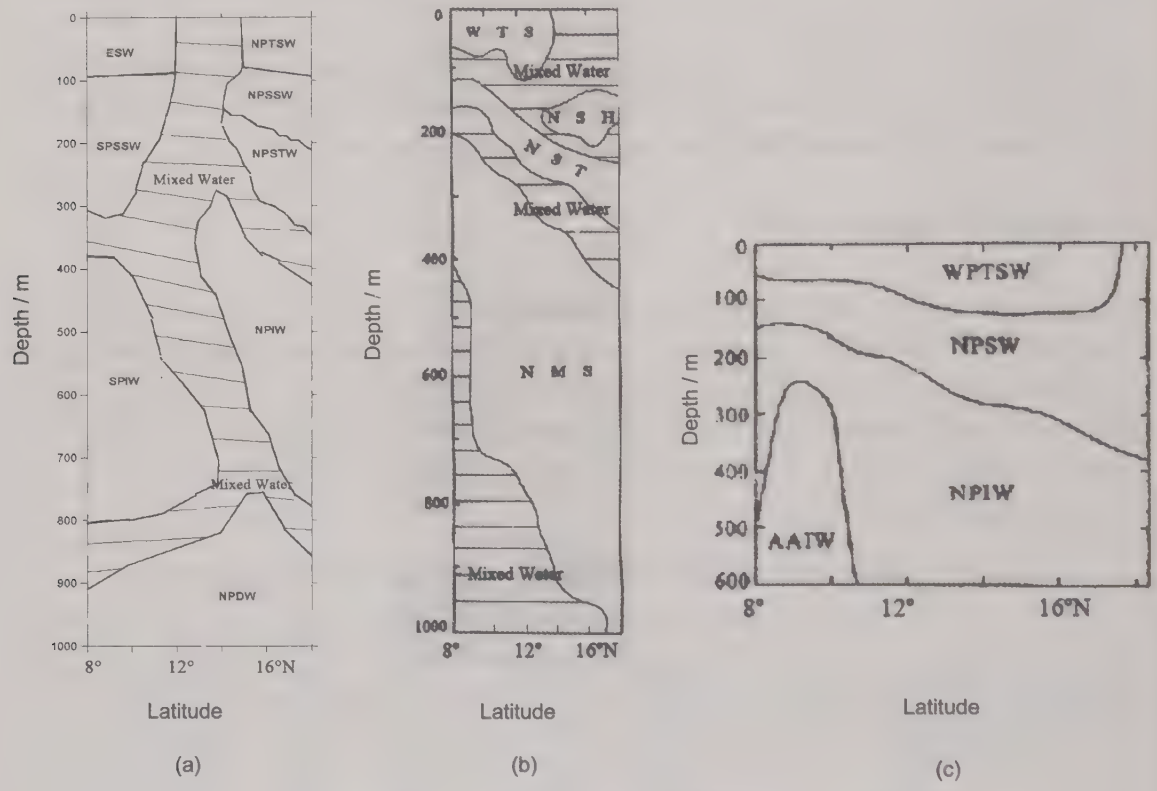

Fig. 10 Distribution of water masses in 130°E section in winter

(a) The result of our study (b) Xu Bochang's result (c) Li Xulu's result

However, comparison of the water mass distribution of Fig. 10b, Fig. 10c with that at section P1 (winter, near 130°E) shows that the distribution range was roughly the same. The difference lies in the South Pacific water mass in section 130°E, which previous study didn't find. The Argo floats provide much more 10d time scale data from the interior of the ocean from wider area, which makes it possible to make more detailed analysis and division on the whole ocean water mass, and the results will be more representative.

Acknowledgments

This work was Supported by the specical scientific research project for the welfare of the State Oceanic Administration for 2007. (No.200706022).

References

[1] Li Xulu. Water mass features in the upper part of section along 8°N in western tropical Pacific Ocean and their responses to El Niño [J]. Journal of Oceanography in Taiwan Strait. 1993, 12(1): 41 - 47.

[2] Li Xulu. Water mass features in the upper part of section along 18°20'N in western tropical Pacific Ocean and their responses to El Niño and anti- El Niño [J]. Acta Oceanologica Sinica. 1993, 15(4): 12 - 18.

[3] Li Xulu. Water mass features in the upper part of section along 130°E in western tropical Pacific Ocean and their responses to El Niño and anti- El Niño [J]. Marine Science Bulletin. 1993, 12(5): 9 - 14.

[4] Xu Jianping. Exposure of Argo Global Ocean Observation [M]. Beijing: China Ocean Press. 2002.

[5] Li Fengqi, Su Yusong. The analysis of Water mass [M]. Qingdao: Qingdao Ocean University Press. 2000.

[6] Chen Shangji, Ma Jirui. Marine Data Processing and Analysis Methods and their Application [M]. Beijing: China Ocean Press. 1991.

[7] Du Bing, Zhang Aijun. Water mass features in the upper part of section along 165°E in western tropical Pacific Ocean and their responses to El Niño and anti- El Niño [J]. Marine Science Bulletin. 1995, 14(2): 10 - 19.

[8] Lou Shibo. Fuzzy mathematics [M]. Beijing: Science Press. 1985.

[9] Xu Dongfeng, Liu Zenghong, Liao Guanghong. The influence of typhoon on the sea surface salinity in the warm pool of the western Pacific [J]. Acta Oceanologica Sinica. 2005, 27(6): 9 - 15.

[10] Cao Jiping, Tropical West Pacific Air-Sea Interaction Research [M]. Beijing: China Ocean Press. 1993.

[11] SU GA T, HANAWA K, TOBA Y. Subtropical mode water in the 137°E section [J]. J. Phys. Oceanogr., 1989, 19: 1 605 - 1 618.

应用 Argo 资料分析西北太平洋冬、夏季水团

孙朝辉，许建平，刘增宏， 童明荣，朱伯康

（卫星海洋环境动力学国家重点实验室，国家海洋局第二海洋研究所，浙江 杭州 310012）

摘 要：应用 Argo 剖面浮标观测的温、盐度资料，分析了西北太平洋海域冬、夏季的温、盐度分布、水团结构及其分布。首先采用 T-S 点聚图法分析了该海域水团分布的基本情况，由点聚分析结果可知，该海域至少存在 6 种以上水团；再用模糊聚类软化法对水团作进一步划分，分别计算了该海域 6 至 11 类水团的 F 和△F 值，结果表明，冬、夏季的△F 值都以划分为 8 类时为最大，这与大洋水团的稳定性是一致的，因此，该海域冬、夏季水团以划分为 8 类最佳，它们分别是北太平洋热带表层水、北太平洋次表层水、北太平洋中层水、北太平洋副热带模态水、北太平洋深层水和赤道表层水，以及南太平洋次表层水和南太平洋中层水。

关键词：Argo 剖面浮标；T-S 点聚；水团分析；西北太平洋

An Assessment of Urban Heat Island Effect using Remote Sensing Data

WANG Guiling[1], JIANG Weimei[2], WEI Ming[3]

1. *Institute of Meteorology, PLAUST, Nanjing* 211101, *Jiangsu, China;*

2. *Department of Atmospheric Sciences, Nanjing University, Nanjing* 210093, *Jiangsu, China;*

3. *Sino-American Cooperative Remote Sensing Center, NUIST, Nanjing* 210044, *Jiangsu, China*

Abstract: Characteristics of urban heat island (UHI) effect and its cause are investigated by using MODIS data in April 2004. Surface parameters from the MODIS data have surface temperature (t_s), albedo(α), and normalized difference vegetation index (NDVI). Their heterogeneities over urban and rural area are analyzed based on land cover classification, and their relations are also presented in order to explain the UHI effect. The results show that there exists obvious the UHI effect. T_s over urban areas are by 10.83 % higher than those over rural area，and NDVI and α over urban area are by 62 % and 18.75 % less than those over rural area, respectively. Surface temperature has significantly negative correlation with NDVI and their correlation coefficient is -0.73. Correlation between NDVI and albedo is determined by the spectrum of light. Difference in vegetation cover is the primary cause of the UHI effect.

Keywords: remote sensing; MODIS; urban heat island; surface temperature; NDVI; albedo

Introduction

Urban development usually gives rise to a dramatic change of the Earth's surface, as natural vegetation is removed and replaced by non-evaporating and non-transpiring surfaces such as metal, asphalt, and concrete. This alteration inevitably results in the redistribution of incoming solar radiation, and induces the urban-rural contrast in surface radiance and air temperatures. The difference in ambient air temperature between an urban area and its surrounding rural area is known as the effect of UHI. It is a meteorological phenomenon developing with the growth of urbanized areas, are increasingly affecting citizen's lives and health. The study will help us to better understand the UHI aspects and its causes, providing an important addition to conventional methods of monitoring the urban environment. It is important to urban expand and layout in order to lessen the UHI.

Studies on UHI phenomenon using satellite remote sensing data have been conducted for more than ten years. The methods are included the following types. Firstly, UHI actuality and its dynamic change are analyzed using long term meteorological record over urban and suburban area. Secondly, the causes of UHI characteristics are explained by the remote sensing or aerial photos. Thirdly, the numerical model is used to simulate the UHI effect. Fourthly, some stations are set to measure UHI. The recent

Received on January 23, 2008

increasing availability of remote sensing technique is an efficient way to survey UHI periodically for long time. Roth (1989) and Gallo (1993) used remote sensing techniques to compare the UHI effect to vegetation index [1,2].Owen(1998) used fractional vegetation cover and surface moisture availability to study the impact of urbanization in and around State College, PA [3]. Streutker (2003) analyzed the growth of UHI and successfully quantified the UHI of Houston, TX taken 12 years apart [4]. All the above studies used National Oceanic and Atmospheric Administration (NOAA) AVHRR data. The 1.1 km spatial resolution of these data was found suitable for the surface temperature mapping over urban area and used to study the surface UHI. UHI has been also studied with more fine resolution satellite data such as Landsat TM, SPOT in many cities such as the Zhujiang Delta in China, Lódź in Poland, Granada in Spain over the past few years. But such remote sensing data have low temporal resolution and a shorter data record [5-8].

MODIS is a key instrument aboard the Terra (EOS AM) and Aqua (EOS PM) satellites. Terra MODIS and Aqua MODIS are viewing the entire Earth's surface every 1 to 2 days, acquiring data in 36 spectral bands. These data will improve our understanding of global dynamics and processes occurring on the land, in the oceans, and in the lower atmosphere. MODIS is playing a vital role in the development of validated, global, interactive Earth system models able to predict global change accurately enough to assist policy makers in making sound decisions concerning the protection of our environment. Most recent researches were about the regional or global scale climatic and environmental changes and seldom on the UHI using MODIS data [9-13].

Surface temperatures derived from satellite are believed to correspond more closely with the canopy layer heat island, although a precise transfer function between the surface temperature and the near ground air temperature is not yet available. Satellite information is the only source for determing of the surface temperature (t_s) at macro level over a region. In this study, we use the MODIS and other supplementary data to study the characteristics of the UHI and its causes.

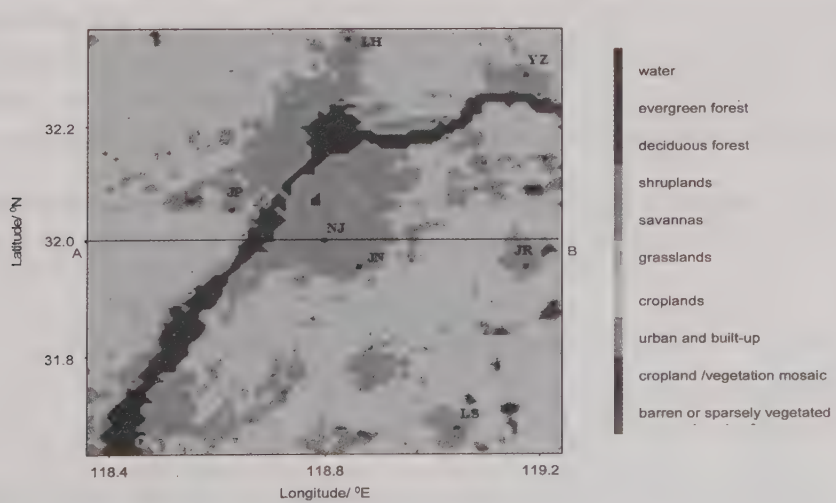

Fig.1 Land cover classification from MODIS in 2004 and locations of automatic weather station

MODIS data are pretreated firstly by the method of overlapped mobile window in Geo-statistics to eliminate abnormal values due to cloud [14,15]. MODIS land surface temperature products are compared with monthly mean t_s from seven Automatic Weather Stations (AWSs) to validate them. Then, the parameters in three broadbands (0.3 - 0.7 μm, 0.7 - 5.0 μm, and 0.3 - 5.0 μm) are used to compute the surface albedos in the broadbands with BRDF model. Finally, the difference and correlation analysis of t_s, NDVI and albedos between the urban and rural area are performed depending on land use pattern. The urban heat island in the study area is synthetically analyzed by comparing the distribution of t_s, NDVI and albedos over urban areas and non-urban areas.

1 Study area

The study area considered in this paper encompasses an area of 83 × 83 km^2 centered at coordinates 118.8°E, 32.0°N (Nanjing, China). This area includes Nanjing urban area and its suburban counties. Most of the terrain heights are very low in the region and mountains are distributed mainly in the east and southwest areas.

The study area is very heterogeneous, comprising of water, cropland, and forest as well as urban and built-up. Fig. 1 shows the land cover classification map in study area (2004) and the locations of seven AWSs. From Fig. 1 it is easily seen that the Yangtze River runs across the urban zone, and the Xuanwu Lake and the Purple Mountains locate in the central part of the area, with large green cover of semi-natural forest. A transect crossing the centre of the area (AB) is chosen from west to east.

2 Data set description

2.1 Satellite remote sensing data

Satellite remote sensing has potential utility for this landscape scale characteristic analysis because of the global continuity of observation. Here we choose MODIS satellite data. A series of high-level land surface products have been generated by the MODIS land science team, which are all operational and can be downloaded from the following web site: http://edcimswww.cr.usgs.gov/pub/imswelcome/.

Tab.1 Selected MODIS products of 2004 and their spatial and temporal resolutions

ESDT	Product Name	Temporal Resolution/d	Starting DOY of Each Granule	Scale / km
MOD11A2	Land Surface Temperature	8	089, 097,105,113,121	1
MOD12Q1	Land Cover	96	/	1
MOD13A2	Vegetation Indice	16	081,097,113	1
MOD43B1	Surface Albedo	16	081,097,113	1

The selected products are listed in Tab.1. ESDT is the short name for Earth science data type. DOY

means Julian day of the year. Temporally, these data cover April 2004 (spring season). We have included MODIS data from the period March 21th (DOY 81) to May 8th (DOY 121). The time period covers 40 days (five 8-day periods and three 16-day periods). The 96-day land cover product included here does not specifically overlap with the spring season. The product "MOD11A2" in the MODIS Land Discipline is defined as the "land surface temperature (LST)" over the global land surface every 8 days with 1 km-resolution. Other products used include the land cover product "MOD12Q1" and NDVI product "MOD13A2".

The accuracy specification for MODIS LST is 1K at 1 km resolution under the clear sky conditions. It can be validated by field measurements over flat uniform land surfaces. The accuracy specification for land-surface emissivity retrieved from MODIS data is 0.02 for bands 29, 31 and 32, and 0.05 for bands 20, 22, and 23. The MOD13A2 are standard products designed to be fully operational at launch. The MOD12Q1 product provides a suite of land covers with the primary classification in the IGBP (International Geosphere Biosphere Programme) scheme. Each of these classification schemes is accompanied by the assessments of its quality or confidence. More information about the MODIS products can be found from the web site http://modis.gsfc.nasa.gov/data.

All data are in HDF (Hierarchical Data Format) format and are provided in ISG (an Integerized Sinusoidal Grid) projection. While the projection becomes increasingly sheared with distance from the Greenwich meridian, the data are converted to Lambert conformal projection and the format from original HDF to a flat binary format by the MODIS Reprojection Tool (MRT v2.4 Beta).

2.2 Meteorological Data

In this study, seven AWSs are selected and their locations are listed in Tab.2. Monthly surface temperature in each hour in April 2004 are obtained from the AWSs. STID is the station code number of AWS.

Tab.2 Locations of the automatic weather stations

STID	ST Name / Abbr.	Longitude / °E	Latitude / °N	Terrain height / m
58235	Liu He (LH)	118.85	32.20	12.2
58237	Jiang Pu (JP)	118.37	32.03	8.9
58238	Nan Jing (NJ)	118.8	32	12
58242	Yi Zheng (YZ)	119.17	32.28	10.5
58333	Jiang Ning (JN)	118.51	31.57	22.1
58340	Li Shui (LS)	119.02	31.39	25.5
58344	Ju Rong (JR)	119.10	31.57	26.1

3 Surface temperature from MODIS product and its validation

Some hot spots, or urban heat islands, can be easily identified (shown in Fig. 2). The terrain height is also drawn in the same map in order to explain the distribution pattern of the surface temperature. The most extensive UHI is distributed left of the central part of the area which is business zone and can be seen in the centre of some small town around the area. However, no extensive UHI exists in the east of the city, where the Purple Mountains are located. Forest and agricultural landcover there restrict the development of UHI. The maximum difference of t_s between urban and suburban is about 10 °C, and the average difference of t_s is about 2.29 °C in daytime.

Interpreting thermal data and images of t_s distribution over an area is often not an easy job, because of many complex factors involved. The most influential factors affecting the heat island are the distribution of surface cover characteristics, and urban morphology, such as building materials, geometry, and density. Each component surface in urban landscapes possesses a unique radiative, thermal, moisture, and aerodynamic properties, and relates to their surrounding environment. The myriad of the component surfaces and the spatial complexity, when mosaicked, create a limitless array of energy balance and microclimate systems, confiscating urban meteorologists from drawing any general conclusion [2]. Land covers are more effective in developing UHI.

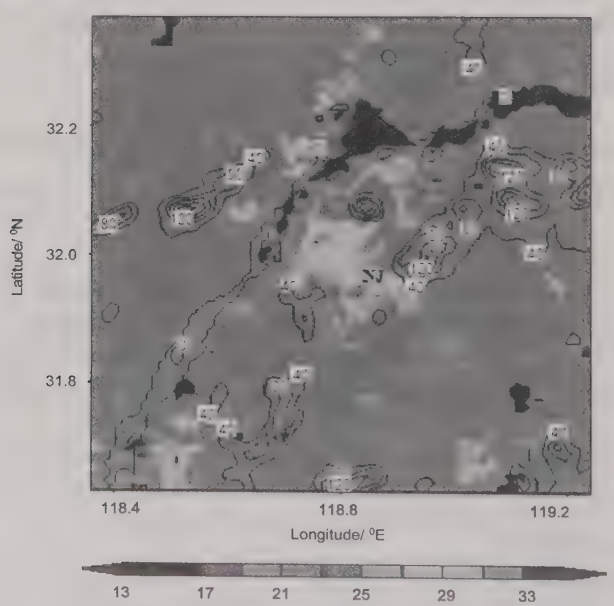

Fig.2 Terrain height (m) and monthly average surface temperatures t_s from MODIS at about 10:30 LT(local time) in daytime in April 2004 .

The monthly average t_s from AWS and MODIS in daytime are compared. Tab. 3 is the comparison of the monthly average t_s derived from MODIS with AWS valid at 10:30 hour local time in day. Δt_s is the

difference of t_s between MODIS and AWS. The monthly average t_s derived from MODIS are generally in good agreement with those from AWSs. The relative error δ is about -8.76 % - 2.39 %, most of which is negative. It can be concluded that the monthly average t_s from MODIS is somewhat lower than the values of AWS.

Tab.3 Comparison of monthly average t_s at about 10:30 LT in April 2004 from MODIS with AWS

ST	t_s/ °C		Δt_s / °C	δ/ %
	MODIS	AWS		
LH	26.04	28.54	-2.50	-8.76
JP	26.08	25.47	0.61	2.39
NJ	27.50	27.53	-0.03	-0.11
YZ	26.18	28.18	-2.00	-7.10
JN	26.68	27.09	-0.41	-1.51
LS	28.04	27.90	0.14	0.50
QR	27.30	28.72	-1.42	-4.94

4 Relations of α,T_S and NDVI

4.1 NDVI

This research uses NDVI to analyze the distribution of temperature in green area and non-green area. Generally speaking, NDVI has the value of 0(Min) - 1(Max) through the following equation.

$$NDVI = (r_{nir} - r_r)/(r_{nir} + r_r))$$

r_{nir} and r_r are surface reflectances in the NIR and red bands, respectively.

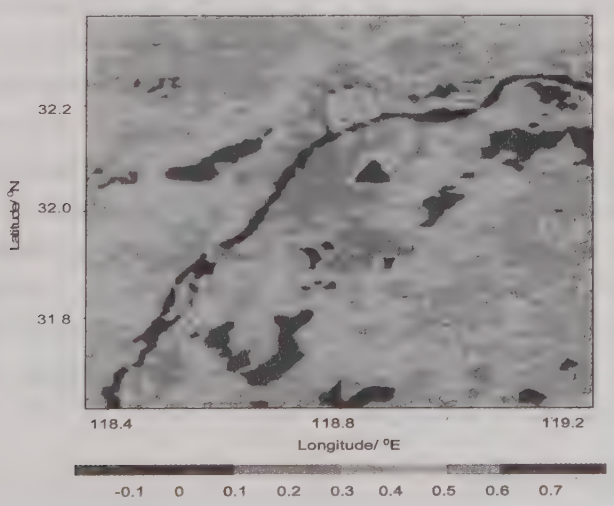

Fig.3 Monthly average NDVI from MODIS in April of 2004

It can be seen from the NDVI map (Fig.3) that all the urban or built-up areas have a relatively low NDVI, ranging from 0.2 to 0.4. The same is true in small towns, which are related to the sparse vegetation. The mean difference of NDVI between urban and rural area is 0.31.

4.2 albedo (α)

The parameters in three broadbands (0.3 - 0.7μm, 0.7 - 5.0 μm, and 0.3 - 5.0 μm) are used in this paper in a forward version of the model to compute the integrated black-sky (at some solar zenith angle) and white-sky albedos. Alternately, the parameters can be used with a simple polynomial to easily estimate the black-sky albedo (completely direct beam) with good accuracy for any desired solar zenith angle[17]. The polynomial is as follows:

$$\alpha_{bs}(\theta_i,\lambda) = f_{iso}(\lambda)(g_{0iso} + g_{1iso}\theta_i^2 + g_{2iso}\theta_i^3) + f_{vol}(\lambda)(g_{0vol} + g_{1vol}\theta_i^2 + g_{2vol}\theta_i^3) + f_{geo}(\lambda)(g_{0geo} + g_{1geo}\theta_i^2 + g_{2geo}\theta_i^3) \quad (1)$$

where θ_i, λ are the solar zenith angle, the spectral band. Similarly, the white-sky albedo (completely diffuse beam) can be computed by using the equation:

$$\alpha_{ws}(\lambda) = f_{iso}(\lambda)g_{iso} + f_{vol}(\lambda)g_{vol} + f_{geo}(\lambda)g_{geo} \quad (2)$$

The appropriate constants are from the MODIS BRDF/Albedo Product (MOD43B) User's Guide as mentioned above. The albedo, $\alpha(\lambda,\theta_i)$, under actual atmospheric conditions can also be modeled quite accurately as an interpolation between the black-sky albedo and white-sky albedo as a function of the fraction of diffuse skylight $s(\theta_i,\tau(\lambda))$, which, in turn, is a function of optical depth $\tau(\lambda)$.

$$\alpha(\lambda,\theta_i) = (1 - s(\theta_i,\tau(\lambda))\alpha_{bs}(\lambda,\theta_i) + s(\theta_i,\tau(\lambda))\alpha_{ws}(\lambda) \quad (3)$$

The fraction of diffuse skylight is calculated through a look-up table downloaded from http://geography.bu.edu/brdf/userguide/tools.html, which was precalculated with the 6S code for seven MODIS land spectral bands plus three broadbands. The optical depth $\tau(\lambda)$ is assumed for the three broadbands as a constant 0.5, and the solar zenith angle is at local solar noon. The error of albedo caused by $\tau(\lambda)$ is very small, about 0.003 [19]. The urban albedo is the area-averaged values over all urban areas, and the rural albedo is the area-average albedo over other land cover type areas. Fig. 4 is the monthly average albedo in total broadband (0.3 - 5.0 μm) from MODIS in April 2004. The average albedo over urban area is about 0.13 in the study, which is consistent with other researches. Validating albedo products is important because their accuracy is critical to the scientific community for their applications. Some scientists have performed initial validations of land surface albedo products based on the up-scaling methods. Some preliminary validation results show that these products are reasonably accurate, with typical absolute error of less than 5 % [15].

4.3 Analysis of urban heat island

To show the distribution of the urban heat islands, albedos in three broadbands (0.3 - 0.7 μm, 0.7 -

5.0 μm, and 0.3 - 5.0 μm), t_s and NDVI in daytime variations along the transect AB (Fig.1) are drawn in Fig. 5. It should help us to understand how industrial development and infrastructure construction have altered the urban thermal characteristics. It exhibits numerous "peaks," "valleys," "plateaus," and "basins," indicating the heterogeneous nature of surface temperature along the line. Factors such as the spatial pattern of different land-cover classes, the occurrence of water bodies, building, and the division of the city's functional districts, among many others, may have affected the development of UHI. Visually reviewing the variations among the land covers reveals that the t_s "peaks" occur over urban and building areas. The UHI pattern becomes visible.

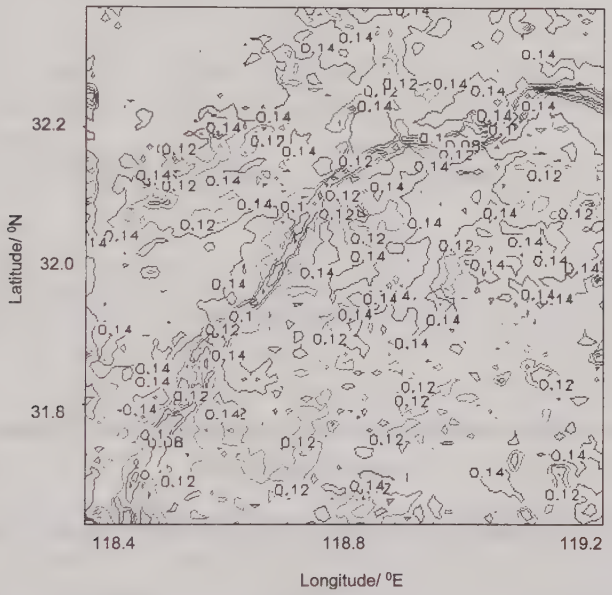

Fig.4 Monthly average albedo in total broadband (0.3 - 5.0 μm) from MODIS in April 2004

Albedo over urban area is less than that over the rural. Correlation between albedo in near infrared broadband (0.7 - 5.0 μm) and NDVI is positive, their correlation coefficient is 0.83, but it is -0.80 in the visible (0.3 - 0.7 μm). Albedo in the visible over urban area is larger than that over rural area, but is less in the NIR and in the total (0.3 - 5.0 μm).The result can be explained that the reaction of vegetation to sun light in wavelength is quite different. Albedo in the visible (0.3 - 0.7 μm) over the area with high density vegetation is lower than that over sparse vegetation. Because vegetation absorbs the light in the visible for photosynthesis, but it absorbs hardly in near infrared broadband and reflect most of it. Therefore albedo in near infrared broadband is larger. There is few vegetation over urban area and NDVI over urban area is always less than that over the rural. We can see from the figure that there is a negative correlation between NDVI and t_s which has also been observed by several researchers for various types of ecosystems [14-17]. The correlation coefficient between t_s and NDVI reaches -0.73. NDVI presents spectral reflectance properties and density of vegetation, surface temperature, on the other hand, is related to water and energy balance determined by soil moisture availability, amount of evapotranspiration and local climate factors.

The inhomogeneities of urban/rural surface characteristics (such as t_s, albedo, NDVI) are analyzed based on MODIS data , and conclusions are shown in Tab. 4.

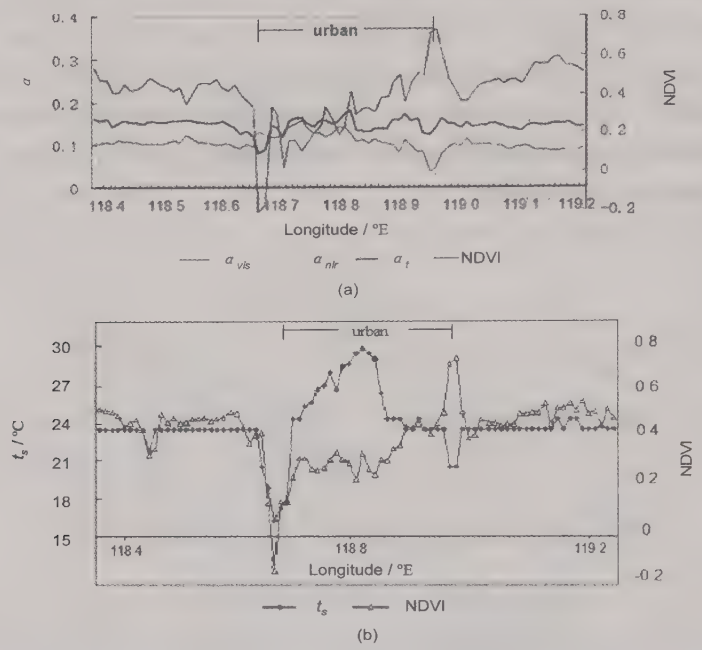

Fig. 5 Zonal profiles of NDVI and (a) albedos in three broadbands and (b) surface temperature t_s along transect AB in Fig.1

Tab. 4 Comparison of monthly average t_s, NDVI and α_t over urban area with those over rural area

	t_s/ °C	*NDVI*	α
urban	23.44	0.19	0.13
rural	21.15	0.50	0.16
difference（urban-rural）	2.29	-0.31	-0.03

t_s over urban area increase by 10.83 %,and difference between urban and rural area is about 2.29 ºC; NDVI over urban area is less than that over the rural. On the contrary NDVI and albedo over the urban are by 62 % and 18.75 % less than the rural, and the mean difference between urban and rural area is about 0.31 and 0.03, respectively.

5 Conclusion

(a) t_s from MODIS product well agrees with that of AWS, the and the UHI effect around Nanjing urban area is obvious by MODIS images.

(b) NDVI and t_s has correlation coefficients of -0.73. Correlation coefficient of NDVI and albedo is determined by spectrum of light, and that of albedo in near infrared broadband (0.7 μm - 5.0 μm) and

NDVI is 0.83, while that is -0.80 in the visible (0.3μm - 0.7 μm).

(c) t_s over urban area is larger than that over the rural area. t_s difference between urban and rural area is about 2.29 ºC, and NDVI and albedo over the urban area are by 62 % and 18.75 % less than those over the rural area, and the mean difference between urban and rural area is about 0.31 and 0.03, respectively.

The results indicate that surface characteristic parameters derived from remote sensing data will be regarded as one of effective methodologies to manifest urban heat island. The vegetation cover appears to be a primary cause of surface properties between two environments that are responsible for the difference between urban and rural surface. It can decrease the surface temperature over urban area and lessen effectively the UHI effect by enlarging vegetation cover and albedo. This study can also be the foundation for the further research on the UHI formation mechanism in term of the surface energy exchange using remote sensing data.

Acknowledgments

This work was supported by the project of National Natural Science Funding of China under grant No. 40075004.

Reference

[1] Roth M, Oke T R, Emery W J. Satellite derived urban heat islands from three coastal cities and the utilization of such data in urban climatology [J]. International Journal of Remote Sensing, 1989, 10 (11): 1 699 - 1 720.

[2] Gallo K P. The use of a vegetation index for assessment of the urban heat island effect [J]. International Journal of Remote Sensing, 1993, 14 (11): 2 223 - 2 230.

[3] Owen T W, Carlson T N, Gillies R R. An assessment of satellite remotely-sensed land cover parameters in quantitatively describing the climatic effect of urbanization [J]. International Journal of Remote Sensing, 1998, 19 (9): 1 663 -1 681.

[4] Streutker D R. Satellite-measured growth of the urban heat island of Houston, Texas [J]. Remote Sensing of Environment, 2003, 85 (3): 282 - 289.

[5] Klysik K, Fortuniak K. Temporal and spatial characteristics of the urban heat island of Lódź, Poland [J]. Atmospheric Environment, 1999, 33 (24/25): 3 885 - 3 896.

[6] Montaúez J P, Rodríguez A, Jiménez J I. A study of the urban heat island of Granada [J]. International Journal of Climatology, 2000, 20 (8): 899 - 911.

[7] Weng Q. Fractal analysis of satellite-detected urban heat island effect [J]. Photogrammetric Engineering & Remote Sensing, 2003, 69 (5), 555 - 566.

[8] Weng Q, Lu D, Schubring J. Estimation of land surface temperature-vegetation abundance relationship for urban heat island studies [J]. Remote Sensing of Environment, 2004, 89 (4): 467 - 483.

[9] Zhu A, Li C, Liu G, et al. Validation and application of MODIS remote sensing aerosol information in Beijing [J].

Acta Scientiae Circumstantiae, 2004, 24 (1): 86 - 90.

[10] Keith W O, Gordon B B, Schaaf C B, et al. Assessment of global climate model land surface albedo using MODIS data [J]. Geophysical Research Letters, 2003, 30 (8):1 443 - 1 447.

[11] Wei M, Wang G, Jiang W M, et al. Surface temperature analysis in urban area using MODIS [J]. Proceeding of SPIE, 2006, 6199:32 - 40.

[12] Wang G, Jiang W, Wei M, et al. Analysis of urban-rural albedo from MODIS over East China [J]. Proceeding of SPIE, 2006, 6199:123 - 134.

[13] Wang G. Study on Satellite Remote Sensing Parameterization of Surface Characteristics and Atmospheric Boundary Layer over Urban Rural Areas [D]. Nanjing: Department of Atmospheric Sciences Nanjing University, 2005.

[14] Wang Z. Geo-statistics and its application in ecology [M]. Beijing: Science Press, 1999.

[15] Sun H, Sun Z, Li Y. Meteorological Satellite Remote-sensing Spectral Characteristics of Fog [J]. Journal of Nanjing Institute of Meteorology, 2004, 27(3):289 - 301.

[16] Yang J, Yin Q, Gu S. Band combination research of city region hyperspectral remote sensing data in false color synthesis[J]. Journal of Nanjing Institute of Meteorology, 2005, 28(3):289 - 295.

[17] Lucht W, Schaaf C B, Strahler A H. An algorithm for the retrieval of albedo from space using semi-empirical BRDF models [J]. IEEE Trans Geosci Remote Sens, 2000, 38 (1): 977 - 998.

[18] Luo Y. Characteristics of atmospheric aerosol optical depth and its simulation of forcing on direct radiation and its climate effect over China[D].Beijing: Department of Geophysics Beijing University, 1998.

[19] Wang K, Liu J, Zhou X, et al. Retrieval of the surface albedo under clear sky over china and its characteristics analysis by using MODIS satellite [J]. Chinese Journal of Atmospheric Sciences, 2004, 28 (6):941 - 949.

[20] Liang S. Validating MODIS land surface reflectance and albedo products: methods and preliminary results [J]. Remote Sensing of Environment, 2002, 83 (1/2): 149 - 162.

[21] Xu X. A study of monthly-mean surface albedo of the Yangtze River Delta [J]. Chinese Journal of Atmospheric Sciences, 2002, 26 (3): 394 - 400.

[22] Zhou S, Shu J. Urban Climatology. Beijing: Meteorological Press, 1994.

[23] Nemani R, Running S. Estimation of regional surface resistance to evapotranspiration from NDVI and thermal-IR AVHRR data [J]. Journal of Applied Meteorology, 1989, 28 (4): 276 - 284.

[24] Smith R C G, Choudhury B J. Analysis of normalized difference and surface temperature observations over southeastern Australia [J]. International Journal of Remote Sensing, 1991, 12 (10): 2 021 - 2 044.

[25] Boegh E, Soegaard H, Thomsen A. Evaluating evapotranspiration rates and surface conditions using Landsat TM to estimate atmospheric resistance and surface [J]. Remote Sensing of Environment, 2002, 79 (2/3): 329 - 343.

[26] Yang B, Ding Y. An Experiment on Soil Moisture Monitoring Using an Improved Thermal Inertia Method[J]. Journal of Nanjing Institute of Meteorology, 2004, 27(2): 218 - 223.

城市热岛效应的卫星遥感分析

王桂玲[1]，蒋维楣[2]，魏 鸣[3]

（1. 解放军理工大学气象学院，江苏 南京 211101；2. 南京大学大气科学系，江苏 南京 210093；
3. 南京信息工程大学中美合作遥感中心，江苏 南京 210044）

摘 要：利用 MODIS 资料研究了 2004 年 4 月南京城市热岛特征及其影响因子，结合地表覆盖类型分析了植被归一化指数（Normalized Difference Vegetation Index，NDVI）、地表温度（T_s）、地表反照率（α）的城乡差异及其相互关系，探讨了城市热岛（Urban Heat Island，UHI）效应形成的机制。结果表明：南京城区存在着明显的城市热岛效应；城市平均 T_s 比乡村高约10.83 %；城市 NDVI 和 α 分别比乡村低约为62 %和18.75 %；NDVI 与 T_s 呈负相关，相关系数为-0.73，而 NDVI 与 α 之间关系与波段有关；城乡植被覆盖差异是造成 UHI 的主要原因，其次是地表反照率，通过提高植被覆盖率和地表反照率可以减小城市热岛效应。

关键词：卫星遥感；MODIS；城市热岛；地表温度；植被归一化指数；地表反照率

Development and Application of the GIS-Based Water Mass Analysis Integrated System

ZHANG Yuexia [1], MIAO Zhenqing [2], YAN Shiqiang [3]

1. *Second Institute of Oceanography, SOA, Hangzhou* 310012, *Zhejiang, China;*
2. *Zhejiang Ocean University, Zhoushan* 316004, *Zhejiang, China;*
3. *School of Engineering and Mathematical Science, City University, London*

Abstract: The research on water masses is always one important facet of Oceanography. I adopt the method of Fuzzy Density Clustering to analyse water masses. Meanwhile, I use Visual Basic 6.0 as developing platform and utilize the MapX components to develop the platform of GIS. By integrating the Water Masses Model compiled by FORTRAN language, and GIS using Tight Coupling, I develop an Integrated System. That makes all phases are finished in one condition, including the gain of computing grid, the pick-up and analysis of data, the choice of parameters and resetting, the computing of model, and the result's visualization. It improves the efficiency of the data analysis and decision-making. Finally, this system is applied in the Zhoushan fishing ground and adjacent region. The results are satisfying.

Keywords: Water mass; GIS; Model integration; the Zhoushan fishing ground

Introduction

Water mass analysis is always one important facet of Oceanography, and its primary mission is the identification and division of the water mass. At present, the main methods of water mass analysis contain: geography analysis, consistency analysis and clustering analysis. Chinese scholars have gained good fruit in the water mass analysis by using these methods [1-7]. However, the division of the water mass still depends on the hand-drawn analysis map drawn by the researcher with rich experiences, which is time-consuming and the result has a bad quantitative accuracy.

After the GIS appeared in the 1960s, it is always the most energic technic, with the fastest development, in the Earth Science and Earth System Science. With its main functions of collection, storage, management, analysis and display of geographic information, GIS brings a new vision for the research of the water mass analysis. However, both the current model of water masses and the integration of GIS are simple secondary exploitations based on GIS platform, actualizing basic data exchange. The GIS platform is just considered as a carrier for data transfer [8].

With the development and maturity of the component GIS, the models and GIS functions can be organically integrated, and can get rid of GIS platform software, which has drawn greater attention [9-12].

Received on November 19, 2007

This paper attempts to establish an organic integration model of GIS, making all stages of the water masses analysis including the capture of the computing grid, data-extraction and discrepancy of the temperature and salinity field, the selection and setting of the model parameters, the computation of model and visualization of the final outcome completed in the same environment. In this way, the efficiency of the application of the model data analysis and decision-making can be greatly enhanced.

1 Model and GIS integration model

GIS and model integration studies have been largely carried out both in China and abroad [10, 11]. It can be achieved through three approaches as follows:

1) Embedded integration model Including two kinds of ways, one is professional software embedded GIS platform, and the other is GIS functions embedded professional model. The former is built on the basis of commercial GIS software packages, taking full advantage of the built-in GIS functions, but currently the model integrated in the GIS software is relatively simple due to the lack of professional participation; the latter's function of handling spatial data analysis is limited, so it is difficult to satisfy the deep-level applications.

2) Loose integration model By using interface procedures as the bridge between the standard GIS software packages and the model, data exchange as the data flow means between the model and the GIS environment can be achieved. This integration is relatively easy to achieve, so it is one of the methods that most users choose, but its shortcomings are the low level of integration, inefficient, and can not guarantee the consistency of user interface and data structure.

3) Tight integration model It Integrates the model and GIS components through the second development language or generic programming language. All the functions and commands are in a unified system, whose stability and implementation of efficiency are both high. The most prominent feature of this integration approach is starting development from the bottom, and all the parts are united together, but it requires a lot of software development work.

2 The water mass analysis model and GIS integration

In this study, we use the Visual Basic 6.0 as the development platform, MapX as the graphics platform, and the professional model is compiled by FORTRAN language. In this way, it will not only take full advantage of GIS software's function on management and analysis of the spatial data, but also make use of the VB and FORTRAN language's programming strongpoints of efficiency and convenience.

2.1 The water mass analysis model

This model plans to adopt Fuzzy Density Clustering method [12] to divide water masses in certain sea

area, and its basic principles are as follows:

Only two indicators are used: temperature and salinity. Here, the space of measuring is the t-s plane, and every grid is regarded as a sample respectively, and the composed matrix is standardized, then:

$$R = \begin{pmatrix} r_{t1} & r_{s1} \\ r_{t2} & r_{s2} \\ | & | \\ r_{tn} & r_{sn} \end{pmatrix} \quad (1)$$

Each of these samples' normalized vectors can be expressed as $r_i = (r_{ti}, r_{si})$.

Because this method needs to compute each point's Fuzzy density, the more data points of temperature and salinity are used, the slower speed of calculation becomes. In order to increase computing speed, and consider the realization of the programming, we make some improvements for this method, and divide the t-s plane into some domains according to appropriate interval. The domains that contain relatively intensive t-s points have grater possibility to become the clustering centre of the water mass. The selected intervals of this model are: temperature 0.5 ° C, salinity 0.25.

For each domain, we gather the t-s points' fuzzy density and the average value of the temperature and salinity, and make the average value of the temperature and salinity as the domain's eigenvalue. The fuzzy density of the *i* domain is defined as:

$$d_i = \frac{1}{n}\sum_{j=1}^{n} v_i\left(\vec{r_j}\right) \quad (2)$$

In equation (2): *n* is the total of samples.

$$v_i\left(\vec{r_j}\right) = \begin{cases} 1 & , \ \vec{r_j} \in s_i \\ 0 & , \ \vec{r_j} \notin s_i \end{cases} \quad (3)$$

s_i is the ith domain in the measuring space.

When the weighted squared Euclidean distance D_{ij} of the mean value between two domains (*i*, *j*) is less than the critical value λ (the critical value of this model λ = 0.6), domains (*i*,*j*) will be amalgamated, and recalculate the fuzzy density and the mean value.

After above merger disposal, we select the maximum fuzzy density domains from all the domains, make their average thermohaline value as the first cohesion center, and is polymerized according to equation (4). According to the pre-set number of water masses c_η, redivide those points that have not yet been polymerized, and also select the maximum fuzzy density domains as the second cohesion center to polymerize. In the same way, we can polymerize n points into c_η groups in the end.

$$d_{ij} \le r^2 * \rho_i \qquad j = 1,2...n \tag{4}$$

In the above expression: d_{ij} is weighted squared Euclidean distance between the *i*th cohesion center and the *j*th point, r is the distinguishing radius:

$$r = \frac{1}{\sqrt{2\pi}} \left(\frac{2}{n * \eta} \right)^{\frac{1}{2}} \tag{5}$$

Given *n*, *r* changes according to the differentiating rate η [0,1].

By adjusting the value η, the value of each division can be calculated at the same time:

$$F = \frac{\frac{1}{m(c_\eta - 1)} \sum_{k=1}^{c_\eta} n_k \left(\vec{r}_k - \vec{r} \right) \left(\vec{r}_k - \vec{r} \right)'}{\frac{1}{m(n - c_\eta)} \sum_{k=1}^{c_\eta} \sum_{r=1}^{n_k} \left(\vec{r}_r - \vec{r}_k \right) \left(\vec{r}_r - \vec{r}_k \right)'} \tag{6}$$

In the equation: *m* is the number of indicators, and *m* is 2 in this model; $\vec{r}$ is *n* test simples' mean vector; n_k is the number of test simples in group *k*; $\vec{r}_k$ is the test sample mean in group *k*; $\vec{r}_r$ is the new serial number of the test sample classified in group *k*. Select the η with the maximum in *F* values as the result of the final division, proceed the result for soft adjustment. When proceeding, take Membership Degree 0.5 as the adjustment standard (>0.5 is the water mass itself).

2.2 GIS and the model integration

MapX Control is a second development control supplied by MapInfo company, whose programmable and mappable component is based on ActiveX (OCX) technology, and has great graphics and attributes functions. To use MapX, MapInfo map documents are necessary. In the absence of MapInfo format charts, so we first use ArcGIS software and bathymetric data to generate JPG format geographical unit layer, then use MapX software to generate Tab, Map documents of every layers, finally generate Geoset documents by loading Tab table, and the Geoset documents are the maps. Enter Visual Basic 6.0 development environment, and embed the controls such as MapX, program — set attributes, transfer methods or respond to incident. Water mass analysis model needs more powerful numerical computing capability, so we use Fortran language for compilation, and add it into the system in the form of dynamic link library, coordinate the operation of GIS components and the model in the way of transferring data from documents and exporting outcome data, integrate GIS and model successfully. Integration system framework is shown in Fig. 1.

2.2.1 Water mass analysis system

Water mass Analysis system is the core of the whole system, including the data-processing model

and the water mass division model. Data-processing model is mainly based on land and sea types of data(obtained from the database or from the layer directly), making Spatial Interpolation for the data extracted; water mass analysis system use the method of Fuzzy Density Clustering that is mentioned above to divide water mass. We must use the FORTRAN language to compile because it needs powerful numerical computing capability in this part, and add it into the system in the form of dynamic link library. Temperature and salinity grounds and the functional interface of water mass analysis system are shown in Fig. 2.

2.2.2 Database system

Database system is mainly responsible for data management, as well as display, inquiry, and modification of the spatial data information. The subsystem is constructed mainly based on the MapX, and its functions include: a) Data management. Model calculation needs a large number of spatial data (such as landform and physiognomy, land - water boundary, attribute data and the data of Temperature and Salinity grounds that the model calculation needs). The system manages this data uniformly. b) Data query. Such as transferring and extracting the water depth or thermohaline data by different geographical location (or time), and drawing all kinds of thematic Raster Map. c) Dynamic updates of data, et al.

We can make sure the plane distribution of the temperature and salinity fields in a certain sea area in virtue of data query. If the distribution of the temperature and salinity fields in different water layer is known, and transfer depth database, the default distribution of the temperature and salinity fields can be queried.

2.2.3 Supplementary information processing subsystem model

Model before processing: the discrete of researched sea (generating square grid automatically) and the capture of the model parameters (via mouse settings or by calling the water layers to obtain automatically).

Model after processing: mainly include the time and space expression of raster map for the result divided as well as some attribute data (such as water mass reunion center), et al. In addition, in order to validate the model to make the calculation result more reasonable, users can amend some certain parameters based on their experience.

2.3 System features

1) Establishing 1：250,000 scale basic geographic information database, contains marine layer, land layer, 5 m, 10 m, 200 m depths layer, et al. Actualize the inquiry and searches of the geographic information for the multi- elements of sea area.

2) The system is developed from the bottom, and various parts integrate together, making all stages of the analysis of the water masses complete in the same environment, improving the efficiencies of the application of the model data analysis and decision-making greatly.

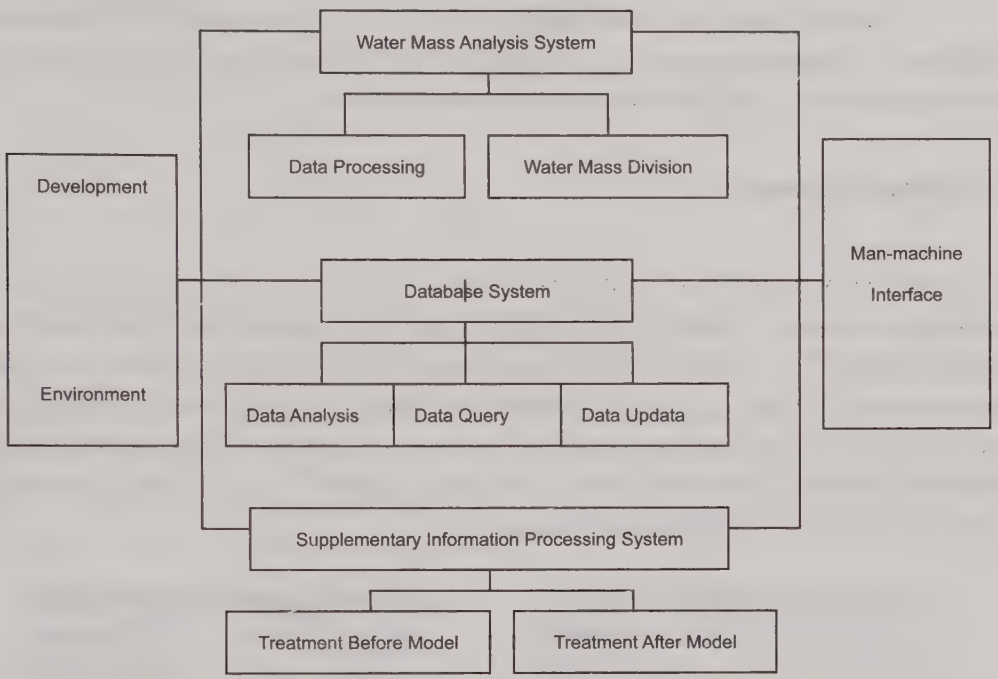

Fig.1 A integration frame

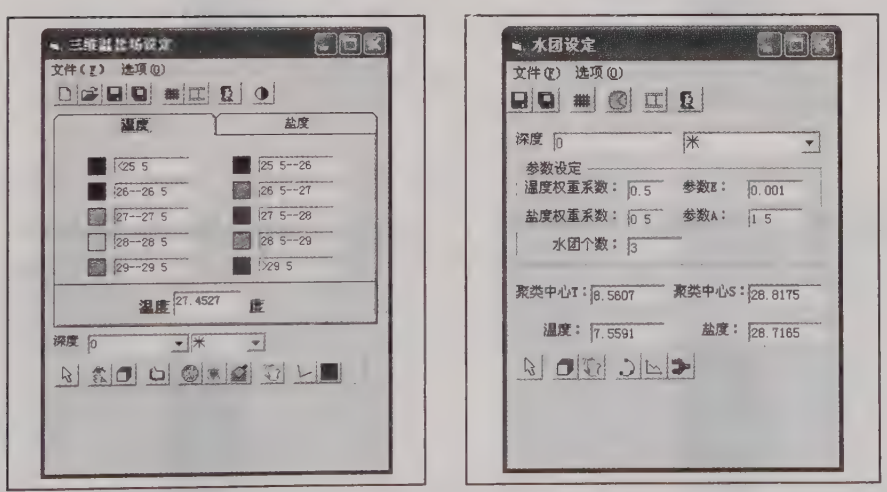

Fig.2 Main windows and function menu of temperature- salinity filed and water mass

3) The application that is developed by the visual development tools has better appearance impression, friendlier user interface. Taking the number of water masses for example, they can be pre-set by the mouse, or can obtain in terms of the sea area layer automatically. It can change the number of water masses to find the best division by displaying the values of the clustering center and grids that are displayed in the results.

4) Achieve the plane and profile distribution of isoline and isosurface of the temperature and salinity fields; actualize the inquiry of the value of all the water masses' cluster centers and each grid point, and in this way we can verify the reliability of water masses' division.

3 Application example

The sea area we study is 28° - 32°N, 122° - 125°E. The data of surface seawater temperature and salinity came from years of observing the average temperature and salinity. Bottom data came from ocean hydrology picture [18]. We should insure the data reliability before classifying water mass by salinity and temperature data. We use this system to draw the distributions of temperature and salinity in winter and summer at Zhoushan sea area and neighborhood sea area. The result show that the distribution of temperature and salinity is accordant with ocean hydrology picture [18], especially the surface data. So we could use those data to classify the water masses.

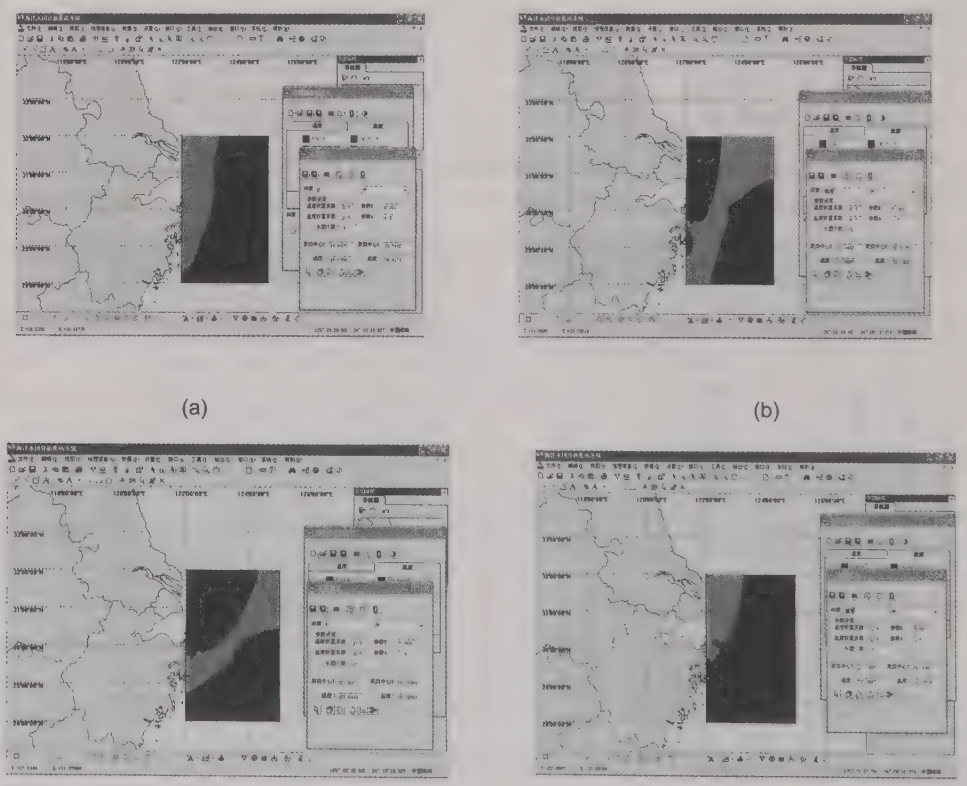

(a) (b)

(c) (d)

Fig.3 Distributions of water masses

(a .surface in winter; b. bottom in winter; c. surface in summer; d. bottom in summer)

Tab. 1 The results of system

The Name of Water Mass	Layer	Winter				Summer			
		T / °C		S		T / °C		S	
		The Central of Clustering	Range	The Central of Clustering	Range	The Central of Clustering	Range	The Central of Clustering	Range
JCW	Surface	8.45	<12.56	28.75	<30.8	26.35	27.0-28.0	29.14	<31.0
	Bottom	9.66	<11.0	29.52	<31.8	22.35	22.9-25.0	28.95	<31.5
MW	Surface	10.96	8.5 - 14.3	32.70	31.0-33.6	27.66	27.3-27.9	32.00	31.0-32.7
	Bottom	12.12	11.5 -14.0	32.82	32.3-33.5	21.69	21.1-22.8	32.75	31.6-33.7
E	Surface	14.58	12.0-17.0	33.83	33.6-34.4	28.31	28.0-29.0	33.32	33.0-33.7
	Bottom	14.33	12.7-15.9	33.61	33.3-34.1				
EU	Surface								
	Bottom					20.63	19.3-22.1	33.90	33.5-34.4

*JCW——Jiangsu-Zhejiang Coastal Water; MW——Mixing Water; E——East China Sea Surface Water; EU—— East China Sea Under Surface Water.

Compare with former analyses result, there are some different in boundary classification in the bottom water masses by this model, in part because of bottom temperature and salinity data is not reliable compared with those of surface. The bottom data are cited from ocean hydrology picture [18], consequently with certain error, and interpolation method also has certain error. But the results show that this model still is a good model that veritably reflect the objective situation.

4 Epilogue

With the high speed development of information technique, close integration of GIS and models is an important tendency. This research under Visual Basic 6.0 environment, empoldered the GIS platform using MapX control; and closely integrated it with water mass analysis model, made up the insufficiency of traditional method that can not satisfy the deep level application, greatly enhanced the model application data analysis and decision-making efficiency, provide a new way for further developments of the specialized model and the enhancement of specialized model practical application potential, and also meets the practical application necessary.

References

[1] Li Fengqi, Su Yuhao, et al. A Test of Cluster Analysis in the Modified Water Mass Analysis in some Shallow Waters [J]. Journal of Oceanography, 1983, 5(6):675 - 686.

[2] Li Fengqi, Su Yuhao, et al. The Application of Fuzzy Mathematical Methods in Water Mass Analysis of the North of the South China Sea [J]. Journal of Oceanography, 1987, 9(6):669 - 680.

[3] Li Fengqi, Su Yuhao, et al. The Fisher Type's Stepwise Discriminatory Prediction of Water Mass Analysis [J]. Journal of ShanDong Ocean University, 1987, (10):17 - 18.

[4] Li Lei, Li Fengqi, et al. Analysis on Water Masses in the South China Sea in Summer and Winter of 1998 [J]. Oceanologia etliminologia sinica, 2002, 33(4):393 - 401.

[5] Zhang QiLong, Wang Fan, et al. Climatological Analysis of Watermasses in ZhouShan Fishing Ground and Adjacent Region [J]. Oceanologia etliminologia sinica, 2004, 35(1):48 - 54.

[6] Zhang Xudong, Zhang Guoyou, et al, Water Mass Analysis of the Source Area of Kuroshio [J]. Marine Science Bulletin, 2004, 25(1):15 - 21.

[7] Hong Bo, Yang Hong. The Application of Fisher's Stepwise Discriminant Analysis to the Water Masses in the East China Sea [J].Ocean Fisheries, 2005, 27(2):143 - 149.

[8] Miao Zhenqing, Yan Shiqiang. Statistical Research About Hydrologic Character of Fishing Ground of Pneumatophorus Japonicus and Decapterus Maruadsi in the North of East China Sea [J]. Oceanologia etliminologia sinica,2003，34(4):397 - 406.

[9] Jia Haifeng, Chen Shengtong, et al. Integration of GIS with Surface Water Quality Model WASP5. Journal of Tsinghua University (Sci&Tech), 2001, 41(8):125 - 128.

[10]Wei Jiahua, Li Cijun, et al. Study on the Integration of Groundwater Numeric Model and Components GIS, Journal of JinLin University, 2003, 33(4):534 - 538.

[11] Liu Zhiyu. ArcTOP: A Distributed Hydrological Modeling System of Tight Coupling TOPKAPI with GIS [J]. HYDROLOGY, 2005, 25(4):18 - 22.

[12] Yin Hailong, Xu Zuxin. Study on the Realization of Visual Water Environmental Models for the HuangPu River [J]. Environment Pollution and Control, 2005, 27(1):5 - 7.

[13] Shamsi U M. Storm-Water Management Implementation through Modeling and GIS [J].Journal of Water Resources Planning and Management, 1996, 122:114 - 127.

[14] Sui D Z, Maggio R C. Integrating GIS with Hydrological Modeling：Practices，Problems，and Prospects [J]. Computer，Environment And Urban System,1999，23:33 - 51.

[15] Fan Beilei, Wu Ping, et al. Integration System of Agriculture Supervision Based on Component GIS [J]. Micro-Computer Information, 2005, 22:255 - 257.

[16] Zhu Can, Li Lan, et al. Design and Application of Water Quality Pre-warning and Forecast System Based on GIS in Xi River [J].China's Rural Water Conservancy and Hydropower,2006,10:9 - 11.

[17] Li Fengqi, Su YuHao, et al. Water Mass Analysis [M]. QingDao: Ocean University Publishing House, 2000.

[18] Ocean Atlas Editorial Committee: Ocean Atlas of Bohai Yellow sea and East China Sea — Hydrology [M]. BeiJing: Ocean Publishing House,1992.

基于 GIS 水团分析集成系统的开发及其应用

张月霞[1]，苗振清[2]，严世强[3]

（1. 国家海洋局第二海洋研究所，浙江 杭州 310012；2.浙江海洋学院，浙江 舟山 316004；
3. School of Engineering and Mathematical Science, City University, London）

摘 要：水团的识别与划分一直是物理海洋学的重要研究内容。本研究采用模糊密度聚类方法划分水团，并利用 Fortran 语言编制了该模型；同时，在 Visual Basic 6.0 环境下，利用 MapX 控件进行了 GIS 平台开发；并将两者紧密集成，使得水团分析的所有阶段，包括计算网格的获取、温盐场数据的提取和插值、模型的参数选择和设置、模型的计算以及最终结果的可视化等都在同一环境下完成，大大提高模型应用的数据分析和决策的效率。将该系统应用于舟山渔场及其邻近海域，所得结果比较理想。

关键词：水团；GIS；模型集成；舟山渔场

Numerical Simulation of the Influence of Mean Sea Level Rise on Typhoon Storm Surge in the East China Sea

GAO Zhigang[1], HAN Shuzong[1], LIU Kexiu[2], ZHENG Yunxia[1], YU Huaming[1]

1. *Ocean University of China, Qingdao* 266100, *Shandong, China;*

2. *National Marine Data & Information Service, Tianjin* 300171, *China*

Abstract: In this paper, ECOMSED (Estuarine Coastal Ocean Model with sediment transport) model is employed to simulate storm surge process caused by typhoon passing across East China Sea in nearly years. Capability of ECOMSED to simulate storm surge is validated by comparing model result with observed data. Sensitivity experiments are designed to study the influence of sea level rise on typhoon storm surge. Numerical experiment shows that influence of mean sea level rise on typhoon storm surge is non-uniform spatially and changes as typhoon process differs. Maybe fixed boundary method would weaken the influence of mean sea level rise on storm surge, and free boundary method is suggested for the succeeding study.

Keywords: Storm surge simulation; ECOMSED model; East China Sea; sea level rise

1 Introduction

Storm surge is a phenomenon of sea level rise abnormally caused by strong wind or abrupt change of atmospheric pressure. Storm surge leads to seawater intrusion making much economic loss, so it's essential to focus on the phenomenon of storm surge. W. Hansen is the first one to use numerical method to simulate storm surge of the North Sea in 1956. Jelesnianski et al. developed SLOSH model to predict storm surge process [1]. Yu et al. simulated storm surge caused by typhoon Polly in spherical coordinate system [2]. Nested grid system is also used to simulate storm surge [3], [4]. Wang considered that the storm surge is a process of forced oscillation so satisfactory results can be obtained only when the calculation field covers the whole region [5]. Jiang and Sun simulated the influence of changing topography to storm surge in Qingdao [3]. Thus a higher resolution and a considerable larger zone is better for the storm surge simulation.

Sea level rise is a focused problem especially in the coastal China Sea where speed of sea level rise is larger than that of global mean value. It's reported that storm surge would be more serious as mean sea level rises according to statistical data. No numerical simulation experiment has been taken to study the effect of sea level rise on storm surge in coastal China Sea. So ECOMSED model whose validation has been checked is adopted to simulate typical typhoon storm surge in the East China Sea.

Received on February 1, 2008

2 Model introduction

2.1 Hydrological model

The development of ECOMSED has its origin in the mid 1980's with the creation of the Princeton Ocean Model [6]. Primary characteristics of the hydro-dynamical model are: a) Orthogonal curvilinear grid in the horizontal direction and sigma level system in the vertical direction; b) An imbedded second moment turbulence closure sub-model to provide vertical mixing coefficients; c) The horizontal time differencing is explicit whereas the vertical differencing is implicit; d) A free surface and a split time step; e) Complete thermodynamics have been implemented. Governing equations are detailed as follows.

Continuity equation is:

$$\nabla \cdot \bar{V} + \frac{\partial W}{\partial Z} = 0 \tag{1}$$

Reynolds momentum equations are:

$$\frac{\partial U}{\partial t} + \bar{V} \cdot \nabla U + W \frac{\partial U}{\partial z} - fV = -\frac{1}{\rho_\circ}\frac{\partial P}{\partial x} + \frac{\partial}{\partial z}\left(K_M \frac{\partial U}{\partial z}\right) + F_X \tag{2}$$

$$\frac{\partial V}{\partial t} + \bar{V} \cdot \nabla V + W \frac{\partial V}{\partial z} + fU = -\frac{1}{\rho_\circ}\frac{\partial P}{\partial y} + \frac{\partial}{\partial z}\left(K_M \frac{\partial V}{\partial z}\right) + F_Y \tag{3}$$

$$\rho g = -\frac{\partial P}{\partial z} \tag{4}$$

where $\rho_\circ$ is reference density, ρ is in-situ density, P pressure, K_M vertical eddy diffusivity of turbulent momentum mixing, and f is Coriolis parameter.

The pressure at depth Z can be obtained by:

$$P(x,y,z,t) = P_{atm} + g\rho_\circ \eta + g\int_z^0 \rho(x,y,z',t)dz' \tag{5}$$

All of the motions induced by small-scale processes can be induced by parameterized terms F_X, F_Y and $F_{\theta,S}$ which are written as:

$$\begin{aligned} F_X &= \frac{\partial}{\partial x}\left[2A_M \frac{\partial U}{\partial x}\right] + \frac{\partial}{\partial y}\left[A_M\left(\frac{\partial U}{\partial y} + \frac{\partial V}{\partial x}\right)\right] \\ F_Y &= \frac{\partial}{\partial y}\left[2A_M \frac{\partial V}{\partial y}\right] + \frac{\partial}{\partial x}\left[A_M\left(\frac{\partial U}{\partial y} + \frac{\partial V}{\partial x}\right)\right] \\ F_{\theta,S} &= \frac{\partial}{\partial x}\left[2A_H \frac{\partial(\theta,S)}{\partial x}\right] + \frac{\partial}{\partial y}\left[A_H \frac{\partial(\theta,S)}{\partial y}\right] \end{aligned} \tag{6}$$

The parameterization of turbulence in the module described here is based on the work of Mellor and Yamada [7]. Three types of open boundary conditions are supplied in ECOMSED, including Clamped Boundary Condition, Reid and Bodine Boundary Condition and Optimized Clamped Boundary Condition.

2.2 Jelesnianski wind field model

Surface wind and atmospheric pressure of typhoon is supplied by Jelesnianski circle wind field model, according to the central pressure and track of the typhoon [9].

$$\vec{W} = \begin{cases} \frac{r}{R+r}(V_{ox}\vec{i}+V_{oy}\vec{j})+W_R(\frac{r}{R})^{3/2}\cdot\frac{1}{r}(A\vec{i}+B\vec{j}), (r \le R) \\ \frac{R}{R+r}(V_{ox}\vec{i}+V_{oy}\vec{j})+W_R(\frac{R}{r})^{1/2}\cdot\frac{1}{r}(A\vec{i}+B\vec{j}), (r > R) \end{cases}$$

$$P_a = \begin{cases} P_0+\frac{1}{4}(P_\infty - P_0)(\frac{r}{R})^3, (r \le R) \\ P_\infty - \frac{3}{4}(P_\infty - P_0)(\frac{R}{r}), (r > R) \end{cases}$$

Where, $A=-[(x-x_c)\sin\theta+(y-y_c)\cos\theta]$; $B=[(x-x_c)\cos\theta-(y-y_c)\sin\theta]$; while (x, y)、(x_c, y_c) are the location of objective grid and the center of typhoon specifically. θ is influx angle (set as 20° in calculation); (V_{ox}, V_{oy}) are the moving speeds of typhoon center in x, y direction specifically; W_R is maximum wind speed of typhoon; r is distance between objective grid and center of typhoon; R is radius of maximum wind speed; P_0 is air pressure of typhoon center; P_∞ is basical air pressure; P_a is air pressure over sea surface. These parameters are acquired from Tropical Cyclone Annual.

3 Setting of the model

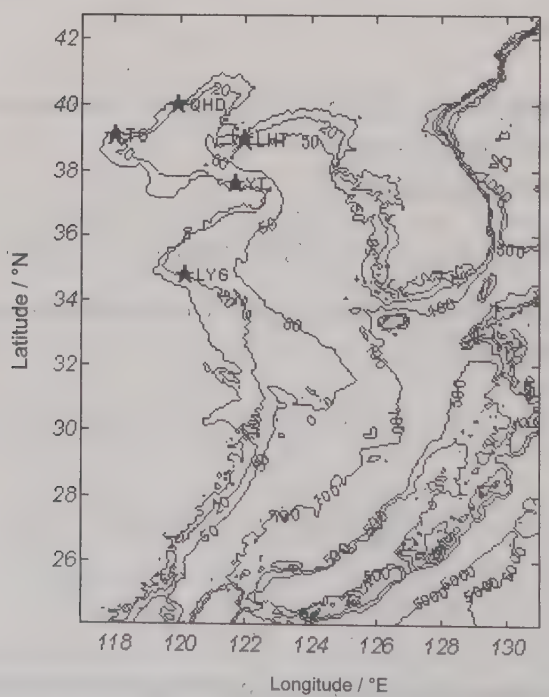

Fig. 3-1 Topographic map of the East China Sea (Isobaths are in meters)

Five tidal stations: LHT(LaoHuTan), QHD(QinHuangDao), TG(TangGu), YT(YanTai), LYG(LianYunGang)

Computing zone is 24°N - 43°N, 117°E - 131°E, as Fig. 3-1 shows. Horizontal grids are 169×229 (W - E×S - N), with the resolution of 5′ × 5′. The simulation begins from a state of rest ($\eta = u = v = 0$).

Three typhoon processes are selected here, and they are typhoon Prapiroon with No. 0012, typhoon Fengshen with No. 0209, typhoon Maemi with No. 0314. The track of typhoon is shown in Fig. 3-2.

Typhoon Prapiroon came into being in the east of Taiwan Island on Aug. 27, 2000, and it passed through the ZhouShan archipelago reaching to the mouth of the Changjiang River on Aug. 30, 2000. More than 20 tidal stations' tidal level were higher than the local guard-level in Jiangsu, Shanghai and Zhejiang Province. Then it moved to the northeast direction through the Yellow Sea and landed on the Korea peninsula in the end.

Typhoon Fengshen is generated in central Pacific Ocean on Jul. 14, 2002. It moved northwest with moving speed accelerating then it growth to be strong typhoon, maximum wind speed reaching 55 m/s, and minimum central air pressure is 925 hPa. After moving through the Northwest Pacific Ocean it landed in Jiaonan, Shandong Province. Then it changed the original path moving to the north direction, reaching Bohai Sea during which it became weaker and vanished tail end.

On Sep. 4, 2003, a tropical low pressure is formed over sea surface, southeast of Guam then it moved northeast and grew stronger and stronger. It became a typhoon named Maemi on Sep. 9, 2003, with its maximum wind speed up to 60 m/s. Then it turned to northeast, moved through and landed in Busan, Korea. Then it weakened to be a strong tropical storm and vanished in Sea of Japan in the end.

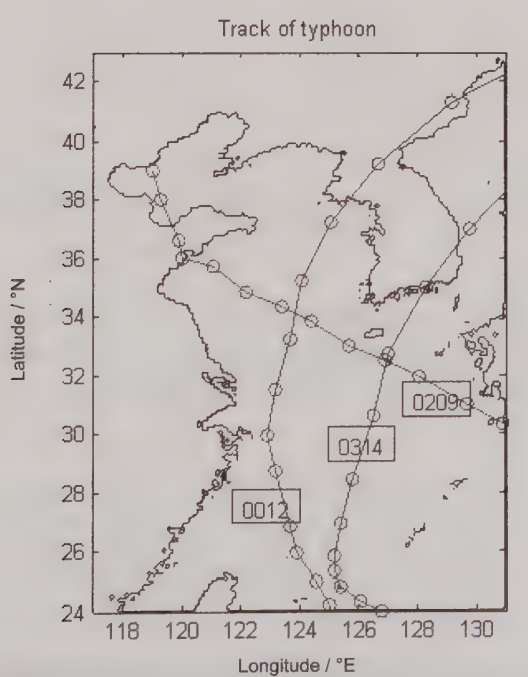

Fig. 3-2 Track of typhoon (No. 0012 Prapiroon, No. 0209 Fengshen, No. 0314 Maemi)

4 Result analysis

Model result is compared with observed data of five coastal tidal stations during the period of typhoon. Observed surge elevation is considered to be residual elevation calculated by subtracting predicted tidal elevation from observed water level. Location of five stations is shown in Tab. 4-1 and Fig. 3-1.

Tab. 4-1 Location of tidal stations

Station Name	Location	
	Latitude	Longitude
LHT(LaoHuTan)	38°52.0'N	121°40.9'E
LYG(LianYunGang)	34°44.5'N	119°27.3'E
QHD(QinHuangdao)	39°55.0'N	119°37.0'E
TG(TangGu)	39°0 0'N	117°43.0'E
YT(YanTai)	37°32 6'N	121°23 6'E

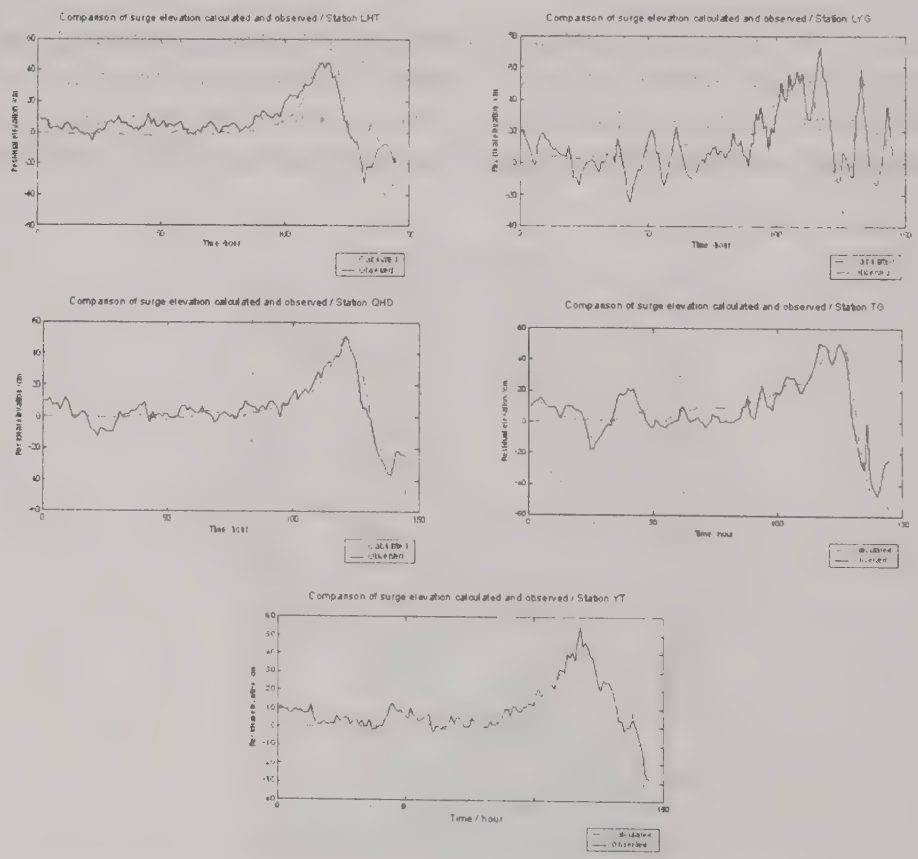
Comparison of surge elevation calculated and observed / Station LHT
Comparison of surge elevation calculated and observed / Station LYG
Comparison of surge elevation calculated and observed / Station QHD
Comparison of surge elevation calculated and observed / Station TG
Comparison of surge elevation calculated and observed / Station YT
Time / hour

Fig. 4-1 Comparison of surge elevation calculated and observed during the period of typhoon Prapiroon

(from 0:00, Aug. 26, 2000 to 23:00, Sep. 1, 2000)

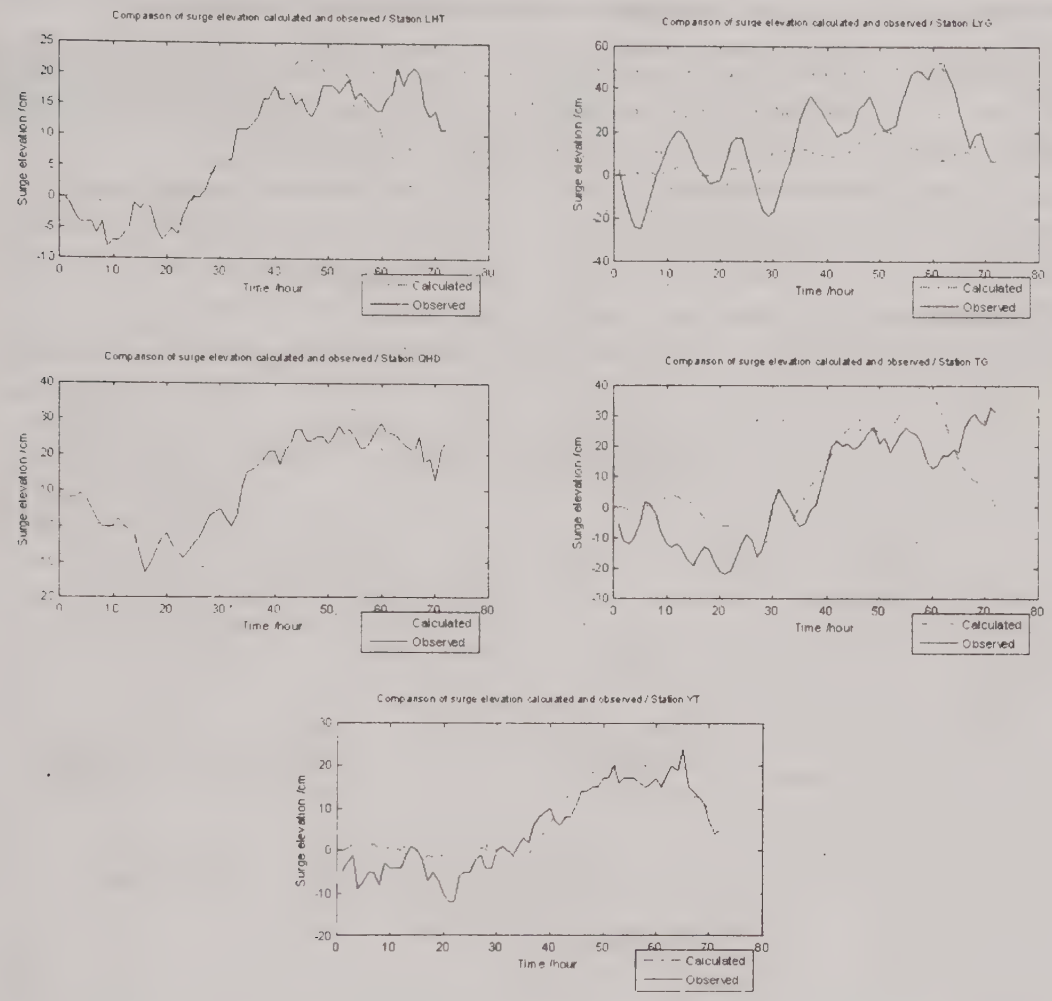

Fig. 4-2 Comparison of surge elevation calculated and observed during the period of typhoon Fengshen

(from 21:00, Jul. 25, 2002 to 20:00, Jul. 28, 2002)

Fig. 4-1 shows that simulation of storm surge caused by typhoon Prapiroon is of well accordance with observed data. The extreme surge elevation and its occurring time are all consistent with observed data. The maximum derivation appears at the LYG station of which calculated extreme surge elevation is 18 cm less than that of observed.

Simulated result of typhoon Fengshen compared with observed data is shown as Fig. 4-2. The surge process could be considered to be two parts. The former process is water decreasing, and the latter process is caused by the effect of typhoon reaching the peak water increase value. Result of the LYG station is awful, and calculated pattern of the surge process differs much with observed data.

Fig. 4-3 shows comparison of result of typhoon Maemi. We can see that the surge process is mainly a water increase process. Calculated result of five stations shows the basic consistency with observed

data in pattern. Minimum elevation value and occurring time differ little from observed data.

In general, the simulated result is acceptable, that's to say, the validation of ECOMSED to simulate storm surge in the East China Sea is confirmed. Maybe model result could be advanced with more accurate atmospheric conditions. Then we can use this model for further study.

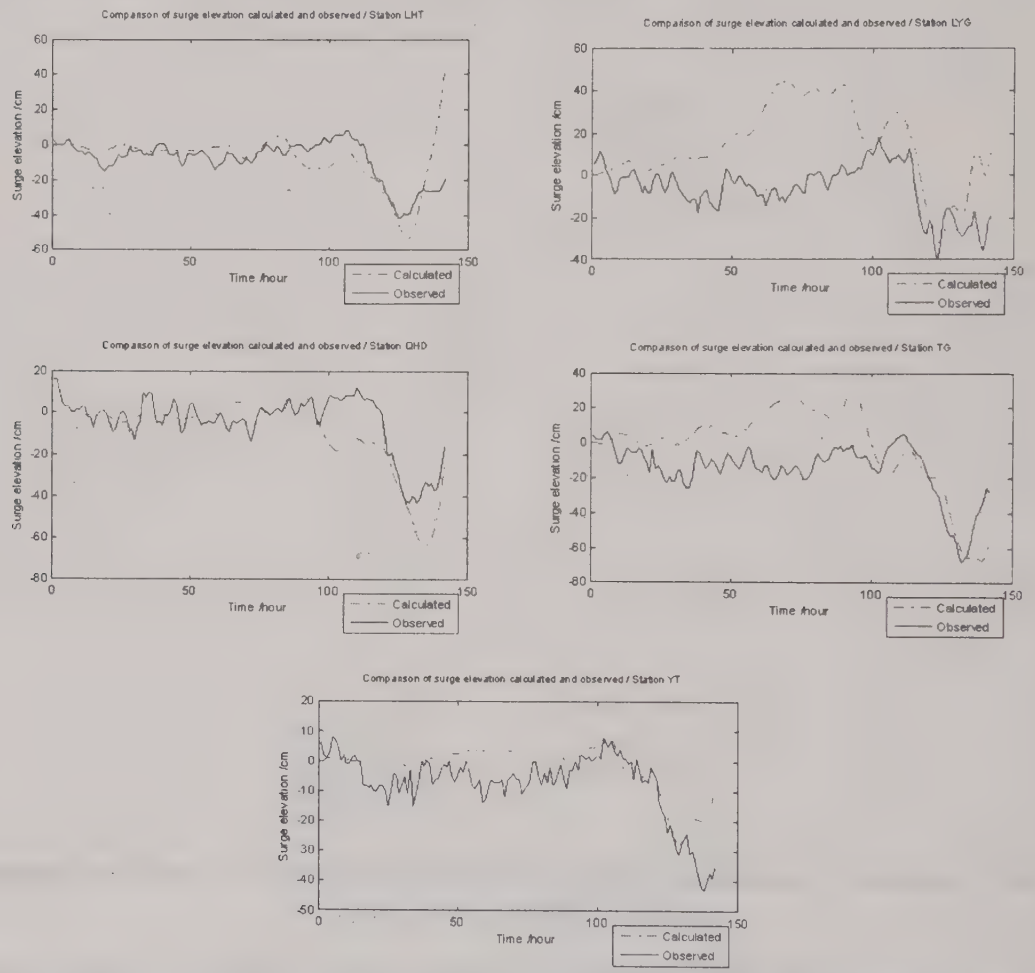
Comparison of surge elevation calculated and observed / Station LHT
Comparison of surge elevation calculated and observed / Station LYG
Comparison of surge elevation calculated and observed / Station QHD
Comparison of surge elevation calculated and observed / Station TG
Comparison of surge elevation calculated and observed / Station YT
Surge elevation /cm
Time /hour
Calculated
Observed

Fig. 4-3 Comparison of surge elevation calculated and observed during the period of typhoon

(from 1:00, Sep. 8, 2003 to 2:00, Sep. 14, 2003)

5 Sensitivity experiments

The Third Assessment Report of IPCC [10] indicates that during the last centenary, the global air temperature and sea-level have rised 0.6 °C ± 0.2 °C and 10 m - 20 cm respectively; and the global temperature and global mean sea level are expected to rise 1.4 °C - 5.8 °C and 9 - 88 cm respectively by 2100. Then we choose a mean value of 50 cm to simulate the mean sea level of 2100. IPCC's Fourth Assessment Report [11] indicates that the corresponding future temperatures in Greenland (1.9°C to 4.6 °C

global) are comparable to those inferred for the last interglacial period 125,000 years ago, when palaeoclimatic information suggests the reduction of polar land ice extent and 4 m to 6 m of sea level rise. Thus we choose 5 m higher than normal mean sea level as the most terrible case. In addition, 2 m higher is considered to be the middle status of mean sea level rise to extreme case.

Three real typhoon processes (Prapiroon, Fengshen and Maemi) are chosen to test sensitivity of surge elevation to track of typhoon as mean sea level rise. Two ideal experiments considering stable wind field are also made to check sensitivity of surge elevation to intensity of wind as mean sea level rise. Ideal experiment I (IE I for short)is a process considering wind with fixed speed of 10 m/s from southeast which is helpful for water increase of the five stations, while ideal experiment II (IE II for short) is of 30 m/s with the same direction as IE I.

The extreme surge elevation is the most focused factor, so we layout typical result as Fig. 5-1 - 5-5 and Tab. 5-1 showed.

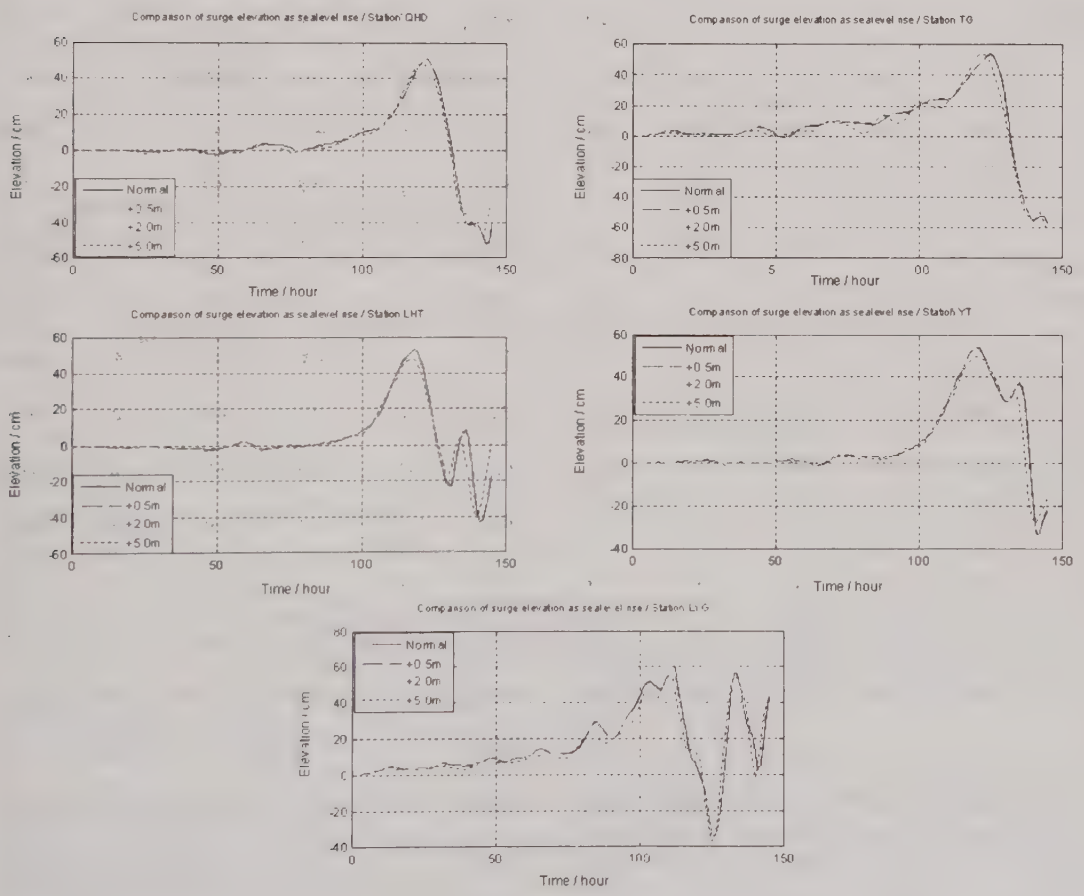
Comparison of surge elevation as sealevel rise / Station QHD
Comparison of surge elevation as sealevel rise / Station TG
Comparison of surge elevation as sealevel rise / Station LHT
Comparison of surge elevation as sealevel rise / Station YT
Comparison of surge elevation as sealevel rise / Station LYG
Elevation / cm
Time / hour
Normal
+0.5m
+2.0m
+5.0m

Fig. 5-1 Comparison of surge elevation change when MSL rising for typhoon Prapiroon

Tab. 5-1 Extreme surge elevation (ESE) change as MSL rising

Typhoon	Station	Normal	MSL+0.5m			MSL+2.0m			MSL+5.0m		
		ESE / cm	ESE / cm	ΔESE / cm	ΔESE / %	ESE / cm	ΔESE / cm	ΔESE / %	ESE / cm	ΔESE / cm	ΔESE / %
	QHD	51	51	0	0	50	-1	-2.0	49	-2	-3.9
	TG	54	55	1	1.9	56	2	3.7	58	4	7.4
Prapiroon	LHT	54	54	0	0	52	-2	-3.7	49	-5	-9.3
	YT	54	54	0	0	52	-2	-3.7	50	-4	-7.4
	LYG	61	61	0	0	60	-1	-1.6	55	-6	-9.8
	QHD	66	65	-1	-1.5	64	-2	-3.0	61	-5	-7.6
	TG	79	80	1	1.3	81	2	2.5	82	3	3.8
Fengshen	LHT	47	46	-1	-2.1	45	-2	-4.3	43	-4	-8.5
	YT	42	42	0	0	42	0	0	43	1	2.4
	LYG	42	43	1	2.4	44	2	4.8	48	6	14.3
	QHD	-63	-64	-1	-1.6	-64	-1	-1.6	-67	-4	-6.3
	TG	-67	-67	0	0	-68	-1	-1.5	-72	-5	-7.5
Maemi	LHT	-53	-53	0	0	-53	0	0	-51	2	3.8
	YT	-28	-28	0	0	-27	1	3.6	-24	4	14.3
	LYG	-32	-32	0	0	-32	0	0	-30	2	6.3
	QHD	54	54	0	0	52	-2	-3.7	50	-4	-7.4
	TG	63	63	0	0	62	-1	-1.6	59	-4	-6.3
IE I	LHT	32	31	-1	-0.8	31	-1	-3.1	30	-2	-6.3
	YT	28	28	0	0	28	0	0	29	1	3.6
	LYG	34	34	0	0	33	-1	-2.9	31	-3	-8.8
	QHD	611	610	-2	-0.3	602	-9	-1.5	587	-24	-3.9
	TG	719	717	-2	-0.3	709	-10	-1.4	686	-33	-4.6
IE II	LHT	390	389	-1	-0.2	385	-5	-1.3	379	-11	-2.8
	YT	332	332	0	0	335	3	0.9	344	12	3.6
	LYG	329	328	-1	-0.1	329	0	0	332	3	0.9

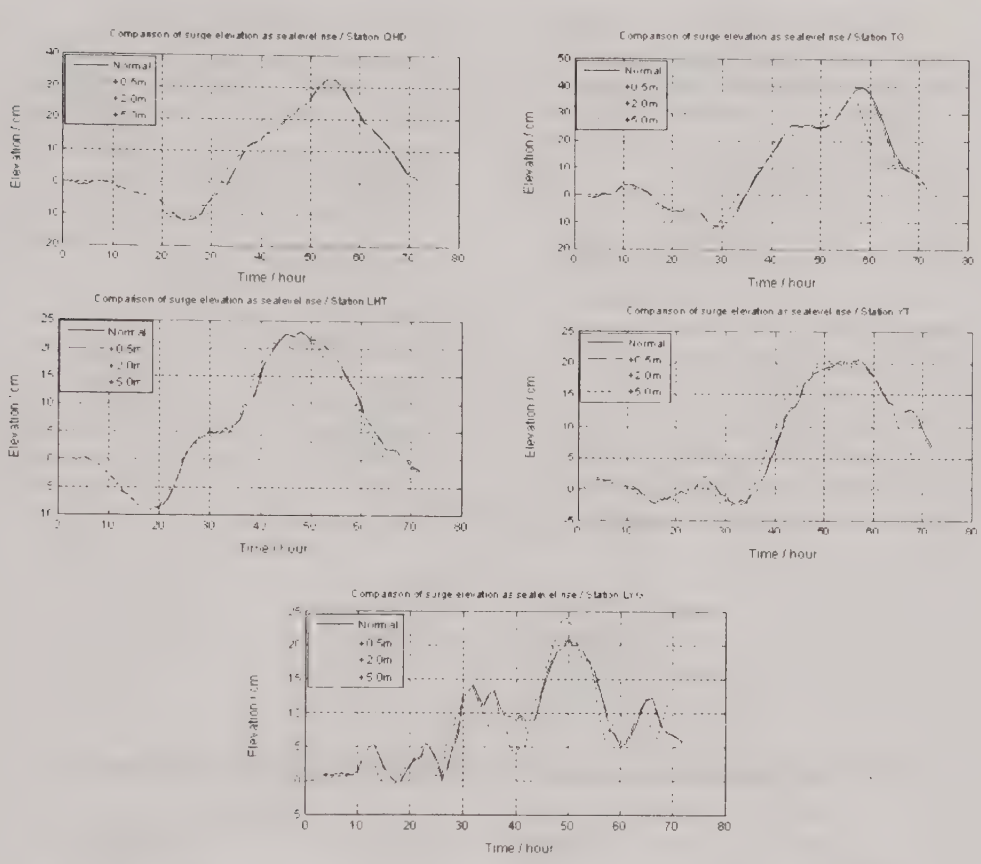
Comparison of surge elevation as sealevel rise / Station QHD
Comparison of surge elevation as sealevel rise / Station TG
Comparison of surge elevation as sealevel rise / Station LHT
Comparison of surge elevation as sealevel rise / Station YT
Comparison of surge elevation as sealevel rise / Station LYG
Normal
+0.5m
+2.0m
+5.0m
Elevation / cm
Time / hour

Fig. 5-2 Comparison of surge elevation change when MSL rising for typhoon Fengshen

We can see from the modeling result that extreme surge elevation change is non-uniform spatially. For typhoon Prapiroon, extreme high surge elevation of all five stations decreases when mean sea level rises. For typhoon Fengshen, extreme high surge elevation of QHD and LHT decreases and other stations present the inverse trends. For typhoon Maemi, the extreme low surge elevation decreases in station QHD and TG, while those in other stations increase.

Even for the same station, the variation of extreme surge elevation is different as storm surge differs. Take station LYG for example, its extreme high surge elevation decreases as mean sea level rise for typhoon Prapiroon; Otherwise it takes on an opposite trend for typhoon Fengshen in which its extreme high surge elevation increases as mean sea level rises.

Result of IE I and IE II shows that relative variance of extreme surge elevation is not sensitive to the wind speed as mean sea level rise. In the case of weaker wind of IE I, when mean sea level rise 5.0 m, the extreme high elevation of QHD is of 4 cm lower than that of normal case, which accounts for about 7.4 % of extreme surge elevation of normal case. When wind speed increases to 30 m/s in IE II, as mean sea level rises 5.0 m, the extreme high elevation of QHD decreases 24 cm from that of normal case which accounts for about 3.9 % of normal case.

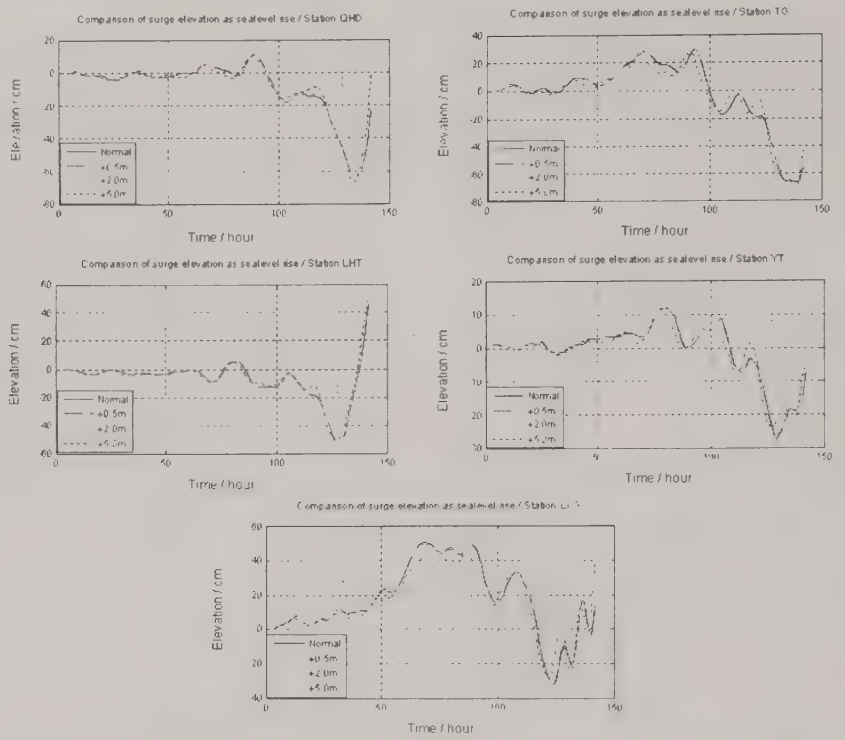
Comparison of surge elevation as sealevel rise / Station QHD
Comparison of surge elevation as sealevel rise / Station TG
Comparison of surge elevation as sealevel rise / Station LHT
Comparison of surge elevation as sealevel rise / Station YT
Elevation / cm
Time / hour
Normal
+0.5m
+2.0m
+5.0m

Fig. 5-3 Comparison of surge elevation change when MSL rising for typhoon Maemi

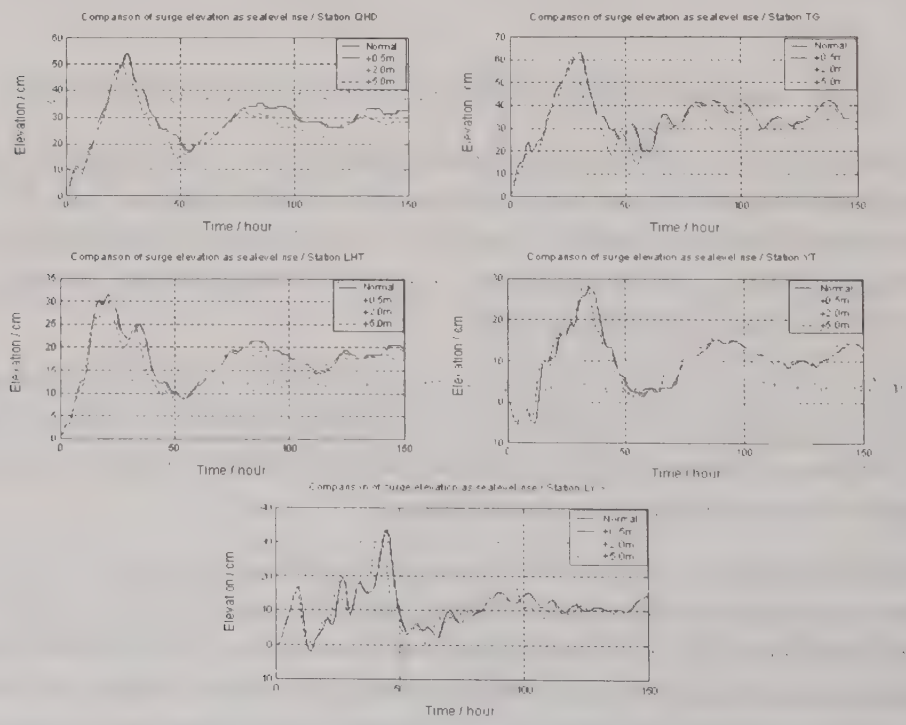
Comparison of surge elevation as sealevel rise / Station QHD
Comparison of surge elevation as sealevel rise / Station TG
Comparison of surge elevation as sealevel rise / Station LHT
Comparison of surge elevation as sealevel rise / Station YT
Elevation / cm
Time / hour
Normal
+0.5m
+2.0m
+5.0m

Fig. 5-4 Comparison of surge elevation change when MSL rising for ideal experiment I

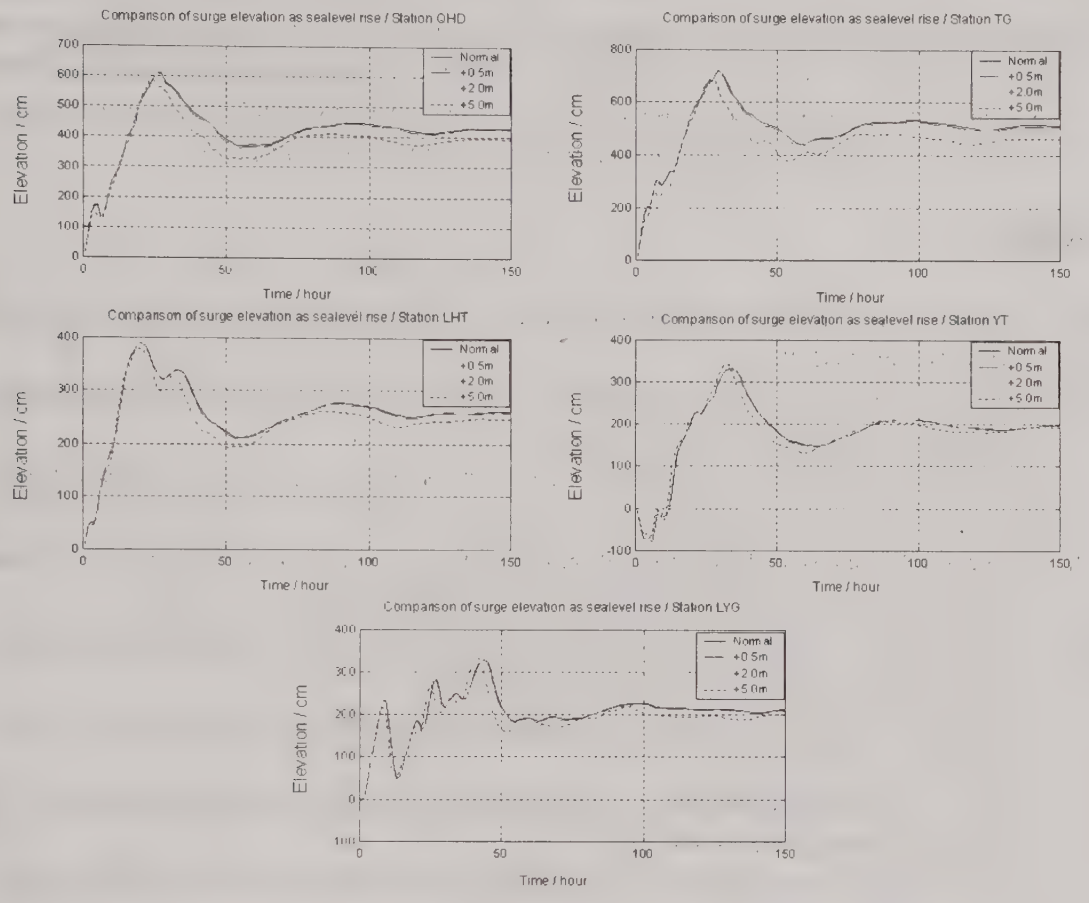
Comparison of surge elevation as sealevel rise / Station QHD
Comparison of surge elevation as sealevel rise / Station TG
Comparison of surge elevation as sealevel rise / Station LHT
Comparison of surge elevation as sealevel rise / Station YT
Comparison of surge elevation as sealevel rise / Station LYG
Normal
+0.5m
+2.0m
+5.0m
Elevation / cm
Time / hour

Fig. 5-5 Comparison of surge elevation change when MSL rising for ideal experiment II

In a word, simulated result shows that extreme surge elevation is not too sensitive to the mean sea level rise. When mean sea level rise 0.5 m, the variation of extreme surge elevation changes little for all stations. Even for 5 m rising extreme surge elevation just varies less than 10 % for most stations. We can not get the conclusion that sea level rise makes little influence on storm surge. Maybe our model not taking the coast changing into consideration makes it happen. Accumulation in coastal areas is an important process for storm surge propagation. Coast is also changed as mean sea level rises, so if we fixed the boundary in numerical simulation, the influence of mean sea level rise may be weakened.

6 Conclusion

Three typical typhoon storm surge processes are simulated using ECOMSED model. The capability of ECOMSED to simulate storm surge in the East China Sea is assured by comparison of model result and observed data in five coastal stations. Sensitive experiment shows that influence of mean sea level rise on typhoon storm surge is non-uniform spatially, for the same typhoon process extreme surge

elevation increases in some stations and for the inverse in other stations; Just for the same station, different typhoon process makes inconsistent influence. In a word, extreme surge elevation is not too sensitive to mean sea level rise using fixed boundary method which may weaken the accumulating effect of storm surge in coastal area. Thus we suggest that it's necessary to use a free boundary method to simulate the influence of mean sea level rise on storm surge for the succeeding studies.

Reference

[1] Jelesnianski, Jye Chen, Wilson A Shffer. SLOSH: Sea, Lake and Overland Surges from Hurricanes [R]. NOAA Technical Report, 1992, 48(71).

[2] Yu Fujiang, Wang X N, et al. The numerical simulation of storm surge in Bohai Sea caused by tropical storm POLLY [M]. Acta Oceanologica Sinica, 2000, 17(4): 9 - 15.

[3] Jiang Wensheng, Sun W X. Simulation of the influence of the changing topography to storm surge in Qingdao. Marine Forecasts, 2002, 19(1):97 - 104.

[4] Yu Fujiang, Zhang Z H. Implementation and application of a nested numerical typhoon storm surge forecast model in the East China Sea. Acta Oceanologica Sinica, 2002, 24(4): 23 - 33.

[5] Wang Xiuqin, Qian C C, Wang W. The Influence of Selected Calculation Field on the Simulation of Storm Surges. Periodical of Ocean University of China, 2001, 31 (3): 319 - 324.

[6] Blumberg A F, G L Mello. A Description of a Three-Dimensional Coastal Ocean Circulation Model [J]. American Geophys. Union, 1987, Ed.: 1 - 16.

[7] Mellor G L, T Yamada. Development of a Turbulence Closure Model for Geophysical Fluid Problems, Rev. Geophys. Space Phys., 1982, 20: 851 - 875.

[8] Editorial board for marine atlas, Marine Atlas of Bohai Sea Yellow Sea East China Sea (Hydrology) [M]. Beijing: China Ocean Press. 1992, 429 - 432.

[9] Jelesnianski C P. A numerical computation of storm tides induced by a tropical storm impinging on a continental shelf [J]. Mon. Wea. Rev., 1965, 93 (16): 343 - 358.

[10] Church J A, J M Gregory, P Huybrechts, et al .Changes in sea level. In Climate Change 2001: the Scientific Basis, Contribution of Working Group I to the Third Assessment Report of the Intergovernmental Panel on Climate Change. Houghton J T, Ding Y, Griggs D J. et al. Cambridge, Cambridge Univ. Press, 2001, 639 - 693.

[11] Jansen E J, Overpeck, K R Briffa, et al. Palaeoclimate. In: Climate Change 2007: The Physical Science Basis. Contribution of Working Group I to the Fourth Assessment Report of the Intergovernmental Panel on Climate Change [Solomon S, D Qin, M Manning, et al.] Cambridge University Press, Cambridge, United Kingdom and New York, NY, USA, 2007, 410 - 417.

平均海平面上升对东中国海台风风暴潮影响的数值模拟

高志刚[1]，韩树宗[1]，刘克修[2]，郑运霞[1]，于华明[1]

（1. 中国海洋大学，山东 青岛，266100；2. 国家海洋信息中心，天津 300171）

摘 要：本文采用 ECOMSED 模式模拟了影响东中国海的 3 次台风过程，经与实测资料对比验证了模型的可靠性。在此基础上设计了敏感性试验以考察海平面上升对风暴潮造成的影响。结果表明，海平面上升对风暴潮的影响在空间分布上不是一致的，且因具体台风过程而异。整体而言，海平面上升对风暴潮造成的影响有限。海平面上升 0.5 m，大部分站位风暴增水极值基本不变，即使海平面上升 5 m大部分站位的风暴增水极值相对改变量都小于 10 %。

关键词：风暴潮数值模拟；平均海平面上升；ECOMSED 模型；东中国海

Antarctic Psychrophile Bacteria Screening for Oil Degradation and Their Degrading Characteristics

ZHENG Zhou[1,2], JIN Qing[3], MIAO Jinlai[1,2], LIU Fangming[1,2]

1. *First Institute of Oceanography, SOA, Qingdao* 266061, *Shandong, China;*

2. *Key Lab of Marine Bioactive Substances, SOA, Qingdao* 266061, *Shandong, China;*

3. *Qingdao university of science and technology, Qingdao* 266042, *Shandong, China*

Abstract: Two hydrocarbon degrading bacteria NJ276 and NJ341 were screened from 385 Antarctic marine bacteria and their degrading characteristics were studied. Diesel oil as sole carbon source was used in this study. The results showed that the oil degradation rates of Antarctic psychrophile bacteria NJ276 and NJ341 were 23.47 % and 32.15 %, respectively, after 20 days culturation at 5 °C, and the rates were 43.95 % and 62.47 % respectively after 20 days culturation at 15 °C. The oil degradation abilities were enhanced remarkably with the increasing culture temperature. GC - MSs indicated the residual oil contained C_{15} - C_{21} 7 alkyls after degradation by NJ276, and C_{16}, C_{17} and C_{18} 3 alkyls after degradation by NJ341. The 16S rDNA gene sequences homology and phylogenetic analysis of the two Antarctic psychrophile bacteria showed that NJ276 belonged to the described genus Pseudoalteromonas and NJ341 belonged to the genus Colwellia.

Keyword: Antarctic psychrophile bacteria; Hydrocarbon; Degradation

Instruction

Oil pollutions in the sea have been increasing serious and popular. Biodegradation holds the special superiority in oil pollution control, so cleaning up the oil pollution of the sea by marine microorganisms biodegradation has roused people's great attention. A lot of scholars have carried out many researches on the oil biodegradation using marine microorganisms, but most people focus on the oil biodegradation using mesophilic marine microorganisms [1, 2, 3]. The sea oil biodegradation using psychrophile marine microorganisms have not been reported.

There are abundant low temperature microbe resources in Antarctic. Many components of oil can be biodegraded in the land and sea ecosystem of Antarctic. Indigenous microorganisms, especially psychrophile bacteria play important roles in the biodegradation [4, 5]. So the psychrophile bacteria have important biology and ecology meaning to oil pollutions bioremediation at low temperature. In this study, two biodegrading bacteria were screened from 385 Antarctic sea bacteria strains and their biodegradation abilities were studied.

Received on November 28, 2007

1 Materials and methods

1.1 Bacterial strains

Bacterial strains were isolated and purified from Antarctic seawater, sea-ice and sea mug which were collected during the 19th Chinese Antarctic Science Exploration in 2002-2003. Strains were conserved in the key Laboratory of Marine Bio-active Substances SOA.

1.2 Reagents and culture medias

Diesel used for degradation is No.0 on the sale.

Isolation media 2216E: peptone 0.5 % and yeast extract 0.1 %, pH7.0 - 7.5. The media was autoclaved at 121 °C for 20 mins.

Screening media (MMC): NaCl 24 g/dm^3, $MgSO_4 \cdot 7H_2O$ 7.0 g/dm^3, NH_4NO_3 1.0 g/dm^3, KCl 0.7 g/dm^3, KH_2PO_4 2.0 g/dm^3, Na_2HPO_4 3.0 g/dm^3, pH 7.4. The media were supplemented some of microelements and diesel oil which is the sole carbon source after sterilization. Diesel oil and microelements were sterilized by 0.2 μm microfiltration membranes.

1.3 Biodegradation ability assay

The bacteria cultures were incubated at 7 °C on rotary shaker operated at 120 r/m for 24h, then bacteria cultures were washed twice with sterilized MMC. 1g pre-sterilized diesel oil was added to 100 ml pre-sterilized medium. These mediums were inoculated with bacterial suspension previously prepared and incubated at 5 °C, 10 °C and 15 °C on rotary shaker operated at 120 r/min for 20 days respectively. The MMC were centrifuged at 10 000 r/min for 10 mins and the supernatant liquids were filtrated with 0.2 μm filter membrane. Uninoculated MMC liquid medium was controlled and incubated in parallel. The residues of diesel oil were assayed by fluorospectrophotometry [6].

1.4 Growth curve assay

5.0 ml activated bacteria suspension which have been washed by MMC twice were added both 100 ml 2216E and 100 ml MMC (diesel oil is the sole carbon source). Then they were incubated at 5 °C on a rotary shaker operated at 120 r/min. Samples were performed on 540 nm with spectrophotometer every 24 h. Make the growth curve with the sampling time as abscissa and the OD_{540nm} values as vertical coordinate.

1.5 GC-MS analysis

2 ml MMC which used diesel oil as the sole carbon source has been cultured at 5 °C, 120 rpm for 20 days and it was centrifuged with 10 000 r/min for 10 mins. The supernatants were filtrated with 0.1 microfiltration membranes and be used for analysis. The MMC without bacteria was used as control.

6890N GC-5973N MS: HP-5 MS, 30 m × 0.25 mmID × 0.25 μm, FID, NIST.

Helium (99.99 %) was used as a carrier gas with a flow rate of 1 ml/min, and 1 uL sample was injected for each analysis. Split injection was used and the split ratio was 100: 1. The injector temperature was at 250 °C. The initial temperature was set at 160 °C for 5 mins, then 15 °C /min to 250 °C for 7 mins. MS conditions included ionization mode IE70eV, connections bar temperature 280 °C, ion source temperature 200 °C, solvent delay time 5 mins. Selection ion mode was used and selected ions were m/z60 and m/z150.

1.6 Isolation of genomic DNA

DNA of two strains NJ276 and NJ341 was extracted and precipitated following the CTAB protocol for bacteria1 genomic DNA preparations [7]. Polymerase chain reaction (PCR) products were amplified using the two PCR primers 16F27 (5'-dAGAGTTTGATCCTGGCTCAG-3') and R1488 (5'-dGGTTACCTTGTT A CGACTT-3'). PCR were performed with a thermal cycler by using 20 μl reaction mixtures containing deoxynucleoside triphosphates at concentrations of 0.02 mM, 1.0 μM of primers, 2 μL reaction buffer, 1 μL of five strains'genomic DNA and 1 U Taq DNA polymerase(Takara).The program used for the PCR was as follows：94 °C for 5 mins, then denaturation at 94 °C for 1 min, annealing at 53 °C for I min, and extension at 72 °C for 1 min 30 s, 30 cycles，and extension at 72 °C for 10 mins.

1.7 16S rDNA sequence analysis

For sequence analysis, about 1, 500 bp PCR products were subcloned into the vector pMD18-T. The nucleotide data for NJ276 and NJ341 have been deposited in the GenBank nucleotide sequence database under the Accession No. AY781153, AY781156. The multiple sequence alignment analysis was performed using CLUSTALW program. The evolutionary distances were calculated by the MEGALIGN program of DNASTAR (DNASTAR Inc.). And the phylogenic tree was constructed by the neighbor-joining phylogenic tree (50 majority rule). A boot strap analysis of 1 000 replicates was performed.

2 Result and analysis

2.1 Screening for Antarctic petrolic-hydrocarbon degrading bacteria

385 strains of Antarctic psychrophile bacteria were cultured in the MMC liquid substrate which used diesel oil for the only carbon source. And two strains of eugonic petrolic-hydrocarbon degrading bacteria were screened, and numbered NJ276 and NJ341 respectively.

2.2 Mensuration of diesel oil-degradation capability

The results of the oil degradation rate of 2 strains of Antarctic psychrophile bacteria are shown in Fig. 1. The test results showed both strains had good performances of removing diesel. Culture temperature is the biggest influencing factors for degradation ability. The degradation rate rises from 5 °C to 15 °C. The degradation rates of NJ276 and NJ341 cultured at 5 °C in 20 days are 23.47 % and 32.15 %,

and cultured at 15 °C for 20 days are 43.95 % and 62.47 %.

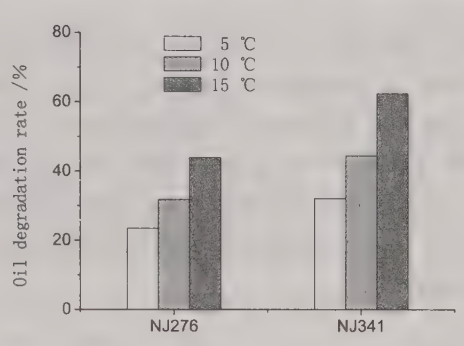

Fig. 1 Effect of temperature on the oil degradation rate of 2 Antarctic psychrophile bacteria

2.3 Growth curve of petrolic-hydrocarbon bacteria

Both strains NJ276 and NJ341 can grow well from 0 °C to 20 °C, and can't survive at 25 °C. The optimum grow-temperature of them is 15 °C. Morita identified the psychrophile and psychrotrophic, based on their different upper limits of grow-temperature [8]. Psychrophile bacteria could grow when the temperature is below 0 °C, and couldn't grow when temperature is above 20 °C, and the optimum grow-temperature is below 15 °C. Psychrophilic could grow when the temperature is 0 °C, and the optimum grow-temperature is between 20 °C - 30 °C. The strains NJ276 and NJ341 are belonged to psychrophile bacteria on the basis of definiens. The growth curves of strains NJ276 and NJ341 are shown in Fig. 2. NJ276 and NJ341 reached exponential growth period and steady period after 3 days incubated in 2216E substrate, and started decline after 6 days. NJ276 and NJ341 grow relatively slow in MMC substrate, which use diesel oil as the only carbon source. NJ276 and NJ341 reached exponential growth period and steady period after 4 days and started decline after 7 days. Both these two strains have thickness in MMC substrate which use diesel oil as the only carbon source, so they could use diesel oil as the carbon source.

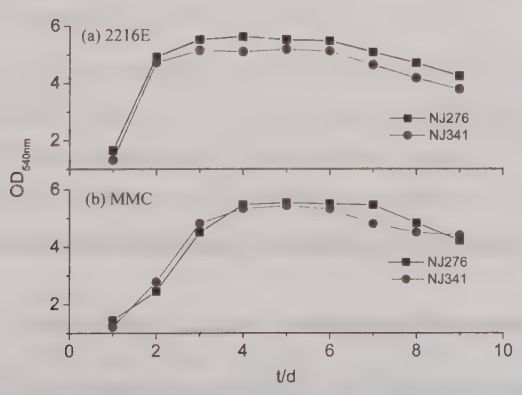

Fig.2 Effect of culture medium on the growth of 2 Antarctic psychrophilic bacteria

2.4 GC-MS Analysis of residual oil

Residual oil of the MMC substrates was analyzed by GC-MS. The results showed that the MMC without bacteria included 18 kinds of alkanes from C_9 to C_{26} (Fig. 3). Seven kinds of alkanes from C_{15} to C_{21} were detected in the residual oil components degraded by NJ276, and the kinds and contents of alkanes decreased significantly (Fig. 4). This has great relationship with the degradation ability of NJ276, and the high additive diesel oil could not be degraded in short time. But only 3 kinds of alkane C_{16}, C_{17} and C_{18} were detected in the residual oil components degraded by NJ341 (Fig. 5). This shows NJ341 has very strong diesel oil degradation capability.

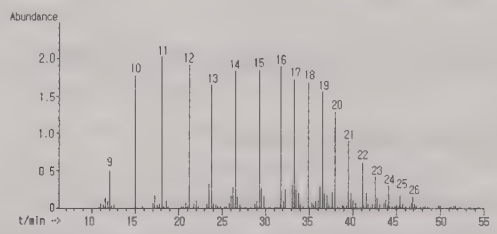

Fig.3 GC-MS of residual oil of the blank

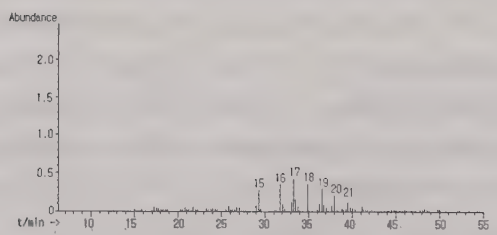

Fig.4 GC-MS of residual oil after degradation by Antarctic psychrophile bacteria NJ276

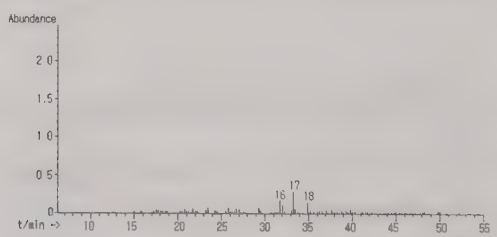

Fig.5 GC-MS of residual oil after degradation by Antarctic psychrophile bacteria NJ341

2.5 16S rDNA gene sequence and phylogenetic analysis of two strains

In order to contrast these two strains'16S rDNA sequence comparability, Clustalw software was used to translate those sequences to a format that PHYLIP could identify. The genetic distances of these

sequences were calculated by megAlian application from DNAstar software, and they were translated into the similarity. The similarity is 98.1% between strain NJ276 sequence and *Pseudoalteromonas agarivorans* sequence. Generally speaking, homology of 16S rDNA sequences below 97 % is considered belong to different species, and homology below 93 % - 95 % can be considered as different genus. So, strain NJ276 belongs to the genus *Pseudoalteromonas*. The sequence similarity between strain NJ341 and *Colwellia piezophila* was 94.8 %, and the strain NJ341 belonged to the genus Colwellia on the basis of 16S rDNA gene sequence analysis. Phylogenetic analyses based on 1 6S rRNA gene sequence information are shown in Fig. 6. Two strains belonged to the γ-proteobacteria subclass which was one of the greatest group proteobacteria. The strain NJ276 should belong to *Alteromonadales*, *Aheromonadaceae*, *Pseudoalteromonas*. The strain NJ341 should belong to *Alteromonadales*, *Alteromonadaceae*, *colwellia*. Both of two strains were typical psychrophile bacteria. Previous result indicated that the dominant sea ice bacteria1 groups represented are from the gamma subdivision of the *Proteobacteria* and the flavobacteria, and that *Colwellia* was described among the psychrophiles, and was found the predominant groups in clean ice including 29 % *Pseudoalteromonas* [9].

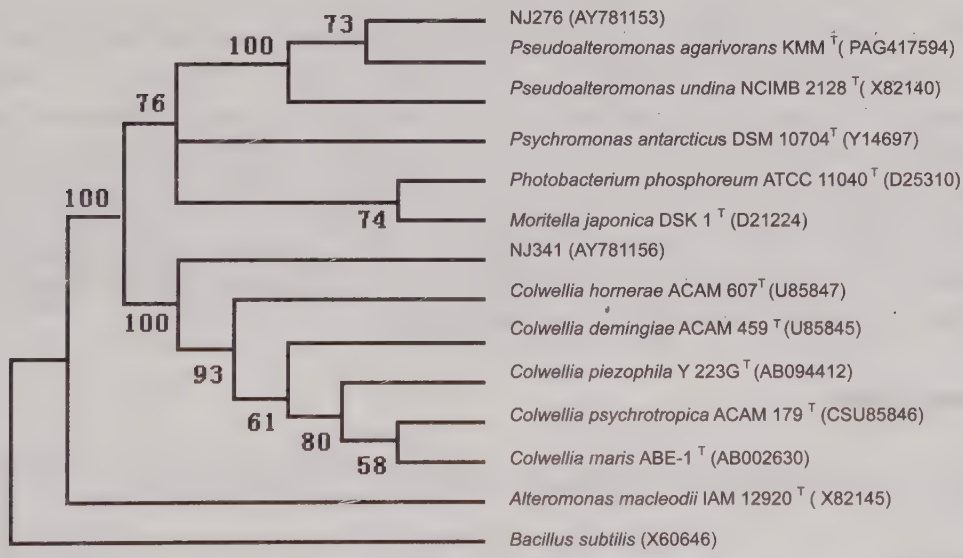

Fig. 6 Phylogenetic tree showing the relationships of strains of Antarctic hydrocarbon degradation bacterium producing protease with the sequences of relating genera constructed by the neighbour-joining method and based on 16S rDNA gene sequences, bootstrap values（above 50 %）are shown at the branch points. Submission number of the relating genera is available as supplementary data in IJSEM Online

3 Discussion

Oil pollution occurred more and more frequently and gave great harm to the sustainable development of the sea. With oil import increasing and development of the sea transportation year by year, the pollution to Chinese Coastal waters is becoming serious. Microbial degradation of petroleum

contaminants is considered to be the major decomposition process for decomposing petroleum contaminants in seawater. Many studies about marine hydrocarbon degradation bacteria were carried out in China, but most of them were mesophilic microorganism. There is no report on psychrophilic marine microorganism for petroleum hydrocarbon degradation in China. Low temperature is the key factor affecting biodegradation of petroleum in seawater of north China in winter. The seawater temperature is 0 °C - 4 °C from Dalian to Qingdao in winter. And mesophilic microorganisms stop growing and degrading petroleum. Therefore, the petroleum contamination in the offing of north China is serious in winter. But Antarctic psychrophile microorganism can degrade petroleum effectively at low temperature, which can be used to clear away petroleum contaminants in cold seawater.

Biodegradation of petroleum hydrocarbon at low temperature is attracting attached more and more attention all over the world. There are various microorganisms in the ice, snow, water, soil and rock in Antarctica. Psychrophile bacteria can grow at the temperature about 0 °C and can not grow above 20 °C. Their favorite temperature is below 15 °C [8]. Some microorganisms for degrading hydrocarbon have been screened in many countries and their latency characteristics for biodegradation of hydrocarbon have been studied [4, 5]. Petroleum hydrocarbon degrading bacteria NJ276 and NJ341 were screened from 385 strains Antarctic psychrophile bacteria, and their degrading characteristics were preliminarily studied, and their genus were identified by 16S rDNA in our study, which enriches the resource of Antarctic microorganism in China and offers a good method for bioremediation of petroleum contamination in cold environment. The mechanism that Antarctic psychrophile bacteria degrades petroleum hydrocarbon needs more research combined with the environmental factors in the offing of north China in winter. These studies have important application prospect, and will provide new technology to clear away petroleum contaminants in the offing of north China in spring and in winter, and have a great significance in bioremediation of petroleum contamination in cold environment.

Acknowledgements

This work was supported by the Natural Science Foundation of China (No. 40876107).

References

[1] Okoh A I. Biodegradation alternative in the cleanup of petroleum hydrocarbon pollutants[J]. Biotechnol. Moe. Biol. Rev., 2006, 1 (2): 38 - 50.

[2] Song Z W, Xia W X, CAO J. Biodegradation and bioremediation of petroleum contaminants in seawater [J]. Chinese Journal of Ecology, 2004, 23(3): 99 - 102.

[3] Liu C L, Shao Z Z. Isolation and characterization of oil-degrading marine micro-organisms [J]. Acta. Oceanologica. Sinica., 2005,27(4): 114 - 120.

[4] Aislabie J, Mcleod M, Fraser R. Potential for biodegradation of hydrocarbons in soil from the Ross Dependency, Antarctica [J]. Appl. Microbiol. Biotechnol., 1998, 49: 210 - 214.

[5] Powell S M, Bowman J P, Snape I. Degradation of nonane by bacteria from Antarctic marine sediment [J]. Polar Biol., 2004, 27: 573 - 578.

[6] Wang Q, Shao M H, Tao P. Determination of total petroleum in halobios by fluorescence spectrophotometry [J]. Journal of Dalian Maritime University, 2006, 32(1): 51 - 53.

[7] Wilsan K. Preparation of genomic DNA from bacteria. Current protocols in molecular biology [M]. New York: J Wiley &Sons, 1987.

[8] Morita R Y. Psychrophilic bacteria [J]. Bacteriol. Rev., 1975, 39: 144 -167.

[9] Bowman J P, Mccammon S A, BROWN M V, et al. Diversity and association of psychrophilic bacteria in Antarctic sea ice [J]. Appl. Environ. Microbiol, 1997, 63: 3 068 - 3 078.

南极石油烃降解嗜冷菌的筛选及其降解特性的研究

郑 洲[1,2]，金 青[3]，缪锦来[1,2]，刘芳明[1,2]

（1. 国家海洋局第一海洋研究所，山东 青岛 266061；2. 海洋生物活性物质国家海洋局重点实验室，山东 青岛 266061；
3. 青岛科技大学，山东 青岛 266042）

摘 要：从 385 株南极海洋细菌中筛选出 2 株石油烃降解菌，并对其降解特性进行了初步研究。以柴油为唯一碳源进行降解实验的结果表明，南极嗜冷菌 NJ276 和 NJ341 在 5 °C、20 d 内对柴油的降解率分别达到 23.47 % 和32.15 %，在 15 °C、20 d 内降解率分别达到 43.95 % 和 62.47 %，其降解能力随着培养温度的升高而显著增强；石油烃降解残油组分的GC ～ MS分析表明，柴油经过 NJ276 降解后的残油组分中能检测到 C_{15} ～ C_{21} 七种烷烃，柴油经过 NJ341 降解后的残油组分只能检测到少量 C_{16}，C_{17} 和 C_{18} 三种烷烃。对它们进行 16S rDNA 基因序列的同源性和系统发育分析表明，菌株 NJ276 属于假交替单胞菌属（*Pseudoalteromonas*），NJ341 属于科尔韦尔氏属（*Colwellia*）。

关键词：南极嗜冷菌；石油烃；生物降解

Study on Different Size-fractionated Phytoplankton Assemblage Change in the Mesocosm Ecosystem

LI Tao[1,2], LIU Sheng[1], HUANG Liangmin[1], JIAN Weijun[4], YAN Yan[1,3]

1. *LMB and LED, South China Sea Institute of Oceanology, CAS, Guangzhou* 510301, *Guangdong, China;*
2. *Tropical Marine Biological Research Station in Hainan, CAS, Sanya* 572000, *Hainan, China;*
3. *Marine Biology Research Station at Daya Bay, CAS, Huizhou* 518121, *Guangdong, China*
4. *Key Laboratory for Coastal & Atmospheric Research, IER, Shenzhen* 518057, *Guangdong, China*

Abstract: A algal bloom process had been simulated via field mesocosm experiment, and the change of phytoplankton assemblage of different sizes in different growing phases had been studied. Nutrients addition could promote the growth of phytoplankton. In the mesocosm of *Prorocentrum donghaiense* (M1) and the mesocosm of natural waters (M2), and the peaks of chlorophyll *a* were 112.79 mg/m and 235.60 mg/m, respectively. The restraining effect of nano-phytoplankton on pico-phytoplankton growth was stronger in M2 than in M1. When nutrients were abundant, the relative growth rate of diatom was higher than that of *P. donghaiense,* and they reached the peak quickly and then came to die out very fast. The decreasing of Si promoted diatom bloom to die out.

Keywords: Daya Bay; Mesocosm; Phytoplankton; Size fractionation; Community change

1 Introduction

The laboratory research results could not be applied directly at natural sea area due to many factors (Lin, et al. 1994b). At present, researches on mesocosm ecosystem simulatively have become an effective means to understand marine ecosystem (Chen, et al. 1999; Guo, et al. 2000). In mesocosm ecosystem, marine natural environment and its ecological process were simulated by artificially controlling the environmental conditions, and the disturbing effect of diversified environmental factors on the maritime experiments had been lessened (Parsons, et al. 1978; Li, et al. 2001). The difference between indoor experiment and sea area had also been shortened. Although it would not completely accord with the spot, we could gain some results reflecting the true status of natural ecosystem and some ecosystem-scale informations, and could study quantificationally on the mechanism (Li, 1990; Tang, et al. 1995; Chen, et al. 1999; Qiao, et al. 2000).

Responses of phytoplankton to different proportional nutrients were studied by Harrison & Turpin (1982) using mesocosm set. Lin, et al. (1992; 1994a; 1994b) had adopted the method of adding nutrients

Received on November 23, 2007

into mesocosms to research the algal bloom caused by eutrophication. Large-scale *Prorocentrum donghaiense* blooms have occurred in the East China Sea in recent years (Lu & Goebel, 2001). The competition between *P. donghaiense* and *Skeletonema costatum* (Li, et al. 2001; 2003) and the effect of different proportional nutrient on phytoplankton and its assimilating and releasing dynamics (Shi, et al. 2003) had been studied using mesocosm experiment. Hou, et al. (2006) had discussed the effect of rich-phosphorus on the growth of *P. donghaiense* and *S. Costatum* and the change of nutrient in mesocosms. Zhang, et al. (2006) had studied the effect of nutrients on the growth of *P. donghaiense* in mesocosm ecosystem.

In order to understand the competition among different eco-place assemblages in phytoplankton community and its succession, we had done field mesocosm experiment to simulate an algal bloom process. This paper focused on the variations of Chlorophyll *a*, cell density of different size-fractionated phytoplankton and nutrients in different growing phases.

2 Material and method

The experimental alga, *Prorocentrum donghaiense*, was offered by CEOHAB Program. The field experiment was carried through at Dapeng'ao fishing raft located in the Daya Bay, Dongshan Village, Dapeng Town, Shenzhen City, Guangdong.

The diameter of four mesocosm bags made of white fibre-fabric was 2 m and the depth was 2.5 m. These bags were fixed in four cages on the fishing raft and marked as A, B, C and D. Sea water around the fishing raft was pumped into these four bags after getting rid of zooplankton and microphytoplankton by means of covering a 160 μm mesh net and a 77 μm mesh net at the infall and outfall of the water pipe, respectively. And then the bags were covered with fibre-fabric and placed stably on the fishing raft for 10 days.

Culture medium was added into the bags based on f/2 Medium. *P. donghaiense* was expensively cultivated and then added into A and B (f/2 - Si), and the initial cell density was about 5×10^5 cells/L. Each one was added 180 L algae and the salinity was about 30. At the same time, natural sea water near the fishing raft was added into C and D.

Water samples were taken with organic glass container after slowly mixing round the algae in mesocosms, and then put into the sealed pots and carried back to Marine Biology Research Station at the Daya Bay, CAS. Water temperature and salinity were mensurated using YSI 6600 system (Yellow Springs. Instrument Co. USA) in spot. Chlorophyll *a* was mensurated using fluorometry (10AU Turner Design USA). Nutrients water samples were frozen after filtrated with 0.45 μm cellulose acetate film, and then taken back to the laboratory and mensurated using nutrient flow analyer (Skalar san plus flow analyzer). Nano-phytoplankton was counted and identified under light microscope. Picophytoplankton was mensurated using flow cytometry (FACS calibar, BD).

A and B were analyzed as parallel samples and marked as M1, and their data were averaged and calculated the standard deviation; similarly, C and D were also analyzed as parallel samples and marked as M2.

Formula of relative growth rate (K) was list as follows:

$$K = \frac{\lg N_t - \lg N_0}{t}$$

N_0—cells density at the beginning, N_t—cells density after cultivated t time, t—cultivated time.

3 Results and Discussion

3.1 Temperature and salinity

The range of temperature was from 23.37 °C to 27.12 °C in the waters of four mesocosms and the salinity was from 29.65 to 31.15. The temperature and salinity among mesocosms differed less during culture experiment. Both of them were basically within the fitting range of phytoplankton. In tropical and subtropical sea area, the water temperature range fitting for phytoplankton's growth was 22 °C - 26 °C, and salinity range was 20 - 30 (Lin, et al. 1994; Huang, et al. 2002).

3.2 Growth change of phytoplankton

3.2.1 Change of Chlorophyll *a*

The results showed that the content of Chlorophyll *a* increased obviously in M1 and M2 (Fig. 1). It suggested that nutrients addition could promote the growth of phytoplankton. The content of Chlorophyll *a* reached the maximum earlier in M2 than in M1. The content of Chlorophyll *a* entered the exponential growth phase on the 4th day, and then reached its maximum of 112.79 mg/m on the 7th day, and subsequently stated to reduce gradually in M1; while in M2, it got the peak on the 4th day with the maximum of 235.60 mg/m, and on the 5th day, the content of Chlorophyll *a* kept in high level and in the plateau phase, and later began to reduce. Phytoplankton in natural waters (M2) grew faster than *P. donghaiense* (M1) under the same environmental condition. Its peak value of Chlorophyll *a* was higher, and it also came to die out faster in M2.

3.2.2 Change of phytoplankton

The results showed that there were many minitype diatom species in M1 except for *P. donghaiense*, and the dominant species was *S. costatum*. The dominant species in M2 was also *S. costatum*. The changing trend of nano-phytoplankton in mesocosms was showed in Fig. 2. Nano-phytoplankton in M1 began to enter the exponential growth phase on the 4th day and the cell density reached its maximum 1.84×10^7 cells/mL on the 6th day, and then began to decrease gradually. Being similar with the change of Chlorophyll *a*, nano-phytoplankton in M2 also grew faster than that in M1 and got the peak on the 5th day, and the cell density was 2.85×10^7 cells/mL, which was higher than that in M1. Later, and it also began to

decrease gradually.

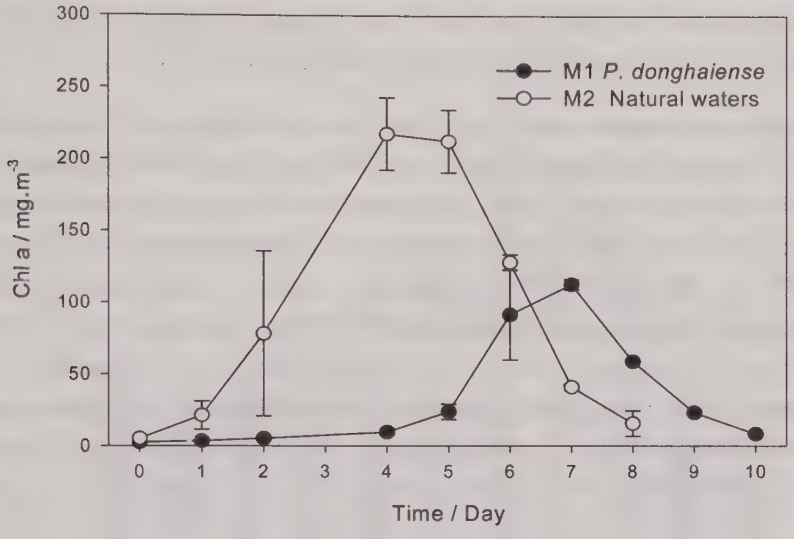

Fig.1 Changing trend of Chlorophyll *a*

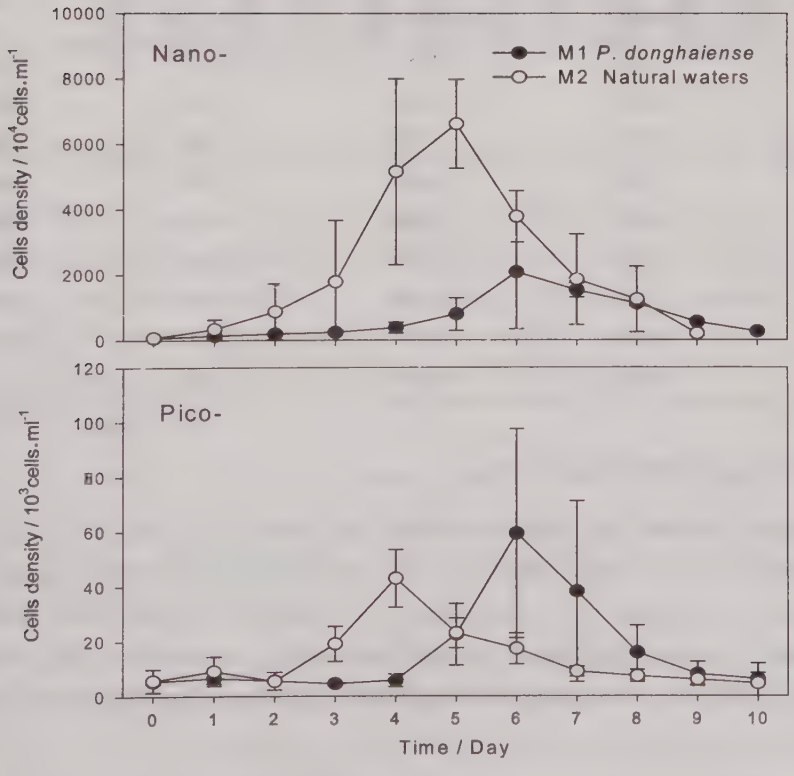

Fig.2 Trend of phytoplankton of different sizes in mesocosm experiments

Tab. 1 showed that relative growth rate (*K*) of nano-phytoplankton in M2 was higher than that in M1, and it got the maximum of 0.655 / d on the 1st day and then tended to reduce gradually. The value of *K* in M1 also reached its maximum of 0.303 / d on the 1st day. It began to decrease on the 2nd day and had ascended a little since the 5th day and reduced gradually after the 7th day.

Flow cytometry measurement results show that, pico-phytoplankton in mesocosms was mainly picoeukaryotes and there was few *Synechococcus* spp. The reason might be that the sea water for culture was taken from the water area of cage culture. The growth trend of pico-phytoplankton in M1 was similar with that of nano-phytoplankton. It also entered the exponential growth phase on the 4th day and reached its maximum 3.82×10^4 cells/mL on the 6th day, and then started to decrease gradually. What different from nano-phytoplankton was that, pico-phytoplankton in M2 grew faster than that in M1 and it got the peak on the 4th day, but its cell density was 1.05×10^4 cells/mL and less than that of M1. It had entered the dying-out phase since the 5th day and its cell density decreased continuously. It illuminated that, there was competing relationship between nano-phytoplankton and pico-phytoplankton, and because of largely multiplication, the restrain function of nano-phytoplankton to pico-phytoplankton in M2 was much greater than in M1.

Tab.1 Relative growth rate of phytoplankton in different mesocosms

Cultivating time / d	M1			M2
	Total	*P. donghaiense*	Other algae	
1	0.303	0.267	0.653	0.655
2	0.228	0.203	0.445	0.533
4	0.180	0.155	0.364	0.459
5	0.188	0.150	0.375	0.460
6	0.214	0.144	0.411	0.390
7	0.248	0.123	0.439	0.284
8	0.194	0.124	0.346	0.199
9	0.153	0.129	0.255	0.153
10	0.102	0.091	0.171	-

3.2.3 Growth change of different algae in M1

P. donghaiense reached the peak on the 8th day and the maximum of cell density was 6.77×10^6 cells/mL, and then started to die out and reduced slowly (Fig. 3). Other algae increase rapidly and their quantities exceeded that of *P. donghaiense* on the 5th day. They reached the maximum on the 6th day which was two days earlier than *P. donghaiense* and their cell density was1.73×10^7 cells/mL. Later they began to decrease continuously and their quantities had been less than that of *P. donghaiense* since the 8th day.

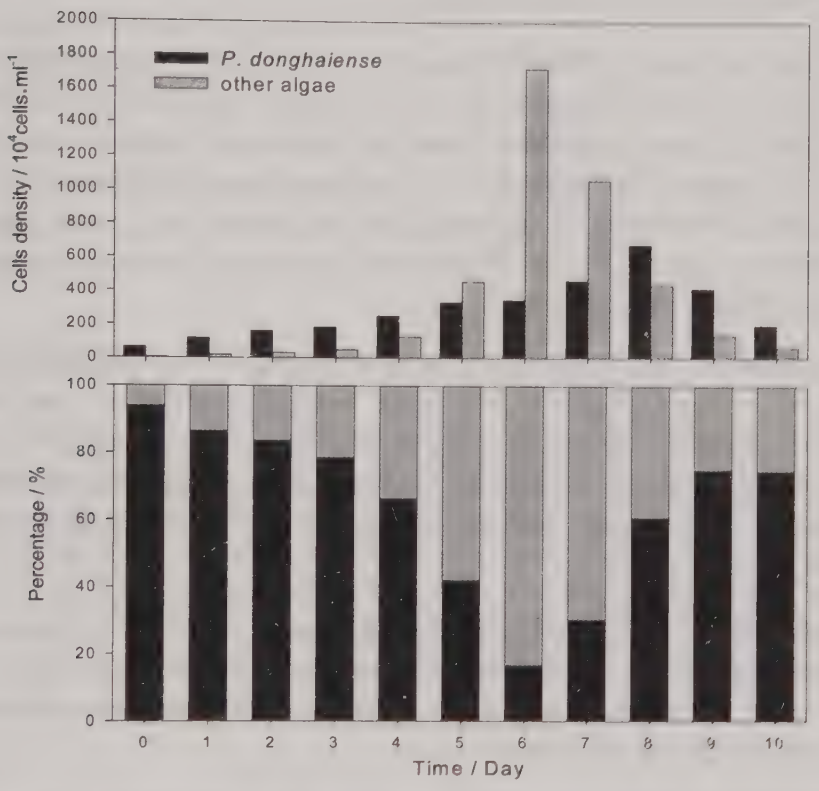

Fig.3 Trend of densities and proportions of *Prorocentrum donghaiense* and other algae in M1

Based on the percentages of their cell densities in total cell density, the proportion of *P. donghaiense* tended to decrease first and then increase. Because *P. donghaiense* was added into the mesocosms after expansive culture, its proportion was rather high at the beginning. Along with other algae largely growing, the proportion of *P. donghaiense* reduced gradually and got the minimum on the 6th day and accounted for only 16.7 % of total cell density. Thereafter, since other algae began to die out, the proportion of *P. donghaiense* slowly increased again.

As relative growth rate concerned, the relative growth rate of *P. donghaiense* in M1 was much smaller than that of other algae. *K* value of *P. donghaiense* got the maximum 0.267 / d on the 1st day, while *K* value of other algae on the 1st day was 0.653 / d and also was the most. Later, both of their *K* value took on a continuously descending trend.

Thus it can be seen that, under high nutrients conditions, the multiplication velocity of phytoplankton (especially diatom) in natural waters was faster than that of *P. donghaiense* and the time of reaching the peak was relatively small. But with the algae consuming a lot of nutrients for their growth and entering the dying-out phase, under nutrients-limited conditions, *P. donghaiense* grew better than other algae. This result was similar with the mesocosm experiment of Li et al. (2003).

3.3 Change of nutrients in the waters of mesocosm ecosystem

Fig. 4 showed that the nitrate (NO_3-N) in the waters of M1 and M2 tended to decrease at first and then increase. In the mesocosm ecosystem, the phytoplankton consumed NO_3-N for its growth so the concentration of NO_3-N started to decrease. When the phytoplankton reached its growth peak and Chlorophyll *a* got its maximum, the concentration of NO_3-N reduced to its minimum after one day later. The minimum of NO_3-N in the waters of M1 appearing on the 7th day was 424.07 μmol/L, and that of M2 appearing on the 5th day was 491.0 μmol/L. Subsequently, because the phytoplankton started to die out, the concentration of NO_3-N increased a little.

The concentration of nitrite (NO_2-N) took on an increasing trend. The concentration of NO_2-N in the waters of M1 increased from 1.70 μmol/L to 10.21 μmol/L, while that of M2 increased from 2.46 μmol/L to 15.93 μmol/L. The increase of NO_2-N was likely to have relation with the ability of phytoplankton selectively assimilating different forms of nitrogen. The ability of different algae using dissoluble inorganic nitrogen was different, and at the same time some kinds of bacteria also might translate NO_3-N into NO_2-N (Wang, et al. 2002).

The changing trend of phosphate (PO_4-P) was similar to that of NO_3-N, and it also decreased at first and then increased. PO_4-P in the waters of M1 and M2 reduced to the minimum on the 7th and 6th day respectively, and the concentrations were 13.41 μmol/L and 12.63 μmol/L respectively. Later, the concentration of PO_4-P began to ascend again.

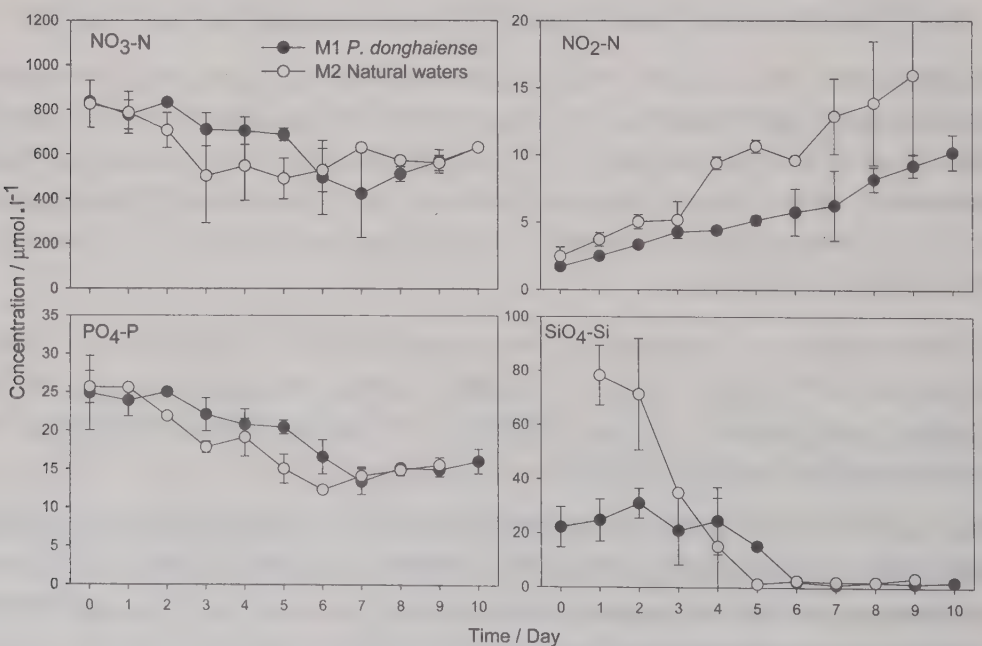

Fig.4 Trend of nutrients in the waters of different mesocosm experiments

Since the nano-phytoplankton community in M1 was dominated by *P. donghaiense*, silicate (SiO_4-Si) changed less at the beginning. Along with the increasing of other algae, SiO_4-Si had began to reduce since the 3rd day and reached its minimum of 1.0 μmol/L on the 6th day. While the nano-phytoplankton was predominated by diatom, SiO_4-Si took on a decreasing trend with its minimum of 0.96 μmol/L on the fifth day. The time of SiO_4-Si reducing to the minimum in M1 and M2 was according with that of the cell density of nano-phytoplankton reaching the maximum. It indicated that the growth of diatom consumed a great deal of SiO_4-Si, and the dead cells sedimentated to the bottom of mesocosm bag, so as to the silicon cannot be supplied in time, accordingly promoting diatom bloom to die out and the cell quantity of diatom descended continuously.

Acknowledgments

We thank the anonymous reviewers and Li Kaizhi for their very helpful comments on this work. This work was supported by National '973' Program (2001CB409707), the Natural Science Foundation of China (No. 40206016 and U0633007), the Key Program of National Natural Science Foundation of China (No. 40531006) and the Field Platform & Station Foundation of CAS. The data of water temperature, salinity, Chlorophyll *a* and nano-phytoplankton were offered by the 8th problem team (remote sensing problem) of CEOHAB Program. We thank Yang Anan, Zhu Jianhua, Li Gang and Zhou Hongli of National Ocean Technology Center for taking part in this mesocosm experiment.

Reference

[1] Chen S, Zhu M Y, Ma Y, et al. Study of the effects of eutrophication on marine ecosystem by mesocosm experiments [J]. Advance in Earth Sciences, 1999, 14(6): 571 - 576.

[2] Guo Weidong, Hu Minghui, Yang Yiping, et al. MEEE study on heavy metal release and transport from estuarine polluted sediments [J]. Journal of Oceanography in Taiwan Strait, 2000, 19(3): 276-283.

[3] Harrison P J, Turpin D H. The manipulation of physical, chemical and biological factors to select species from natural phytoplankton communities. In: Grice G. D. and Reeve M. R. eds. *Mesocosm*. New York: Springer-Verlag, 1982. 275 - 289.

[4] Huang X P, Huang L M, Tan Y H, et al. Relationship between red tide and environmental conditions in coastal waters [J]. Marine Environmental Science, 21(4): 63 - 69.

[5] Li B H, Cheng S, Zhu M Y. Effects of rich phosphate and oil pollutant on the variances in Chlorophyll-a in mesocosm ecosystem [J]. Journal of Oceanography of Huanghai & Bohai Seas, 2001, 19(4): 30 - 36.

[6] Li G G. Different types of ecosystem experiments. In: Lalli, C. M. ed. Enclosed experimental marine ecosystem: A review and recommendations. 1990, London, Springer-Verlag: 7-19.

[7] Li R X, Zhu M Y, Chen S, et al. Responses of phytoplankton on phosphate enrichment in mesocosms [J]. Acta Ecologica Sinica, 2001, 21 (4): 603 - 606.

[8] Li R X, Zhu M Y, Wang Z L, et al. Mesocosm experiment on competition between two HAB species in East China

Sea [J]. Chinese Journal of Applied Ecology, 2003, 14(7): 1 049 - 1 054.

[9] Lin Y, Chen X L, Zhuang D F, et al. Preliminary analysis for the structures of phytoplankton community in a marine enclosed ecosystem before and after a red tide process [J]. Acta Ecologica Sinica, 1992, 12 (3): 213 - 218.

[10] Lin Y, Tang S M, Chen X L, et al. Effect of inorganic nitrogen on phytoplankton successio in marine mesocosms [J]. Acta Ecologica Sinica, 1994.14 (3): 323 - 326.

[11] Lin Y, Zhuang D F, Chen X L, et al. Preliminary study on red tide formation based on results from enclosed experimental ecosystems-The relationship between diatom red tide with some physical and chemical factors. Oceanologia Et Limnologia Sinica, 1994b, 25 (2): 139 - 145.

[12] Lin Y S, Zhou Y C, Wang G C. Red tide organisms and their relationships with environment in the zhujiang estuary [J]. Tropic Oceanology, 1994, 13(4): 58 - 64.

[13] Lu D D, Goebel J. Five red tide in genus *Prorocentrum* including the description of *Prorocentrum donghaiense* Lu sp. nov. from the East China Sea [J]. *Chin J Oceanol Limnol*, 2001, 19(4): 337 - 344.

[14] Parson T R, Harrison P J, Waters R. An experimental simulation of changes in diatom and flagellate blooms [J]. Journal of Experimental Marine Biology and Ecology, 1978, 32(3): 285 - 294.

[15] Qiao Fangli, Zhu Mingyuan, Wan Zhenwen. The newest progress of numerical simulating research on marine ecosystem dynamics-be hopeful to refrain marine red tide [R]. Chine science and technology mensal report, 2000, 6: 44 - 45.

[16] Tang Senming, Hou Shuming. Manner of polluted stress acting on the phytoplankton population in marine mesocosm ecosystem [J]. Acta Oceanologica Sinica, 1995, 17(5): 112 - 116.

[17] Wang L Q, Huang X X. The growth of Nannochloropsis oculata cultured in different nutrient concentrations and the variations of nitrogen and phosphorus in culture tanks [J]. Journal of Shanghai Fisheries University, 2002, 11 (3): 215 - 218.

[18] Shi X Y, Wang X L, Han X R, et al. Nutrient distribution and its controlling mechanism in adjacent area of Changjiang River estuary [J]. Chinese Journal of Applied Ecology, 2003, 14 (7): 1 086 - 1 092.

[19] Hou J L, Zhang C S, Shi X Y, et al. Effect of phosphate on two typical HAB species in East China Sea by Mesocosm Experiments [J]. Periodical of Ocean University of China, 2006, 36 (Sup.): 163 - 169.

[20] Zhang C L, Shi X Y, Han X R, et al. Mesocosm experiments of the effects of nutrients on the growth of dominant HAB species in the East China Sea [J]. Marine Fisheried Research, 2006, 27 (4): 29 - 35.

围隔生态系内不同粒级浮游植物群落变化研究

李 涛[1,2], 刘 胜[1], 黄良民[1], 简伟军[4], 严 岩[1,3]

(1. LMB 和 LED, 中国科学院南海海洋研究所, 广东 广州, 510301; 2. 中国科学院海南热带海洋生物实验站, 海南 三亚, 572000; 3. 中国科学院大亚湾海洋生物综合实验站, 广东 深圳, 518121; 4. 深港产学研基地海岸与大气研究重点实验室, 广东 深圳, 518057)

摘 要: 通过现场围隔实验, 模拟赤潮发生过程, 研究了种群不同生长阶段中不同粒级浮游植物种群的变化情况。结果表明, 添加营养盐能有效促进浮游植物的生长, 东海原甲藻围隔(M1)和自然水体围隔(M2)中浮游植物分别于第 7 天和第 4 天出现生长高峰, 叶绿素 *a* 最大值分别为 112.79 mg/m 和 235.60 mg/m。微型浮游植物与微微型浮游植物存在竞争, 微型对微微型生长的抑制作用: M2>M1。在营养盐丰富时, 硅藻的增殖速率比东海原甲藻快, 达到高峰期时间短, 消亡也快。硅的减少促进硅藻水华的消亡。

关键词: 大亚湾; 围隔; 浮游植物; 粒级; 群落变化

Correlation and Path Analysis for Growth Traits in F_1 Population of Pearl Oyster *Pinctada martensii*

DENG Yuewen, DU Xiaodong, WANG Qingheng, FU Shao, HUANG Ronglian

Fisheries College, Guangdong Ocean University, Zhanjiang 524025, *Guangdong, China*

Abstract: 120 pearl oysters (*Pinctada martensii)* were randomly sampled from F_1 population, and shell length, shell width, shell height, shell weight and total weight of each sample were measured. Correlation and path analysis were conducted on the basis of measurement data. The results showed that shell length, shell width, shell height, shell weight and total weight were significantly correlated ($P < 0.05$). Total weight was significantly and positively correlated with shell weight (r = 0.8970), shell height (r = 0.6974), shell width (r = 0.6521) and shell length (r = 0.5486). Shell weight, shell height, shell width and shell length had positive and direct effects on total wet weight, with the values of 0.6356, 0.1872, 0.1814 and 0.0599, respectively. The results indicated that growth traits (shell length, shell width, shell height, shell weight and total wet weigh) of the F_1 population could be improved by direct or indirect selection.

Keywords: *Pinctada martensii*; selected line F_1; growth traits; correlation; path analysis

Introduction

Selective breeding is a classic and fundamental approach to improve certain economic traits in shellfish species. Genetic improvement in growth traits such as shell length and total weight by selective breeding has been observed in several shellfish species, which include Pacific oyster *Crassostrea gigas*, the American oyster *Crassostrea virginica*, the Chile oyster *Ostrea chilensis*, the European oyster *Ostrea edulis*, blue mussel *Mytilus edulis*, bay scallop *Argopecten irradians*, pearl oyster *Pinctada martensii*, scallop *Placopecten magellanicus* and Pacific abalone *Haliotis discus hannai* [1, 2].

Pearl oyster *Pinctada martensii* is an important species and widely cultured in the southern sea of China. In the past decade, breeding studies on the species have included polyploidy induction [3-5], hybridization [6, 7] and mass selection [8, 9]. When planning selection programs, breeders are interested to know the relationship of the selected traits. Phenotypic correlation among growth traits of pearl oyster *P. martensii* has been well documented [10]. However, phenotypic correlations of growth traits are complex and result from the interaction of these traits. A further understanding on correlation among growth traits will be obtained by path analysis, which has been successfully used to assist in selective breeding programs of other aquatic animal [11, 12].

The present study was to estimate the phenotypic correlation for growth traits and evaluate the

Received on December 26, 2006

relative contribution of some growth traits to total weight by path analysis. The objectives were to provide some useful information on a sustained selection for faster growth rate in the F_1 population of pearl oyster *P. martensii*.

1 Materials and methods

1.1 Base population

In April 2004, 100 mature animals were randomly collected from each of two cultivated stocks: Leizhou, Guangdong and Beibu Bay, Guangxi. The breeders were mass spawned in the hatchery. Larvae were reared following the techniques of Wada et al (1986) [9]. Fertilized eggs were incubated in 200-l polyethylene tanks until the D-shape larvae occurred at 24 h after fertilization. And then, the larvae were transferred to 1 000-l polyethylene tanks. The density was about 1 individual/ml. Water temperature was at 28 ± 1 °C and salinity was at 30 ± 1 ppt. Daily feeding consisted of *Isochrysis galban* from Day 2 to 5, and a mixture of *I. galban* and *I. zhanjianggensis* from Day 6 to 35. Feeding ration increased with ages. Every other day 500 l of sea water were replaced in each tank. At approximately 21 days, plastic films were provided as substrate for metamorphosis. At approximately 35 days, individuals as large as 3 - 8 mm were removed from films, transferred to the nets and suspended in floating nets in the sea of Leizhou, Guangdong. Shells were cleaned and placed in new nets at appropriate intervals.

In April 2005, the pearl oysters were brought back to the hatchery. 20 males and 40 females with largest size (based on shell length) were selected as the parents of the selected line.

1.2 Production of selected line F_1

In April 2005, the selected breeders were killed. Gametes from each sex in the line were pooled within sex and kept separately in 200-l polyethylene tanks. For each line, fertilization was initiated by pouring an adequate amount of pooled sperm into pooled eggs. Larval rearing techniques were the same for the production of base population except that the larvae of each line were reared separately in five 1000-l polyethylene tanks. The pearl oysters were reared in the same sea as their parents.

1.3 Sampling and measurement

In March 2006, 120 individuals were randomly sampled from the F_1 population and used for the trait measurement. The methods for trait measurement were detailed by Wang et al. (2004) [10]. The measured traits were as follows: shell length (SL, mm), shell height (SH, mm), shell width (SW, mm), shell weight (SHW, g) and total weight (TW, g).

1.4 Data analysis

The mean value and standard deviation of each trait were calculated and the variation coefficient (CV) of each trait was estimated using the following formula:

CV = (standard deviation/mean) × 100 %

The correlation coefficients among the traits were evaluated using software SPSS 11.0 version. Significant level was set $P < 0.05$. Path analysis was performed by the methods of Liu et al. (2002) [11] and Rodriguez et al. (2001) [13].

2 Results

The mean values and standard deviations of the growth traits in the F_1 population are shown in Tab. 1. The coefficients of variation of shell length, shell width, shell height, shell weight and total weight were 8.48 %, 10.82 %, 9.77 %, 11.55 % and 14.66 %, respectively.

Tab. 1 Mean values and variation coefficient of phenotypic traits in F_1 population

Traits	SL	SW	SH	SHW	TW
Mean	62.49	21.82	65.71	17.06	33.76
SD	5.3	2.36	6.42	1.97	4.95
CV %	8.48	10.82	9.77	11.55	14.66

Note: SL, shell length (mm); SH, shell height (mm); SW, shell width (mm); SHW, Shell weight (g); TW, total weight (g).

Phenotypic correlation coefficients among the traits are listed in Tab. 2. TW exhibited significantly positive correlation coefficients with SHW (r = 0.897 0), SH (r = 0.697 4), SW (r = 0.652 1) and SL (r = 0.548 6). SHW displayed significantly positive correlation coefficients with SH, SW and SL, with values of 0.643 9, 0.596 9 and 0.543 3, respectively. Significantly positive correlation coefficients were also detected between SH and SL, SH and SW, SW and SL.

Tab. 2 Phenotypic correlation coefficients among the traits

	SL	SW	SH	SHW	TW
SL	1	0.287 7*	0.486 6*	0.543 3*	0.548 6*
SW		1	0.395 6*	0.596 9*	0.652 1*
SH			1	0.643 9*	0.697 4*
SHW				1	0.897 0*
TW					1

* Correlations were significant ($P < 0.05$)

To further analyze direct and indirect effects of SL, SH, SW and SHW to TW, path analysis was made taking SL, SH, SW and SHW as independent variables and TW as independent variable (Tab. 3). Path analysis showed that the indirect effects of SL, SH and SW on TW were larger than direct effects of these traits on TW (Tab. 3).

Tab. 3 Direct and indirect effects of the other traits on total weight

Trait	Correlation	Direct effect	Indirect effect			
			SL	SW	SH	SHW
SL	0.548 6	0.059 9	-	0.052 2	0.091 1	0.345 3
SW	0.652 1	0.181 4	0.017 2	-	0.074 1	0.379 4
SH	0.697 4	0.187 2	0.029 1	0.071 8	-	0.409 3
SHW	0.897 0	0.635 6	0.032 5	0.108 3	0.120 5	-

4 Discussion

High variation has been proved to exist in pearl oyster *Pinctada martensii* populations [9, 14]. After a three-generation selection for several traits in a Japanese pearl oyster *P. fucata martensii* population realized heritability estimates for shell width and shell convexity at adult stage were 0.47 and 0.35, respectively [14]. The studies indicted that genetic improvement could be obtained by mass selection for these traits in pearl oyster *P. martensii* populations [9, 14]. When compared with the control line, He et al. (2006) reported that the selected line F_1 of pearl oyster *P. martensii* had significantly larger shell length, shell height, shell width and total weight at both juvenile and adult stages [14]. Our selection experiment also showed an approximately 20 % increase in shell length at adult stage after a one-generation selection for faster growth rate in the base population of pearl oyster *P. martensii*.

Generally, homozygosity increases after several generation selections and therefore variation coefficient decreases [17]. In the present, the selected line F_1 showed a decrease in variation coefficient for the traits studied. However, high variation coefficient for these traits was still observed in the selected line F_1. These results can be explained as follows: (a) Genetic variability in Baybu Bay stock has reported to be high as revealed by amplified fragment length polymorphism (AFLP). Considering the case that the base population was established by selecting parental breeders from both Beibu Bay and Liushagang stocks, the base population used for our selection experiment was postulated to have a high genetic variability. (b) The effects of inbreeding could be minimized but they weren't completely eliminated, because a larger number of breeders were used for production of the F_1 generation [16, 17]. High variation coefficient for growth traits implied that a sustained improvement could be obtained by mass selection at an appropriate intensity in F_1 population.

Significantly phenotypic correlations among growth traits have been reported in shellfish species [18-21]. For example, Wang et al. (2004) reported significant correlation coefficients in 11 quantitative traits of F_1 progenies produced by inter- and intra-crosses of geographical populations of pearl oyster *P. martensii* [10]. Our results also showed that there was significantly positive relationship among the traits. The results indicated that selection for a trait would result in related response in other traits. High correlation among the traits can be explained as pleiotropy in the determination of these traits [15].

Path analysis is effective in estimating the direct effect of one trait on another, and it separates the

relationship into its components of direct and indirect effects [13]. By path analysis on a stock of scallop *Chlamys farreri* collected in Dalian, Liaoning, the results showed that shell length, shell height and shell width exerted positively direct effects on total weight [11]. In the present study, the direct effects of shell length, shell width and shell height on total weight were smaller than the indirect effects of these traits on total weight. These traits exerted their effects on total weight by shell weight. An overall consideration of the direct and indirect effects of the measured traits in the present study could contribute to the success of sustained selection for faster growth in the F_1 population of pearl oyster *P. martensii*.

Acknowledgements

This study was supported by grants of the Guangdong Marine and Fishery Bureau (No. B02068) and Guangdong Ocean University (No. E06031).

References

[1] Wada K T. Aquaculture genetics of bivalve molluscs: a review. J. Ocean Univ. Qingdao, 2000, 30(1): 107-114.

[2] Zhang G F, Liu X. Theory and method of genetic improvement in mariculture mollusks: a review [J]. Journal of fisheries of China, 2006, 30(1): 130 - 136.

[3] Jiang W G, Xu G Q, Lin Y G, et al. Comparison of growth between triploid and diploid of *Pinctada martensii* (D.) [J]. Journal of Tropical Oceanography, 1991, 10(3): 1 - 7.

[4] He M X, Shen Q, Lin Y G, et al. Comparison of heterozygosity and growth between diploid, triploid and aneuploid pearl oyster *Pinctada martensii* (D.) [J]. Tropic Oceanology, 2000, 21(4): 55 - 62.

[5] Wang A M, Yan B, Lan G B. Comparative of three methods for the induction of tetraploidy pearl oyster (*Pinctada martensii* D.) [J]. Journal of Agricultural Biotechnology, 2004, 1: 64 - 69.

[6] Wang A M, Yan B, Ye L, et al. Comparison on main traits of F_1 from matings and crosses of different geographical populations in *Pinctada martensii* [J]. Journal of fisheries of China, 2003, 27(3): 200 - 206.

[7] Wang A M, Ding X L, Deng F J, et al. The genetic diversity of the first generation from matings and crosses of two wild populations (Daya Bay, Guangdong and Sanya, Hainan) in *Pinctada martensii* (Dunker) [J]. Marine Fisheries Research, 2003, 24(4): 19 - 25.

[8] Wang A M, Shi Y H, Yan B, et al. Effects of selection on larval growths for second generation of different selected pearl oysters, *Pinctada martensii* [J]. High Technology Letter, 2004, 14(1): 94 - 97.

[9] He M X, Shi J H. Lin Y G. Studies on growth traits of first generation of selective line of *Pinctada martensii* Dunker [J]. Journal of Tropical Oceanography, 2006, 25(10): 19 - 22.

[10] Wang A M, Shi Y H, Zhou Z G. Morphological trait parameters and their correlations of the first generation from matings and crosses of geographical populations of *Pinctada martensii* (Dunker) [J]. Marine Fisheries Research, 2004, 25(3): 39 - 45.

[11] Liu X L, Chang Y Q, Xiang J H, et al. Analysis of effects of shell size characters on live weight in Chinese scallop *Chlamys farreri* [J]. Oceanologia Et Limnologia Sinica, 2002, 33(6): 673 - 678.

[12] Liu X L, Wu C G, Zhang Z H, et al. Mathematical analysis of effects of morphometric attributes on body weight

Penaeus vannamei [J]. Acta Ecologica Sinica, 2004, 24(4): 857 - 861.

[13] Rodriguez D, Jasso D, Angulo-Sanchez J L, et al. Correlation and path coefficient analyses of the agronomic traits of a native population of guayule plants [J]. Industrial Crops and Products, 2001, 14: 93 - 103.

[14] Wada K T. Genetic selection for shell traits in the Japan pearl oyster, *Pinctada fucata martensii* [J]. Aquaculture, 1986, 57:171 - 176.

[15] Falconer D S. Introduction to quantitative genetics [M]. Longman Inc., New York, 1981.

[16] Wan J F, Bao Z M, Wang X L, et al. The influence of parental stock size on the genetic structure of *Haliotis discus* [J]. Journal of Fisheries of China, 2004, 28(2): 127 - 132.

[17] Kirpichnikov V S. Genetic bases of fish selection [M]. Springer-Verlag Berlin Heidelberg New York, 1981.

[18] Crenshaw J W, Heffernan P B, Walker R L. Heritability of growth rate in the southern Bay scallop, *Argopecten irradians concentricus* [J]. Journal of Shellfish Research, 1991, 10: 55 - 63.

[19] Toro J E, Newkirk G F. Divergent selection for growth rate in the European oyster *Ostrea edulis*: Response to selection and estimation of genetic parameters [J]. Marine ecology progress series, 1991, 4(2): 101-108

[20] Toro J E, Aguila P, Vergara A M. Spatial variation in response to selection for live weight and shell length from data on individually tagged Chilean native oyster (*Ostrea Chiensis* Philippi, 1845) [J]. Aquaculture, 1996, 146(1-2): 27 - 36.

[21] Ibarra A M, Ramirez J L, Ruiz C A, et al. Realized heritabilities and genetic correlation after dual selection for total weight and shell width in catarina scallop (*Argopecten ventricosus*) [J]. Aquaculture, 1999, 175:227 - 241.

马氏珠母贝选群 F_1 的表型性状的相关和通径分析

邓岳文，杜晓东，王庆恒，符 韶，黄荣莲

（广东海洋大学水产学院，广东 湛江，524025）

摘 要：从 7 月龄的 F_1 群体随机取样 120 个体，测量表型性状并进行相关和路径分析。所测量的表型性状包括壳长、壳高、壳宽、壳重和全湿重共 5 个指标。结果表明：（1）壳长、壳高、壳宽、壳重和全湿重存在显著的相关性（$P < 0.05$）。全湿重与壳长、壳高、壳宽和壳重存在显著的正相关（$P < 0.05$），相关系数分别为 0.897 0、0.697 4、0.652 1 和 0.548 6。（2）壳重、壳高、壳宽和壳长对全湿重具有正直接影响，其值分别为 0.635 6、0.187 2、0.181 4 和 0.059 9。结果说明了通过直接选择或间接选择可以改良马氏珠母贝选群 F_1 的壳长、壳高、壳宽、壳重和全湿重等生长性状。

关键词：马氏珠母贝；F_1 选群；生长性状；相关；路径分析

Dynamics Characteristics and Topographic Profile Shaping Process of Feiyan Shoal at the Yellow River Delta

YING Ming[1], LI Jiufa[2], CHEN Shenliang[2], DAI Zhijun[2]

1. *Shanghai Waterway Engineering Design and Consulting Co., Ltd., Shanghai* 200120, *China*

2. *State key laboratory of Estuarine and Coastal Research, East China Normal University, Shanghai* 200062, *China*

Abstract: Feiyan Shoal is a sub Yellow River Delta, which was formed from Jan. 1964 to May 1976, when the Yellow River entered sea via Diaokou Channel. Since the terminal reach shifted to Qingshuigou channel in 1976, Feiyan Shoal has been experiencing severe erosion and retreat. This paper explains the evolutionary characteristics of the typical profile of Feiyan Shoal from the perspective of dynamical force and sediments' characteristics. All this is on the basis of the data of topographic profiles observed since the 1970s and the samples of hydrology and sediments collected in situ in Apr. 2004, the analysis of the retreating distance, and the tidal and wave friction velocity distribution. Feiyan Shoal topographical profile has experienced a course of "fast erosion and retrogression - slow eroding modulation - fluctuate triggering change" in recent 30 years, which is also the gradual disappearing process of the delta front. The different intensity of sediment erosion resistance is the main reason for the erosion speed changes. Due to the hydrodynamic force changes, the water depth range of maximum retreating distance and between erosion and progradation became shallow. It indicates that the storm tide will still be the triggering force of seashore topographic profile evolutions in the future.

Keywords: The Yellow River Delta; Feiyan Shoal; erosion; wave and tidal co-action; topographic profile; sediment transport

Introduction

In the 20th century, about 70 % beaches were in recession while the silting coasts only accounted for less than 10 % in the world [1]. 24.4 % of the coasts eroded severely in the U.S.A. [2]. Coastal erosion has become a world problem, especially the erosion and retreating speed of mud and silt coasts, which is up to hundreds of meters each year, is much faster than that of rocky coasts. The sediment load of the Yellow River and the Yangtze River has been declining sharply since 1980s in China, and a large number of coasts are in erosion [3-9]. Since the Yellow River course changed to Shandong province and entered into the Bohai Sea in 1855, the modern Yellow River Delta between Bohai Bay and Laizhou Bay has formed, whose area is 9 380 km^2, including a land area of 5 880 km^2 and an underwater area of 3 500 km^2 [9]. Meanwhile the terminal reach shifts frequently. Up to now, it has greatly changed for 10 times, and correspondingly 10 sub-delta lobes have been formed [10, 11]. The abandoned sub-delta lobes

Received on December 25, 2007

without sediments supply fell into the state of eroding one after another. Coast erosion not only causes the disappearance of land resources, but also influences the development of resources along the coast. For example, Shengli Oil Field (the second largest oil field in China), located in Feiyan Shoal, has numerous oil wells and oil field facilities severely destroyed because of the coastal erosion. The economic benefits of Shengli Oil Field have suffered from direct loss. The area of coastal wetland is reducing constantly, and it weakens the ecological function of the littoral zone. The present status and reasons for coastal erosion are paid close attention to by numerous scholars [6, 7, 12-15]. However, past studies mainly focus on the space variation of the silting and eroding and the time-varying. Based on the field data, this paper discusses such dynamics as tide and wave, the characteristics of sediments, how the dynamics influence the silt and erosion process, and the shaping process of the profile, which provides some useful theoretical foundation for coastal protection engineering.

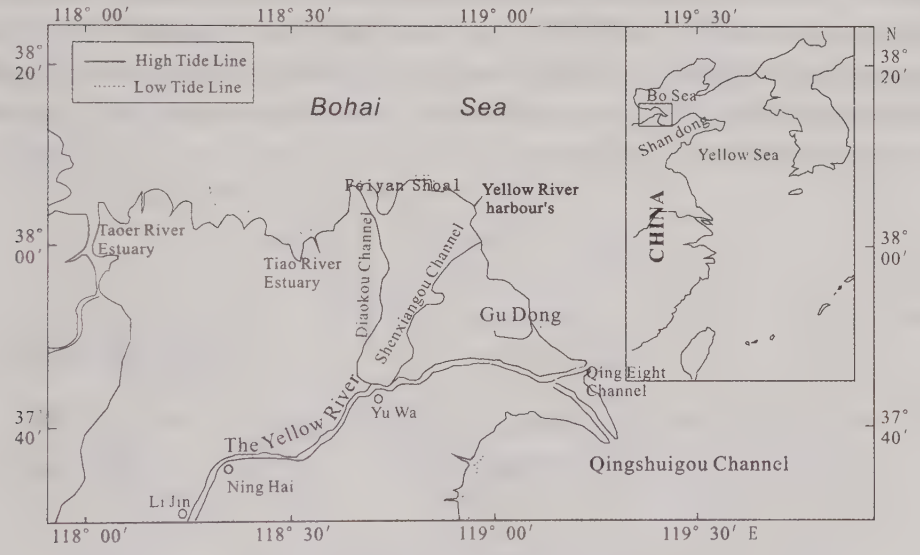

Fig. 1 Map of the Yellow River delta

1 The study area and data

1.1 The study area

Located at the northern Yellow River Delta (Fig. 1), Feiyan Shoal is a sub-delta lobe that was formed by about 71 × 10^8 t sediment from the Yellow River from Jan. 1964 to May 1976 [16, 17]. The coastal profile has the three zones of delta geomorphological structure, which consists of pro-delta, delta front and subsided delta platform [6]. The terminal reach shifted to Qingshuigou channel in 1976, and the effect of sediment diffused from the Yellow River is limited, and it's diffusion influence extension toward north can't exceed the Yellow River Harbour [18, 19]. Besides, sedimentation flux caused by sediment diffused from Qingshuigou channel is below 1 mm/a [20]. Therefore, after Feiyan Shoal was abandoned, there was no

influence of sediment supplied by the Yellow River basically. With the hydrodynamic action of tide, wave and storm tide etc., the seashore eroded constantly with the sediment diffusing to open sea. It is found that about 35.9 % of the sediment from the Yellow River, amounting to 40.67×10^8 t from 1964 to 1973, diffused to the open sea probably [16]. It indicates that on condition of sufficient sediment supplied from the river, sediment diffusing ability is up to 4×10^8 t/a in this sea area. It is inevitable that seashore erodes in circumstances of strong sediment diffusion and little sediment supply.

1.2 Data

Since the 1970s, coastal profiles have been observed regularly in the sea area of the Yellow River Delta by the Hydrology and Water Resource Investigation Institution of the Yellow River. The observation is arranged and implemented after flood season of the Yellow River generally. A temporary tidal level station is set up to revise the measured water depth during the observation period. Typical profiles data are selected from those of 1976, 1977, 1980, 1985, 1989, 1990, 1991, 1993, 1996, 1998, 1999, 2002, altogether amounting to 12 years (the positions shown in Fig. 2). The profile data is interpolated with the step water depth of 0.1 m, and the range of the water depth is decided to be 2.4 - 17 m due to the difference of water depth range in different years.

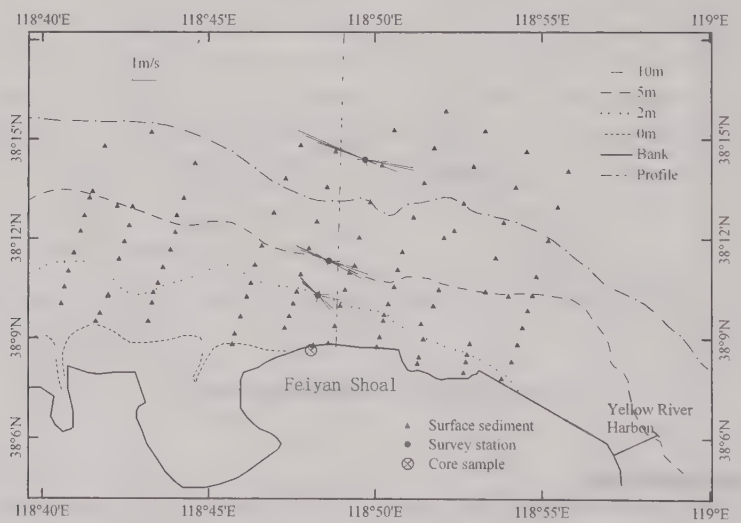

Fig. 2 Vector graph of field tidal flow and survey sites in the Feiyan Shoal

From Apr.19th to Apr. 27th of 2004, hydrology and suspended sediment surveys were carried out at 3 sites synchronously in the studied area. Surficial sediments and a core sample had been collected (the sites are shown in Fig. 2). The hydrology data was measured by the SLC-9 type current meter manufactured by Chinese Marine University. Sampling depth of surficial sediment was less than 5 cm. The core sample was collected from the high tidal flat (118°48′08″E, 38°08′37″N) by a truck borer, whose length was over 30 m with the diameter of 9 cm. It was cut into 1m sections and kept in PVC pipes hermetically. Sediment grain size was obtained by LS100Q laser particle size analyzer, manufactured by

American Coulter Corp., whose testing range is 0.000 4 - 0.9 mm and the error is less than 1 % for the same grain size. With a straight uni-directional flume with high speed flow at the Environmental Fluid Mechanics Laboratory in the Institute of Mechanics, Chinese Academy of Science in Beijing, the core sample was utilized in erosion resistance testing of undisturbed soil.

2 Hydrodynamic characteristics near shore

2.1 Tide flow

The tidal character is controlled by the amphidromic point of M_2 component tide (E119°04′, N38°04′) in the Northeast. The flood direction is westward. From the amphidromic point westward, the tide range increases, and the largest tidal flow speed reduces gradually. The max tide range of spring tide was 1.42 m in April 2004 (the lunar calendar was 1st March), and the minimum was 0.65 m. The vector graph of field tidal flow (Fig. 2) shows that the tidal flow in the form of rectilinear current is parallel with isobaths approximately. Suppose that the flow velocity is 0 at the 0 m water depth approximately, thus in a certain range, the deeper water depth, the higher tidal flow velocity. By means of the logarithmic equation the transverse distribution of the tidal-period and depth average velocity is:

$$\overline{V_y} = 0.1445 \times \mathrm{Ln}(y+1) - 0.0014 \tag{1}$$

Where y is water depth, $\overline{V_y}$ the tidal-period and depth average velocity at 'y' water depth, correlation coefficient R^2=0.9914.

During the tidal period T, the relation between the tidal-period and depth averaged velocity $\bar{u}$ and maximum depth-averaged velocity $\bar{u}_{max}$ can be expressed as the equation below:

$$\bar{u} = \frac{1}{T}\int_0^T \bar{u}_{max}\sin(\omega t)dt = \frac{2}{\pi}\bar{u}_{max} \tag{2}$$

Assuming that the flow is steady, the depth-averaged flow can be described as:

$$\bar{u} = \frac{1}{n}R^{2/3}i^{1/2} \tag{3}$$

The maximum bed shear stress by current can be expressed as $\tau = \rho g R i$.

$$\text{So} \qquad U_* = \sqrt{\frac{\tau}{\rho}} = \sqrt{gRi} \tag{4}$$

Through equation (3) and (4), the correlation between $\bar{u}$ and friction velocity U_* is:

$$\frac{\bar{u}}{U_*} = \frac{1}{n} R^{1/6} g^{-1/2}$$

Using water depth 'd' to stand for hydraulic radius R, $U_* = n\sqrt{g}d^{-1/6}\bar{u}$ (5)

Where n is 0.025.

Based on the field data, the maximum friction velocity of tidal flow can be calculated, and the result is shown in Fig. 3.

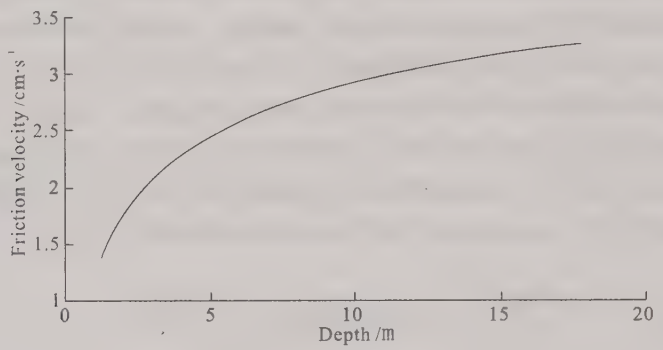

Fig.3 Distribution of friction velocity of tidal flow

2.2 Wave

The Bohai Sea is a semi-closed inland sea, and communicates with open sea only via the Bohai strait. The tidal wave is difficult to enter the Bohai Sea from Huanghai Sea, so the wind wave is preponderant in studied region. The direction of the strongest wave is NE-NNE, and that of the second strongest wave is N-NNW. The wave characteristics are listed in Tab.1 (Wu, 1989). The storm with 5.3m wave height and NE direction was observed at 14 m water depth on Nov. 22nd, 1985.

Tab.1 Wave Feature in the Northern Yellow River Delta

Direction	N	NNE	NE	ENE	E	ESE	SE	SSE	S	SSW	SW	WSW	W	WNW	NW	NNW	Total / %
0≤H<0.5	2.3	1.8	2.7	1.5	2.4	3.5	3.5	3.5	3.7	4.6	4.3	3.3	3.9	3.1	5.2	1.8	51.1
0.5≤H<1.5	2.1	1.9	4.0	2.5	4.1	2.3	3.8	2.1	1.4	1.7	0.9	0.9	1.0	1.4	2.5	3.7	36.3
1.5≤H<3.0	0.4	1.4	3.4	3.0	1.2	0.7	0.8	0.2	0.2	0.7	0.1	0.1				0.2	11.8
3.0≤H<5.0	0.1		0.2	0.1		0.1											0.5
Total / %	4.9	5.1	10.3	7.1	7.7	6.6	8.1	5.8	5.3	6.4	5.3	4.3	4.9	4.5	7.7	5.7	100
$H_{1/10}$ / m	3.0	2.5	3.1	3.3	2.5	3.0	2.8	2.6	0.8	2.0	1.5	2.4	1.1	1.0	1.4	2.1	

The relationship between average period and average wave height at Yellow River Delta can be expressed as [22]:

$$\overline{H} = 0.0338\overline{T}^2, \text{ convert } \overline{H} \text{ to } H_{1/10}: \ \overline{T} = 3.82\sqrt{H_{1/10}} \tag{6}$$

When it propagates from deep sea to nearshore, due to the shallow water effect, refraction and bottom friction action, the wave gradually declines.

$$\frac{H}{H_0} = K_r K_s K_f \tag{7}$$

Where K_r is shoaling coefficient, K_s is refraction coefficient and K_f is bottom friction coefficient. According to micro amplitude wave theory, K_c and K_s can be expressed respectively as follows:

$$K_r = \frac{\cos^{0.5}\alpha}{\left[1-\sin^2\alpha \text{th}^2(kd)\right]^{0.25}} \tag{8a}$$

$$K_s = \left[\frac{2ch^2(kd)}{2kd+sh(2kd)}\right]^{0.5} \tag{8b}$$

When $h/L_0<0.1$, K_s should be calculated based on Cnoidal Wave Theory [23]:

$$K_s = K_{s0} + 0.0015\left(\frac{h}{L}\right)^{-2.8}\left(\frac{H_0}{L_0}\right)^{1.2} \tag{8c}$$

Where $L = \frac{gT^2}{2\pi}\text{th}(kd)$ and $k = 2\pi/L$

K_f is calculated in accordance with the Bretschneider-Reid method [24]:

$$K_f = \frac{H_2}{H_1} = \left[1+\frac{64\pi^3 f H_1 X K_s^2}{3g^3T^4\sinh^3(kd)}\right]^{-1} \tag{8d}$$

Where X is the horizontal distance from water depth H_1 to H_2. L is wavelength; T is wave period; d is water depth; f, the frictional coefficient, is 0.015.

In a wave period, the peak value of bed shear stress is [25]: $\tau_w = \frac{1}{2}\rho f_w u_w^2$

Linear wave theory shows that the maximum horizontal velocity of water particle at the bottom can be expressed as:

$$U_{max} = \frac{\pi H}{T\sinh(kd)}$$

The maximum friction velocity at the bottom:

$$U_{*max} = \sqrt{\frac{\tau_{max}}{\rho}} = \sqrt{\frac{f_w}{2}} \times U_{max} \quad (9)$$

The wave propagates to nearshore, enduring a remarkable topographical bottom friction effect. Feiyan Shoal experienced an erosion process of 26 years from 1976 to 2002, and the topography has changed enormously. The process of wave damping varies on different topographies, and distribution of the friction velocity takes on different characteristics. Therefore, based on the topography data of 1976 and 2002, the wave friction velocity is calculated separately. The result is drawn in Fig. 4. It is found that the wave friction of the two years is dissimilar regarding the wave height over 1 m. The energy consuming speed on the topography of 2002 is slower than that of 1976, and the peak of friction velocity moves landward; the friction velocity in 2002 is greater than that in1976 only at the shallow area; at the area with water depth more than 4 m, friction velocity in 1976 is greater than that in 2002.

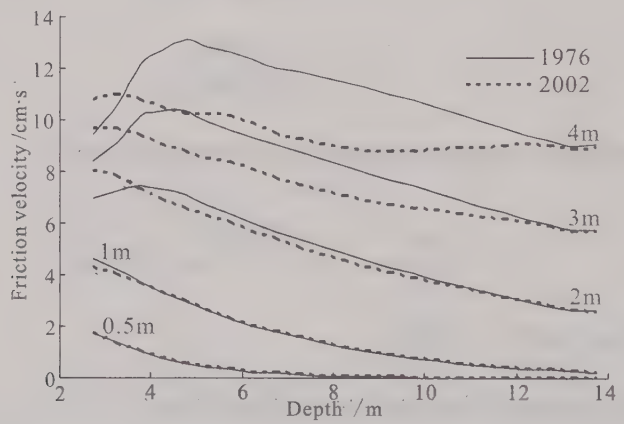

Fig.4 Distribution of near-bed wave generated friction velocity

2.3 Interaction of wave and tidal current

Vector sum principle is used for calculating the interaction of wave and tidal flow. Suppose at the moment of the largest tidal flow, the maximum wave-current friction velocity is calculated. Take the topography of 2002 for example (Fig. 5): in shallow water the wave-current friction velocity is higher than that in deeper water. When the coming wave height is 4 m, the maximum value is over 12 cm/s. At the moment of slack tidal flow, the maximum wave-current friction velocity is the same to that in Fig. 4. The velocity of tidal flow declined after 1976 [26], and the majority of wave friction velocity in 1976 is higher than that in 2002 in the depth range of study. Thus the friction velocity of wave-current is considered to have decreased since Feiyan Shoal was abandoned in 1976.

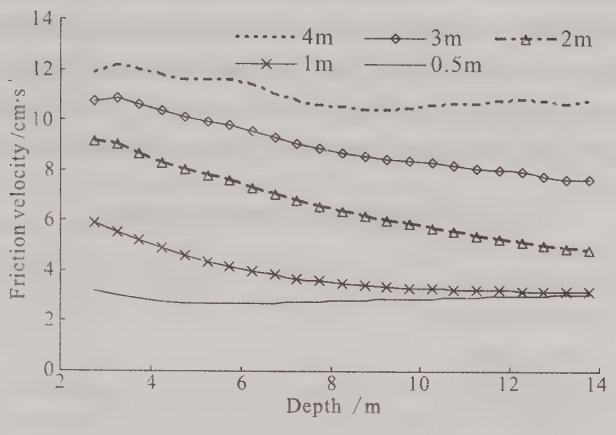

Fig.5 Distribution of tidal and wave co-action generated friction velocity

3 Sediment characteristics

3.1 Newly deposited sediment

High sediment concentration and concentrating sediment transport result in the rapid deposition of sediment from Yellow River at the river mouth, which is a high water content and low soil compactness delta deposition body. When Feiyan Shoal was abandoned in 1976, the shallow layer of seashore was newly deposited sediment. The dry bulk densities of deposits in the top 0.5 m give an average of 0.750 g/cm^3, and those of deposits buried below 0.5 m are 0.908 g/cm^3 on average [17]. The relation between threshold shear stress and dry bulk density adopts the result of sediment test of top layer done by Huhe (Huhe Aode. Scouring equipments of scatula originalis soil and surficial sediment of Yangtze Estuary Deepwater Channel, 1998)

$$\tau_c = 2.069\times10^{-9}\mathrm{S}^{2.71}$$

Here S is dry bulk density. The threshold shear stress of deposits in the top 0.5 m is 0.128 N/m^2, and that buried below 0.5 m is 0.908 g/cm^3, which are 1.13 cm/s and 1.47 cm/s after being conversed to threshold friction velocity respectively.

3.2 Surficial sediment at present

One hundred and four surficial sediment samples were gathered in Apr. 2004. According to 2 m, 5 m and 10 m water depth, they are divided into 4 groups, and the characteristics are listed in Tab. 2.

Sediment grain becomes finer and finer from nearshore to sea, which is the result of seashore erosion and sediment sorting. Nearshore erodes and the fine sediment is transported to deep sea, then coarser grain sediment is left on the nearshore. The sorting coefficient increases within 10 m, while it decreases at deeper than 10 m. This phenomenon is due to the fact that at depth of about 12 m is the

boundary of delta front and prodelta of sub-Yellow River Delta [15]. The deposit is mainly made up of fine sediment during the period of delta construction. Part of the fine sediment that is eroded from nearshore silts up in areas deeper than 12 m. Therefore, the deep sea area lacks the component part of coarse particle all the while, thus the sorting coefficient is better. From Tab. 2, it is found that the deeper water depth is, the finer the grain is, and the greater threshold friction velocity for sediment motion is.

Tab.2 Surficial sediment character in 2004

Depth rang / m	0-2	2-5	5-10	10-14
Median diameter / um	75.1	59.3	52.8	47.7
Sorting coefficient	1.73	1.90	1.95	1.79
U^*_c / cm.s^{-1}	1.60	2.18	2.87	3.51

3.3 Core samples

Shi et al. [27] have utilized the core samples to do erosion resistance testing of undisturbed soil. It is found that threshold friction velocity of sediment is 3.6 - 3.8 cm/s, which is at the 3 - 7m depth of the core samples. Due to the compaction effect of sediment above, sediment compactness of over 7 m increases, water content declines, and viscous force between fine sediments enhances, and correspondingly, threshold friction velocity of sediment also increases. It increases sharply to 10 - 14 cm/s at depth of 9 - 13 m of core samples, which is the largest part in the depth range of study.

4 Profile change

4.1 General features

Before Feiyan Shoal was abandoned, the coastal profile had the three zones of delta geomorphological structure, which was composed of pro-delta, delta front and subsided delta platform. From beach to sea, the slope of profile was soft-steep-soft, which was the typical topographty of reversed 'S' shape. After course diversion in 1976, the coast eroded and retreated backward rapidly (Fig. 6).

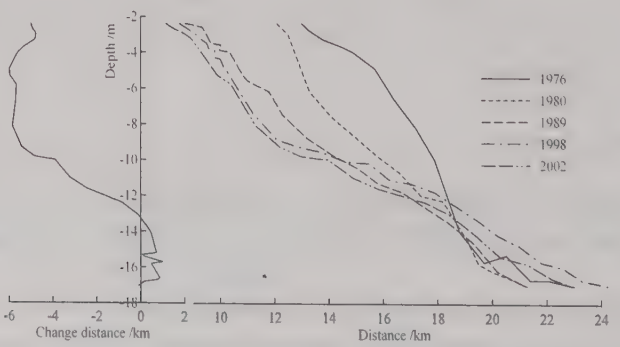

Fig.6 Erosion of coastal profile and corrosive distance

(The left is the eroding or silting-up change distance in the 26 years, and the right is the process of profile change)

From 1976 to 2002, the erosion volume per unit width in the depth range of 2.4 - 17 m is over 4.7×10^4 m^3. The depth range of the most backward distance is 3.5 - 9.5 m water depth; the depth-average value amounts to 5.7 km, with 319 m/a; the depth of the most backward is 4.9 m, amounting to over 5.99 km. It can be seen in Fig.6 that with water depth deeper than 9.5 m, the retreat distance reduces. At 13.3 m depth, it becomes net silt-up. The amount of silt-up is minor in the 26 years, just about 1km. The profile slope becomes softer and softer, from 0.150 % in 1976 to 0.098 % in 2002. With the reduction of the pro-delta's horizontal distance and the gradual disappearance of the delta front, the shape of profile changes to sunken from upper-convex.

4.2 Period characteristics

Based on the character of profile change, the profile change can be divided into 4 periods. Fig. 7 and Tab. 3 show that the profile erodes backward at a high retreating speed before 1980. In this period, the profile retreated intensively and integrally. The max retreat took place at 6.2 m water depth, which was up to 2 940 m; while there was a soft silting at the depth range of 13.5 - 14.6 m, which was less than 100 m. In the period of 1980 - 1989, the profile development started the process of upper erosion and down silting. The threshold depth between erosion and silting was about 14.2 m, and the depth of the maximum retreating distance became shallower with retreating speed slowing down. The years of 1989 - 1998 were a fluctuating adjustment period. The most backward distance at each depth hadn't exceeded 1.2 km in the 10 years. Water depth 10.1 m was the threshold depth of this period. The amount of progradation at deep water was high; all the progradation distance below 11.7 m water depth was over 1.2 km, and what's more, the progradation distance was 3.0 km at 17 m depth. After 1998, the profile transferred to integral erosion again, and the erosion amount at deep water was higher than that at shallow water.

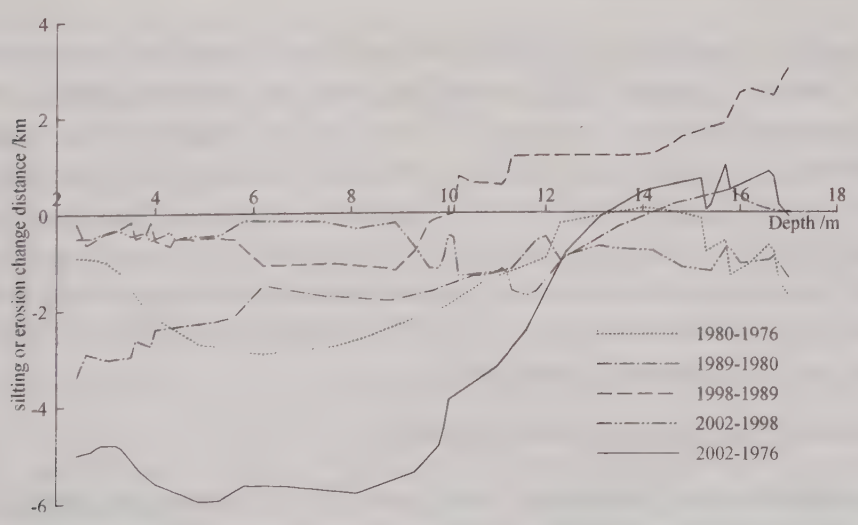

Fig.7 Change of profile in different periods

Tab.3 Distance change of recession and progradation at different depth

Water depth	1976-1980		1980-1989		1989-1998		1998-2002	
/ m	Amount / km	Average / m	Amount / km	Average/ m	Amount / km	Average/ m	Amount / km	Average/ m
2.5	-0.91	-228	-3.13	-348	-0.43	-43	-0.5	-135
5	-2.74	-685	-2.28	-253	-0.5	-50	-0.46	-125
10	-1.92	-480	-2.07	-230	-0.04	-4	-0.45	-112
13	-0.09	-23	-0.59	-66	1.20	120	-0.73	-182
16	-1.20	-300	0.34	38	2.51	251	-1.08	-270

5 Discussions

5.1 Relationship between sediment erosion resistance and profile retreat speed

5.1.1 Weak erosion resistance at earlier periods of abandonment

The sediment from the Yellow River deposited near bank constantly, which resulted in the new incompact deposition without the cover load of sediment above. The dry bulk density of deposit in the top 1m was under the average value of 0.908 g/cm^3 [17]. Erosion resistance of the incompact deposition was very low, whose threshold friction velocity was not over 1.47 cm/s. It was easy to be started and transported by the tidal flow. At the earlier periods of abandonment, the seashore entered the state of quick erosion, and the profile retreated backward wholly. In the first 4 years, the retreating speed was the fastest with 735 m/a at 6.2 m water depth.

5.1.2 Increase of sediment resistance

After the new incompact sediment of shallow water eroded and disappeared, the sorting effect made the sediment resistance strengthen. On the other hand, sediment resistance enhanced with deposit compaction increasing along depth gradually. It is found that the threshold friction velocity of core sampling sediment of the range of 3 - 7 m depth was about 3.7 cm/s, which was similar to the threshold friction velocity of surficial sediment in 2004. The tidal friction velocity was lower than the sediment threshold friction velocity in 2004, so it is concluded that the erosion active force became interactive of wave and tide. Wave is to move the sediment and tidal flow is to transport sediment mainly. With sediment resistance enhancing, the main eroding force changed to the interaction of wave and tide from the single tidal flow, while the speed of retreating slowed down gradually.

5.1.3 Vertical differences of deposition and profile shaping

The net retreating curve of profile takes on the figure of 'soup ladle' during the period of 1976-2002 (Fig. 7). About 9.5 m depth is a mutation point; the backward distance is over 4.8 km at shallow water, retreating amount is reduced to 3.8 km suddenly at 10 m depth, and then declines gradually until it turns into the net silt. According to the erosion resistance test of the core samples, from 9 m depth the clay

content increases rapidly, and water content declines, and the threshold friction velocity increase to 10 - 14 cm/s that is the max value of the core sample. The depth ranges of high sediment resistance and the retreating distance change are consistent.

5.2 The illustration of profile shaping

The coastal erosion profile shaping process has the following characteristics: (a) The eroding speed slows down gradually from the initial periods of abandonment; (b) The depth ranges of max backward distance in different periods become shallower and shallower; (c) The topographical profile presents a phenomenon of up erosion and down accumulation, and the slope becomes soft gradually.

The intense erosion has made the slope of the profile soft. The softer topographical slope is, the longer distance wave propagates to nearshore from a certain water depth, and the energy consuming is more dispersive, and the corresponding wave friction velocity decreases, and the peak value wave friction velocity moves landward, and the depth range of the max retreating distance becomes shallower gradually. The sediment at the depth range of max retreating distance can be scoured by the interaction of tide and wave whose wave height is less than 1 m, while the scoured sediment needs the interaction of tide and wave whose wave height is over 1.5 m with the frequency of just 12.3 % at about 12 m water depth area. The deeper the water is, the less probability that the sediment starts up is. The coarser part of suspending sediment is easier to deposit when hydrodynamic force becomes weaker. The finer the sediment is, the greater difference value of threshold velocity and non-depositing critical velocity will be. Thus, the finer sediment can be transported farther. When the amount of deposit is more than the erosion amount, the profile takes on net accumulation. Thus, the profiles have the characteristic of up erosion and down accumulation in the eroding process.

Due to the storm tides took place in 1992 and 1997 at Yellow River Delta, the silting increased in regions of over 10 m water depth by a large margin in the 1990s. When the storm tidal takes place, on condition of backwater with high hydrodynamic energy, the materials of land area above low tidal flat are corroded and carried to the deep sea. It often makes the deep water area deposit fast, which happens frequently at the beach of the Yangtze River [28]. The fast storm tidal deposition is also of low soil compactness, which will be adjusted after the storm. The change of surficial sediment may result in the trend change of profile development: so the profile entered a new period of corroding again after 1998.

5.3 The threshold depth and dynamic strength

The hydrodynamic force varies, so the threshold depth is not the same at different areas. The stronger hydrodynamic force is, the deeper threshold depth is [29]. As illustrated in Section 4.2, the profile development has experienced 4 periods. At the period of incipient abandonment and the storm tides later, the profiles retreated rapidly, and the threshold depth did not exist. In the later two periods, the main character of profile retreating process was up erosion and down accumulation. With the weakening of hydrodynamic force, the threshold depth also reduced from 14.1 m to about 10 m water depth. It is concluded that if the hydrodynamic force is far greater than the sediment resistance, the profile retreating

process takes on the character of eroding integrally; if the hydrodynamic force and the sediment resistance is comparable, the profile retreating process takes on the character of up erosion and down accumulation, and the threshold depth exists.

6 Conclusions

The essence of strong erosion process of Feiyan Shoal is that sediment transports and redistributes and delta deposition dwindles constantly under the control of marine dynamic. The development characteristics of topographical profile are decided by hydrodynamic force and sediment factors. The following are the characteristics of coastal profiles retreating at Feiyan Shoal:

a) At the initiative period of abandonment, the low sediment resistance of new incompact sediment is the main reason for the coastal profiles eroding and retreating backwards at a high speed. As the surficial sediment resistance strengthens, the main erosion action force changes from tide to the interaction of tide and wave. The feature of profile shaping becomes up erosion and down accumulation from integral erosion, and the retreat speed declines gradually.

b) With the decrease of tidal flow nearshore and landward distribution of peak value distribution of wave bottom friction velocity, the retreat distance and critical depth change less and becomes shallower gradually.

c) The high energy of storm tide may change the developing trend of profiles. It is still the triggering force of seashore topographic profile development in the future.

Acknowledgements

This study is supported by the Major State Basic Research Development Program of China ('973' Program) (Grant No.2002CB412408) and the Shanghai Youth Science and Technology Venus (Grant No.06QA14016).

Reference

[1] Bird E. C F Coasts [M]. 1984, New York: Basil Blackwell Publishing: 71 - 75.

[2] Dolan Robert, Trossbach Susan, Buckly Michael. New Shoreline Erosion Data for the Mid-Atlantic Coast [J]. Journal of Coastal Research, 1990, 6(2): 471 - 478.

[3] Yu Zhiying, Zhang Guoan, Jin Liu, et al. Evolution Prediction of the Abandoned Yellow River submerged delta under wave and current[J]. Oceanologia et Limnologia Sinica, 2002, 36(6): 583 - 590.

[4] Zhang Renshun, Lu Liyun, Wang Yanhong. The mechanism and trend of coastal erosion of Jiangsu Province in China [J]. Geographical Research, 2002, 21(4): 469 - 478.

[5] Ji Zixiu. The Characteristics of Coastal Erosion and Cause of Erosion [J]. Journal of Natural Disasters, 1996, 5(2):

65 - 75.

[6] Reng Yuchan, Zhou Yongqing. Morphological Features and Evolution of the Abandoned Huanghe River Delta [J]. Marine Geology and Quaternary Geology, 1994, 14(2): 19 - 28.

[7] Chen Shenliang, Zhang Guoan, Gu Guochuan. Application of multi-scale finite element method to simulation of groundwater flow [J]. Journal of Hydraulic Engineering, 2004 (7): 1 - 7.

[8] Li Hengpeng, Yang Guishan. The Spatial Analysis of Erosion and Deposition of Tidal-Flat by GIS [J]. Acta Geographica Sinica, 2001, 56(3): 278 - 286.

[9] Yi Yanhong. Erosion and silting up and land making rates of the modern yellow river delta coast [J]. Marine Geology Letters, 2003, 11:13 - 19.

[10] Cheng Guodong. Sedimentation and sedimentarymodels of modern Huanghe River Delta [M]. 2001, Beijing: China Geology Press.

[11] Ye Qingchao. The Geomorphological Structure of the Yellow River Delta and its Evolution Model [J]. Acta Geographica Sinica, 1982, 37(4): 349 - 363.

[12] Huang Shiguang. Erosion and accumulation in the adjacent area of the Taoerhe bay —with emphasis on erosion-accumulation of the Huanghe river delta after its shifted course [J]. Oceanologia et Limnologia Sinica, 1993, 24(2): 197 - 204.

[13] Liu Yong, Li Guangxue, Deng Shenggui, et al. Evolution of erosion and accumulation in the abandoned subaqueousdelta lobe of the yellow river [J]. Marine Geology and Quaternary Geology, 2002, 22(3): 27 - 34.

[14] Ding Dong, Dong Wan. A preliminary study on the erosion of the modern Huanghe river delta [J]. Marine Geology and Quaternary Geology, 1988, 8(3): 53 - 60.

[15] Zhou Yongqing. The subaqueous slope regress progress and main characteristics of the northern coast of the Yellow River delta [J], Marine Geology and Quaternary Geology, 1998, 18(3): 79 - 84.

[16] Dong Nianhu. The deposit and diffuse of the yellow river sediment into the sea [J]. The Ocean Engineering, 1997, 15(2): 59 - 64.

[17] Shi Changxing, Zhang David Dian, You Lianyuan. Sediment budget of the Yellow River delta, China: the importance of dry bulk density and implications to understanding of sediment dispersal[J]. Marine Geology, 2003, 199: 13 - 25.

[18] Li Fulin, Pang Jiazhen, Jiang Mingxing. Shoreline changes of the yellow river delta and its environmental geologic effect. Marine Geology and Quaternary Geology, 2000, 20(4): 17 - 21.

[19] Li Dongfeng, Li Zhegang, Zhang Yuqing. Numerical analysis of effect of sediment from northward route of Qingshuigou on Dongying Port [J]. Journal of oceanography of huanghai & bohai seas, 1998, 16(1): 1 - 6.

[20] Li Guosheng, Wang Longhai, Dong Chao. Numerical Simulations on Transportation and Deposition of SPM Introduced from the Yellow River to the Bohai Sea [J]. Acta Geographica Sinica, 2005, 60(5): 349 - 363.

[21] Chen Shenliang, Zhang Guoan, Chen Xiaoying, et al. Coastal erosion feature and mechanism at feiyantan in the yellow river delta [J], Marine Geology and Quaternary Geology, 2005, 25(3): 9 - 14.

[22] Fan Shunting, Wang Yimou. An analysis for element ratio of characteristic wave over yellow river mouth area [J], Marine Forecasts, 1999, 16(1): 21 - 28.

[23] Wu Songren. Coastal Dynamics [M]. 2000, Beijing: China Communications Press.

[24] Yan Kai. Coastal Engineering [M]. 2002, Beijing: China Ocean Press.

[25] Jonsson I G. Wave boundary layers and friction factors [J]. Process of 10th Conference of coastal Engineering, 1996: 127 - 148

[26] Hao Yan, Le Kentang, Liu Xingquan. A numerical prediction of the tidal characteristics in 2010 of yellow river delta [J], Marine Science, 2000, 24(6): 43 - 47.

[27] Shi Lianqiang, Li Jiufa, Ying Ming. Erosion experiments on natural sediment from the Modern Yellow River Delta [J]. The ocean engineering, 2006, 24(1): 46 - 54.

[28] Li Jiufa. The study on sediment transportion at nanhui tidal flat of Yangtze River Estuary [J] Acta Oceanologica Sinica, 1990, 12(1): 75 - 82.

[29] Ying Ming, Li Jiufa, Li Weihua, et al The study on Profile Shaping Process of Northern Yellow River Delta Coast. IGARSS 2005: 2005 IEEE International Geoscience and Remote Sensing Symposium proceedings: 25 - 29 July 2005, Seoul, Korea, 2005.

黄河三角洲飞雁滩动力特征与地形剖面塑造

应 铭[1]，李九发[2]，陈沈良[2]，戴志军[2]

（1. 中交上海航道勘察设计研究院有限公司，上海，200120；2. 华东师范大学，河口海岸学国家重点实验室，上海，200062）

摘 要：飞雁滩是1964年1月至1976年5月黄河刁口河由一月流路入海形成的新河口三角洲。自1976年黄河改走清水沟入海后，飞雁滩宏观呈现侵蚀后退。以20世纪70年代以前的地形资料为基础，2004年4月现场水文泥沙及沉积物取样资料为基础，地形剖面与岸滩演变作为考证参数，并根据实测资料计算了波流共同作用下的底摩擦流速的模型参数，从动力学和沉积机理角度分析了飞雁滩典型地形剖面变化规律。30 a来飞雁滩岸滩地形剖面经历了"快速后退变陡——慢速调整——淤积复宽"的变化过程，这实际是其三角洲前缘侵蚀消失过程。沉积物粒径细化是造成侵蚀后退速率变化的主要原因。水动力条件的变化改变了不同水深的侵蚀与淤积量，决定最大侵蚀量水深范围与闭合深度。风暴潮仍是今后海滩地形剖面演变的触发动力。

关键词：黄河三角洲；飞雁滩；侵蚀；波流共同作用；地形剖面；泥沙输移

Application of Dynamic Track Drawing Algorithm in Ship Monitoring System

ZHANG Feng, LI Sihai, LIU Jin

National Marine Data and Information Service, Tianjin 300171, *China*

Abstract: The function of dynamic track drawing realized in the ship monitoring system. Based on the function, we could draw the sailing tracks dynamically according to the ship's orientation. Two kernel algorithms are involved during the system developing process, i.e. the algorithms of angular deflection and distance interval value. The practice of system development shows that the proper application of these two algorithms has good effect in the visualization of sailing track.

Keywords: angular deflection; distance interval value; algorithms; GIS

1 Introduction

With the development of"3S" (GIS, RS, GPS) technology, it has become possible now to collect, manage, analyze and display spatial data and information conveniently and intuitively. And the application of this technology in the modern ocean management is displaying an increasingly significant scientific power.

The ship monitoring system, developed with the application of GIS, RS and GPS technologies, is supported by basic geographic spatial database, ship position database and ship attribute database. It contains some main function modules i.e. data collecting module, spatial and attribute information management module, track drawing module etc. With the function of importing the ship position GPS data, the data collecting module can update ship position information in the local database regularly or instantly. The space and attribute information management module can add, delete and correct the space information existing in system's space database such as basic geography data, remote sensing data and so on, and manage the ship position data, ship attribute data as well. The track drawing module can draw the historic and instant track line dynamically, and also display ship position. Combined with some auxiliary functions such as planning track drawing, red tide and oil-spill area monitoring, the monitoring system can provide ship administration authorities with accurate, intuitive data and decision-making support so that they can be in command of ships' moving status timely and make an appropriate dispatch of all ships. The monitoring system was developed through the adoption of VisualBasic 6.0 and MapObjects 2.2 of ESRI, and with abundant function bases, MapObjects can provide powerful function in displaying map elements i.e. point, line, polygon etc. By means of relevant algorithms, the monitoring system reaches a better visualization effect in drawing ship track dynamically.

Received on April 7, 2008

2 Track drawing methods and the realizations

There are two track drawing methods applied in the ship monitoring system. The ship track can be drawn statically and dynamically according to the ship's latitude & longitude points' values at different times. The statically drawing method is to specify the shipment of a certain ship, and the system will connect all of the certain ship's latitude & longitude point in the period of the shipment using the line segment and display it in line. The dynamically drawing method is to mark the static shipping track line with arrows towards its movement and the system will put automatically an interval value between two neighboring track points in distance.

The statically drawing method is realized by developing track line from every points in the track line as inflexion points, and during this realization, the system execute upon every two neighboring track points successively the 'DrawShape' Drawing method included in the MapObjects to draw a static line segment, thus a static track line will be created between every two neighboring track points (the white dashed line in Fig. 3), and the line style of static ship track line can be set in the property of 'DrawShape'. Comparatively, the dynamically drawing method is much more complex, which comes in the shape of the arrow representing the ship moving in line with the static track line. To realize it, you must first go over every track point of the ship track line in the time sequence, and mark them with arrows which represent the specified ship, and then adjust directions of arrows according to the orientations of current track line to make sure the arrows' directions always directing to the orientations that the ship moves forward, at last, the system will set the speed of all arrows and space of every two neighboring arrows to make sure the ship moves in an uniform speed, which displays more intuitionistically. In the realization of dynamically drawing method, there are two core algorithms: the arrow's automatic angular deflection and long distance interval value, which are demonstrated below.

3 Analyses on algorithms

3.1 Angular deflection algorithms

While drawing the sailing track statically, the arrow symbols should deflect automatically according to the directions of line segments between each two neighboring track points to keep them always directing to the directions the ship is moving forward, and the angular deflection algorithms can realize it. In angular deflection algorithms, the angular deflection function value (Angle, abbreviated to deflection value), which can decide directions of the mark symbols, depends on the X and Y coordinate value of each two neighboring track points Pt1 and Pt2, and according to the comparisons of those two track points' X and Y coordinate value, the Angle value may be worked out in 8 different circumstances, details are as follows:

(1) if ((X1 = X2) and (Y1 < Y2)) then

Angle1 = 0

In which, X1=Pt1.X, Y1=Pt1.Y, X2=Pt2.X, Y2=Pt2.Y(the following is same), here the orientation of the track is north, and the value of Angle1 is 0;

(2) if ((Y1 = Y2) and (X1 < X2)) then

Angle2 = 90

here the orientation of the track is east, and the value of Angle2 is 90;

(3) if ((X1 = X2) and (Y1 > Y2)) then

Angle3 =180

here the orientation of the track is south, and the value of Angle3 is 180;

(4) if ((Y1 = Y2) and (X1 > X2)) then

Angle4 = 270

here the orientation of the track is west, and the value of Angle4 is 270;

(5) if ((X1 < X2) and (Y1 < Y2)) then

Angle5 = Atn (Abs(X1 - X2) / Abs(Y1 - Y2)) * 57.325

In which, Atn function is the result of tangent, and multiplying 57.325 means transform to angle value from radian value, and the position of Angle5 is located in the first area, 0<Angle5<90;

(6) if ((X1 < X2) and (Y1 > Y2)) then

Angle6 = (Atn(Abs(Y1 - Y2) / Abs(X1 - X2)) + 1.57) * 57.325

Adding 1.57 means it is located in the second area, adding π/2 value of radian, and the position of Angle6 is located in the second area, 90<Angle6<180;

(7) if ((X1 > X2) and (Y1 > Y2)) then

Angle7 = (Atn((Abs(X1 - X2) / Abs(Y1 - Y2))) +3.14) * 57.325

Adding 3.14 means it is located in the third area, adding π value of radian, and the position of Angle7 is located in the third area, 180<Angle7<270;

(8) if ((X1 > X2) and (Y1 < Y2)) then

Angle8 = (Atn ((Abs(Y1 - Y2) / Abs(X1 - X2))) + 4.71) * 57.325

Adding 4.71 means it is located in the fourth area, adding 3π/2 value of radian, and the position of Angle8 is located in the fourth area, 270<Angle8<360;

These eight cases as shown in Fig. 1:

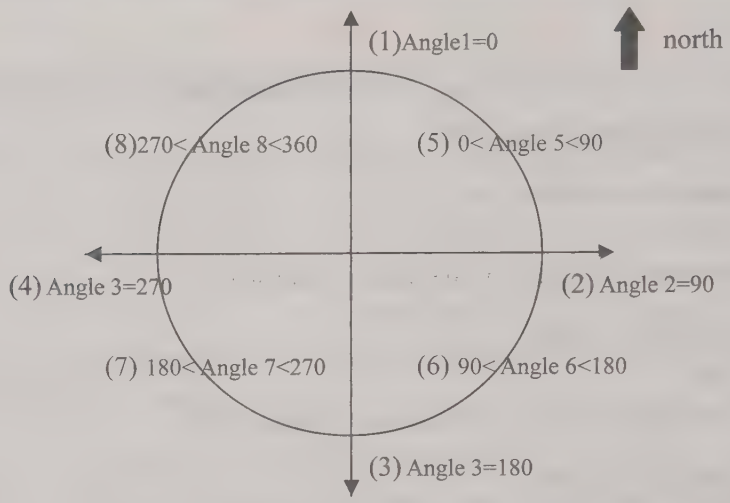

Fig. 1 Distribution of eight kinds of Angle Value

By the application of this algorithms, every track point's Angle values can be worked out depending on each two neighboring track points' X and Y values, and then put these Angle values into symbol drawing function, the instant deflection directions of the arrow symbols can be drawn successfully.

3.2 Distance interval value algorithms

How to control the interval distance between each two arrows is another problem that needs to be solved while drawing arrows dynamically. Under default circumstance, the program will mark every track points on the sailing track with arrows successively according to the sailing direction, and the arrows' directions, always directing to the next track point, are controlled by the angular deflection algorithms demonstrated above. The problem under this circumstance is that the track points' latitude & longitude values are measured by GPS regularly, but the sailing speed varies, so the distances of each two neighboring track points are changeable, meanwhile, the time intervals are certain while drawing every arrows on the sailing track dynamically, and this results in an uneven jump while drawing two neighboring arrows, which displays invisibly on the screen. The key to solve this problem is to keep all intervals between each two neighboring arrows equal, thus you should rather adopt distance interval value algorithms than just marking two neighboring track points with arrows.

Distance interval value algorithms can make a judgment on the relation between the distance of the coordinate of each two neighboring track points and the pre-define interval value distance constant, and then put in an interval value automatically between each two neighboring coordinate points, therefore equal-distance coordinate point can be created on the sailing track. The problem of incoherence of arrows marked dynamically along the sailing track can be solved well through putting in interval values between each two neighboring track points of unequal distances. And there are 3 steps to apply the distance interval value algorithms to practice:

(1) Set a constant 'Dist_min', which decides the Precision of spatial Interpolation, and calculate the

distance declared as 'Dist_2Tp' between two neighboring points of the ship track by using of the trigonometric function. The expressions are as follows:

Dist_2Tp = Sqr((Pt2.X−Pt1.X)*(Pt2.X−Pt1.X)+(Pt2.Y−Pt1.Y)*(Pt2.Y−Pt1.Y))

In which Sqr−extraction function;

Pt1.X− X-coordinate value of the first point;

Pt2.X− X-coordinate value of the second point;

Pt1.Y− Y-coordinate value of the first point;

Pt2.Y− Y-coordinate value of the second point;

(2) Compare the two constants between 'Dist_min' and 'Dist_2Tp', there are two results:

(a) If 'Dist_Min'>'Dist_2Pt',draw an arrow between the two neighboring points of the sailing track with out interpolation.

(b) If 'Dist_Min'<'Dist_2Pt',do interpolation firstly, and the number of interpolation points depends on how many times Dist_2Pt is of Dist_Min, the expressions is:

N=CInt(Dist_2Pt/Dist_Min)

In which, CInt−taking integer function;

(3) Calculate the coordinate values of each interpolation point, Pt.X and Pt.Y. The method is to go through the sailing track between two neighboring track points: based on the first point and adding constant to it one by one, then you can get the coordinate value of each interpolation point. The expressions are as follow:

Pt.X = Pt1.X + i * (Pt2.X−Pt1.X) / (N + 1)

Pt.Y = Pt1.Y + i * (Pt2.Y−Pt1.Y) / (N + 1)

In which, i−the increasing ordinal number of interval value point($1 \le i \le N$, and i is an integer)

N−the number of the interval value

Draw the arrow at each interpolation point by using the symbol-drawing function after getting the coordinate value. The angle value is needed in this function.

It can not ensure that all distance values between two arrows are absolutely same by using the method mentioned before because there are two special cases:

(a) The distance between two neighboring points of the sailing track is less than the constant 'Dist_Min'. (Fig.2(b) track point2 and point3)

(b) It is not an integral value that the times Dist_2Pt is of Dist_Min(Fig.2(b) track point3 and point4)

These two cases will make the distance between two arrows short. Setting an appropriate value for the 'Dist_Min' in practice will get a better drawing effect.

4 Algorithms application effect in system function realization

The two algorithms, angular deflection and distance interval value play important roles in realizing the function of dynamic track drawing, and good visual effect can only be reached with combination of

these two algorithms. During drawing the track, it is the first to determine locations of two neighboring points where arrows shall be marked using program function in distance interval value algorithms, and then determine the arrows' directions according to coordinates of these two points using program function in angular deflection algorithms. But it is noticed that the interval points of each two neighboring points are on a straight line segment with the same arrow directions, and are also of the same directions with direction of the first point, so the actual arrows directions will not be influenced by the sequence of the adoption of these two algorithms. But for the purpose of optimizing program efficiency, the angular deflection algorithms is usually adopted first and then the distance interval value algorithms in actual development, so that it can be avoided to make angular deflection algorithms on every interval point.

Fig. 2 shows the application effect of these two algorithms. As indicated by Fig. 2(a), the arrows marked along sailing track without adoption of the angular deflection algorithms are directing to the same default direction. By adopting the angular deflection algorithms, as indicated by Fig. 2(b), the arrows' directions are decided in accordance with every corner angle values, i.e. always directing to the direction of the sailing track. And in Fig. 2(c), there are five track points, and the distances of each two neighboring track points are different. The arrows will only be marked on track points if interval value algorithms were not adopted, and this will result in the incoherent display of arrows, which is not in accordance with the actual sailing track. By adopting the interval value algorithms, arrows will be marked regularly along the sailing track according to the distance constant set up by program, this shows the uniform movement of the ship and therefore displays better. The system operating effect is as displayed in Fig. 3.

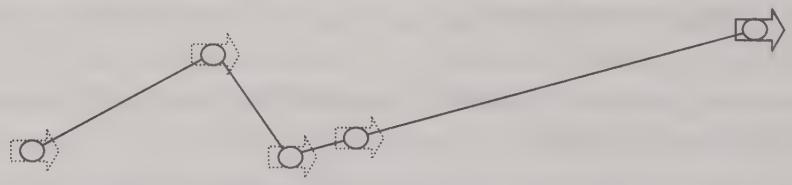

(a) drawing arrow symbol not executing the angular deflection calculation

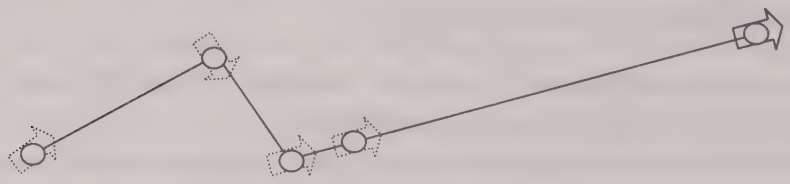

(b) drawing arrow symbol not executing the interval value calculation

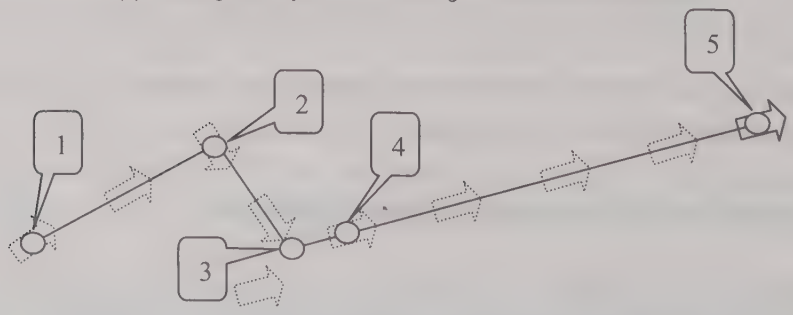

(c) drawing arrow symbol after executing the interval value calculation

Fig.2 Algorithms Application Effect

Fig.3 Dynamic Track

5 Conclusion

In the Monitoring System of the marine surveillance ships, it congregates the GIS functions of collecting and management on the ships spatial data as well as the dynamic drawing for the ship tracks. The algorithm application is the key of achieving the ideal result. The computation of the rotation angle and the interpolation are the two fundamental methods in completing the dynamic drawing for the ship tracks. And it achieves the objectivity and the direct-vision drawing in the ship tracks. But the problems still exist among the practical application of the ship monitoring system which are shown as below:

(1) It's not very intuitionistic to show the sailing track by using arrow to represent ship, and it's better to draw ship symbol instead of arrow because the former is more vivid. But the ship symbol is in the format of bitmap, so using it will result in an incoherent sailing track due to the limitation of program efficiency and screen refresh rate.

(2) The distance interval value algorithm is to put in interval values on an average basis according to the distance of two neighboring track points, and it does not take into account the instant shipping speed, so the shipping track is drawn assuming that the ship is moving at an uniform speed, which is not in accordance with the actual status.

(3) There are many uncertain factors to determine the length constant 'Dist_Min' in the application of distance interval value algorithms, which depends on three factors: interval of obtaining sailing track points, sailing speed and distance of the neighboring track points. So we shall determine or uniform these factors as possible as we can in data obtaining stage to determine a most reasonable length constant afterwards so that better display effect can be assured.

The above mentioned aspects will be improved with the improvement of system function designing, so that the system operating effect is more close to the actual status.

Lastly, it should be pointed out that these two algorithms can also be applied to other developments of programs relating to angular deflection and distance interval value functions, and analysis on applications of these two basic algorithms will benefit the system developing staff in getting deeper understanding of the theory of realizing GIS function.

Reference

[1] Wu Lun, Liu Yu, Zhang Jing, et al. Geographic Information System-Principle, Method and Application, Beijing, Science Publishing Company, 2001.

[2] Guo Renzhong. Spatial Analyse [M]. Wu Han, Wuhan Technical University of Surveying and Mapping Publishing Company, 2000.

[3] Lü Anmin, Li Cheng Ming, Lin Zongjian. A primary Study of Area Interpolation Algorithm [J], Bulletin of Surveying and Mapping, 2002, 1: 44 - 46.

[4] Wu Jianhua, Lei Jinping. The Application of Spatial Analysis in Routing Design and Monitoring Navigation of China [J], 2004, 1: 41 - 43.

[5] Yu Lei, Zhao Hong, Zhao Zontao. Study on the Algorithms of Trajectory Planning based on Terrain Analysis [J], Microelectronics & Computer, 2005, 6: 121 - 123.

[6] Ren Xianfeng, Liu Xingyong. Study on Design of Ship Dynamic Management System [J], Marine Technology, 2004, 6: 74 - 75.

船舶监控系统中航迹线动态绘制算法应用研究

张 峰，李四海，刘 金

（国家海洋信息中心，天津 300171）

摘 要：船舶监控系统中实现了船只航迹线的动态绘制，系统能够根据船只航行方向动态显示航行轨迹，程序开发过程中涉及到偏转角度算法和距离插值两个核心算法，系统开发实践表明，这两个算法的合理应用在航迹线可视化表现方面取得了良好的效果。

关键词：偏转角度；距离插值；算法；GIS

海 洋 通 报（英文版）

HAIYANG TONGBAO

2008 年 10 月　第 10 卷　第 2 期

目　次

应用 Argo 资料分析西北太平洋冬、夏季水团……孙朝辉 等 (13)

城市热岛效应的卫星遥感分析…… 王桂玲 等 (25)

基于 GIS 水团分析集成系统的开发及其应用 …… 张月霞 等 (35)

平均海平面上升对东中国海台风风暴潮影响的数值模拟 ……高志刚 等 (49)

南极石油烃降解嗜冷菌的筛选及其降解特性的研究 ……郑　洲 等 (57)

围隔生态系内不同粒级浮游植物群落变化研究 ……李　涛 等 (67)

马氏珠母贝选群 F_1 的表型性状的相关和通径分析 …… 邓岳文 等 (73)

黄河三角洲飞燕滩动力特征与地形剖面塑造 ……应　铭 等 (88)

船舶监控系统中航迹线动态绘制算法应用研究 ……张　峰 等 (96)

Marine Science Bulletin

Marine Science Bulletin publishes papers on marine science and technology including physical oceanography, chemical oceanography, marine biology, marine geology, environmental oceanography, estuarine & coastal sciences, marine technology, digital ocean, coastal zone management, ocean engineering, marine economics, etc., and aims to promote international academic exchange.

Editor-in-Chief: LIN Shaohua (林绍花)
Associate Editor-in-Chief: HE Guangshun (何广顺) YANG Ying (杨 鹰)
Executive Editor: HE Xuewu (何学武) QIU Wenjing (邱文静)
ZHANG Xiaoxian (张潇娴) WANG Zhankun (王占坤)
English proofed by: WANG Qi (王琦)

semi-annually (started in 1999, sam 20)
Publication date: May. 15th and Oct. 15th

Marine Science Bulletin **(Vol. 10, No. 2, Oct. 2008)**

Responsible Institution:
State Oceanic Administration of China
Sponsored by:
National Marine Data and Information Service
Edited by:
Office of Marine Science Bulletin (English edition)
Printed by:
Printery of National Marine Date and Information Service

Published by:
Office of Marine Science Bulletin (English edition)
E-mail: msb@mail.nmdis.gov.cn
Tel: (022) 24011287
Address: 93 Liuwei Rd., Hedong District, Tianjin 300171, China

---

ISSN1000-9620
CN12-1271/N

Price: $ 30.00 / ￥18.00 Per year